



Trajectory Design for a Very-Low-Thrust Lunar Mission

Rogan Shimmin

Supervisors:

Assoc. Prof. Benjamin Cazzolato
Dr. Matthew Tetlow

School of Mechanical Engineering
Faculty of Engineering, Computer
and Mathematical Sciences
The University of Adelaide

*A thesis submitted in fulfillment of the requirements for the degree of Doctorate
of Philosophy on the 24th day of May in the year 2012*

Copyright ©2013 by Rogan Shimmin. All rights reserved.

Revised: 21st January, 2013

School of Mechanical Engineering
The University of Adelaide
North Terrace
Adelaide SA 5005
AUSTRALIA

Institut für Raumfahrtsysteme
Universität Stuttgart
Pfaffenwaldring 29
70569 Stuttgart-Vaihingen
DEUTSCHLAND

Contents

1	Introduction	1
1.1	Historical background	1
1.2	<i>Lunar Mission BW-1</i>	2
1.3	GESOP	5
1.4	Summary	6
2	Scope of research	7
2.1	Introduction	7
2.2	Optimisation of a low-thrust trajectory	7
2.2.1	Modelling	8
2.2.2	Investigation of optimisation techniques	8
2.2.3	Exploring different initial guesses	9
2.2.4	Application of non-linear constraints	9
2.3	Investigation of perturbations	10
2.4	Investigation of non-linear constraints	11
2.5	Limits of the scope	12
2.6	Summary of research scope	13
3	Review of relevant literature	15
3.1	Introduction	15
3.2	Past missions	15
3.2.1	Deep Space One	17
3.2.2	Hayabusa	19
3.2.3	SMART-1	19
3.2.4	Dawn	21

3.2.5	Planned missions	22
3.3	The process of optimisation	23
3.3.1	Problem formulation	23
3.3.2	Trajectory propagation	24
3.3.3	Optimisation methods	26
3.3.4	Survey of commercial optimisation algorithms	32
3.4	Application of optimisation methods to low thrust problems	34
3.5	Summary of gaps in existing knowledge	44
4	Rocket science	47
4.1	Orbits	47
4.2	The space environment	48
4.2.1	The van Allen belts	49
4.2.2	Space debris	51
4.3	Rocket performance	51
4.3.1	Specific Impulse	51
4.3.2	Delta-v	52
4.3.3	Tsiolkovsky's rocket equation	54
4.4	Sphere of influence	55
4.5	Summary	56
5	Orbital dynamics and modelling	57
5.1	Epoch	57
5.2	Reference frames	58
5.3	Orbital elements	62
5.4	Orbital equations of motion	64
5.5	Perturbations	66
5.5.1	Third-body perturbations	66
5.5.2	Oblateness of primary body	68
5.5.3	Solar wind	71
5.5.4	Applied thrust	72
5.5.5	Total perturbing forces	73
5.6	Summary of orbital dynamics	74

6 Optimisation	75
6.1 Introduction	75
6.2 State vector	75
6.3 Independent parameter	76
6.3.1 Substitution of parameters	77
6.4 Objective function	79
6.5 Boundary value problem	80
6.5.1 Boundary constraints	80
6.5.2 Path constraints	83
6.6 Numerical considerations	84
6.6.1 Integration error	84
6.6.2 Scaling	85
6.7 Summary of the optimisation problem	86
7 Vehicle modelling and parameterisation	87
7.1 Propulsion	87
7.1.1 Resolution of propulsion systems within modelling .	90
7.2 Eclipse	91
7.3 Power	94
7.3.1 Power generation	94
7.3.2 Power consumption	98
7.4 Parameterisation	99
7.4.1 Thrust profile parameterisation	99
7.4.2 Discretisation	100
7.5 Orbital behaviour	102
7.5.1 Gravitational assists	102
7.5.2 Oberth effect and optimal thrust profiles	104
7.5.3 Lunar capture	106
7.6 Summary of vehicle modelling	107
8 Method	109
8.1 Introduction	109
8.2 Developmental procedure	109

8.2.1	Matlab modelling	109
8.2.2	GESOP modelling	109
8.2.3	STK modelling	111
8.2.4	Further GESOP modelling	112
8.2.5	Data analysis	115
8.3	Final trajectory determination	115
8.4	Summary	118
9	Discussion of results	119
9.1	Introduction	119
9.2	Reduced complexity optimisation	119
9.3	Ascent phase	125
9.4	Cruise phase	134
9.5	Propagate phase	141
9.6	Capture phase	148
9.7	Descent phase	156
9.8	Science phase	163
9.9	Validation	167
9.10	Summary	171
10	Conclusion	173
10.1	Summary of major findings	173
10.2	Additions to <i>Lunar Mission BW-1</i> program	174
10.3	Additions to low thrust trajectory optimisation	176
10.4	Conclusions of the research	176
10.5	Future work	177
A	Gravitational potential	181
B	Thruster characteristics	183
B.1	Pulsed plasma thrusters	183
B.2	Thermal arcjet	184

Nomenclature

Notation

Bold text represents a vector. A hat (for example $\hat{\mathbf{r}}$) represents a unit vector. A quantity that is normally a vector that is not in bold (for example r) represents the magnitude of that vector. Parameters are relative to the central body of that phase, except where identified with an astronomical symbol.

\odot	Astronomical symbol for the Sun
\oplus	Astronomical symbol for the Earth
\odot	Astronomical symbol for the Moon
\oplus	Astronomical symbol for Venus
\oplus	Astronomical symbol for Mars
\oplus	Astronomical symbol for Jupiter

Chapter 3

t_0	Start of the phase (symbolic)
t_f	End of the phase (symbolic)
\mathbf{p}	Set of optimisable parameters
\mathbf{x}	Set of state parameters
\mathbf{u}	Set of control variables
F	Cost function
σ	Cost function weighting factor (-)
\mathfrak{L}	Lagrangian (see Section 3.3.3) (symbolic)
λ_i	Equality Lagrangian/KKT multipliers (-)

μ_i	Inequality Lagrangian/KKT multipliers (-)
α	Optimisation step size (-)

Chapter 4

ϵ	Specific orbital energy (m^2s^{-2})
ϵ_k	Specific orbital kinetic energy (m^2s^{-2})
ϵ_p	Specific orbital potential energy (m^2s^{-2})
\mathbf{v}	Velocity of spacecraft (ms^{-1})
μ	Gravitational constant of central body (m^3s^{-2})
\mathbf{r}	Distance of spacecraft from central body (m)
I	Impulse (ms^{-1})
\mathbf{p}	Momentum (kgms^{-1})
I_{sp}	Specific impulse (s, see Section 4.3.1)
g_0	Standard Earth gravity (9.80665 ms^{-2} , Bureau International des Poids et Mesures 1901)
$g(r)$	Classic gravity relative to the primary body at r metres from its centre (ms^{-2})
$m_{exhaust}$	Mass of exhaust (kg)
$v_{exhaust}$	Exhaust velocity (ms^{-1})
Δv	Delta-v (ms^{-1} , see Section 4.3.2)
m	Mass of spacecraft (kg)
\mathbf{T}	Applied thrust (N)
\mathbf{D}	Aerodynamic drag (N)
γ	Velocity vector angle ($^\circ$, see Figure 4.5)
α	Body axis angle ($^\circ$, see Figure 4.5)
ε	Thrust angle ($^\circ$, see Figure 4.5)
r_{SOI}	Radius of sphere of influence (m)
a_s	Semimajor axis of the secondary body's orbit about the primary body (m)
m_s	Mass of the secondary body (kg)
m_p	Mass of the primary body (kg)

Chapter 5

\mathbf{r}	Position of spacecraft relative to primary body (m)
\mathbf{v}	Velocity of spacecraft relative to primary body (ms^{-1})
a	Keplerian element semimajor axis (m)
e	Keplerian element eccentricity (-)
i	Keplerian element inclination ($^\circ$)
ω	Keplerian element argument of periapsis ($^\circ$)
Ω	Keplerian element longitude of the ascending node ($^\circ$)
ν	Keplerian element true anomaly ($^\circ$)
p	Modified equinoctial element semilatus rectum (m)
f	Modified equinoctial element f (-)
g	Modified equinoctial element g (-)
h	Modified equinoctial element h (-)
k	Modified equinoctial element k (-)
L	Modified equinoctial element true longitude ($^\circ$)
$\hat{\mathbf{i}}_r$	Unit vector in radial direction
$\hat{\mathbf{i}}_\theta$	Unit vector tangential to primary body
$\hat{\mathbf{i}}_h$	Unit vector in direction of orbital momentum
Δ_r	Total force acting on spacecraft in the $\hat{\mathbf{i}}_r$ direction (N)
Δ_θ	Total force acting on spacecraft in the $\hat{\mathbf{i}}_\theta$ direction (N)
Δ_h	Total force acting on spacecraft in the $\hat{\mathbf{i}}_h$ direction (N)
$\Delta_{\mathbf{q}}$	Total force on spacecraft due to third bodies (N)
\mathbf{d}_j	Position of third body j relative to spacecraft (m)
\mathbf{s}_j	Position of third body j relative to primary body (m)
Δ_g	Total force on spacecraft due to primary body oblateness (N)
J_2	Second zonal harmonic coefficient of Earth
J_3	Third zonal harmonic coefficient of Earth

J_4	Fourth zonal harmonic coefficient of Earth
W	Orbital energy (J)
Φ	Energy due to angular momentum of orbit (J)
V	Gravitational potential energy of orbit (J)
$\bar{P}_{nm}(\sin \phi')$	Normalised associated Legendre polynomials
$C_{n,m}$	Normalised gravitational coefficient
$S_{n,m}$	Normalised gravitational coefficient
r_{peri}	Periapsis of the orbit (m)
Δ_\odot	Total force on spacecraft due to solar wind (N)
β	Optical reflection constant (-)
A_{eff}	Effective cross-sectional area of spacecraft (m^2)
r_\odot	Distance of satellite from centre of Sun (m)
Δ_T	Total force on spacecraft due to thrust (N)
$\hat{\mathbf{u}}$	Unit control vector governing thrust direction

Chapter 6

E	Energy level in the batteries (J)
P	Net power generation or consumption (W)
Ln	Normalised longitude (-)

Chapter 7

η	Power efficiency
α_u	Half-angle of umbral cone ($^\circ$)
α_p	Half-angle of penumbral cone ($^\circ$)
R_\odot	Radius of the Sun (m)
R_\oplus	Radius of the Earth (m)
\mathbf{r}_\oplus	Position of the Earth from the Sun (m)
\mathbf{r}_\odot	Position of the Moon from the Sun (m)
Q	Solar energy flux (Wm^{-2})
η_a	Area efficiency of solar cells (-)
η_c	Power efficiency of solar cells (-)

η_{DC}	Power efficiency of voltage regulator (-)
Ψ_{\odot}	Angle of Sun on solar panels ($^{\circ}$)
\mathfrak{R}	Power degradation of solar cells (-)
\mathfrak{F}	Equivalent fluence of solar cells (-)

Acronyms

AOCS	Attitude & Orbit Control System
ASTOS	Aerospace Trajectory Optimisation Software
BFGS	Broyden-Fletcher-Goldfarb-Shanno
CAD	Computer Aided Design
CAMTOS	Collocation and Multiple Shooting Trajectory Optimisation Software
CGA	Constrained Genetic Algorithm
COTS	Commercial Off-The-Shelf
CNES	Centre National d'Études Spatiales
DLR	Deutsches Zentrum für Luft- und Raumfahrt
DSN	Deep Space Network
EADS	European Aeronautic Defence and Space Company
ECI	Earth Centred Inertial
ECR	Electron Cyclotron Resonance
EML	Earth-Moon Lagrange point
ESA	European Space Agency
ESOC	European Space Operations Centre
ESTEC	European Space Research and Technology Centre
ET	Ephemeris Time
GCR	Galactic Cosmic Ray
GESOP	Graphical Environment for Simulation and Optimisation
GEO	Geostationary (Earth) Orbit
GSLV	Geosynchronous Satellite Launch Vehicle
GTO	Geosynchronous Transfer Orbit
HEO	High Earth Orbit

HLO	High Lunar Orbit
IAU	International Astronomical Union
ICRF	International Celestial Reference Frame
IEEE	Institute of Electrical & Electronic Engineers
IERS	International Earth Rotation Service
IFR	Institut für Flugmekanik und Flugregelung
IRS	Institut für Raumfahrtssysteme
ISRO	Indian Space Research Organisation
ITRF	International Terrestrial Reference Frame
JAXA	Japanese Aerospace Exploration Agency
JD	Julian Date
JGM3	Joint Gravity Model 3
JPL	Jet Propulsion Laboratory
KKT	Karush-Kuhn-Tucker
LEO	Low Earth Orbit
LLO	Low Lunar Orbit
LP165	Lunar Prospector Gravity Model, degree and order 165
NASA	National Aeronautics & Space Administration
NIMA	National Imagery & Mapping Agency
NLP	Non-Linear Programming
ODE	Ordinary Differential Equation
PPT	Pulsed Plasma Thruster
PROMIS	Parameterised tRajectory Optimisation by direct MultIple Shooting
PTFE	Polytetrafluoroethylene (Teflon TM)
SEL	Sun-Earth Lagrange point
SEPTOP	Solar Electric Propulsion Trajectory Optimization Program
SIMPLEX	Stuttgart Impulsing MagnetoPlasmodynamic thruster for Lunar EXploration
SNOPT	Sparse Nonlinear OPTimiser
SOCS	Sparse Optimal Control Software
SOI	Sphere of Influence
SPE	Solar Particle Event

SQP	Sequential Quadratic Programming
SSO	Sun Synchronous Orbit
STK	Satellite Tool Kit
TALOS	Thermal Arcjet for Lunar Orbiting Satellite
TLI	Trans-lunar Injection
TROPIC	Trajectory OPtimisation by dIrect Collocation
TT	Terrestrial Time
UTC	Universal Coordinate Time

Abstract

The University of Stuttgart is conducting a research program to build a succession of small satellites. The ultimate goal of this program is to build and launch a craft named *Lunar Mission BW-1* (after the federal state that Stuttgart is situated in, Baden-Württemberg) into lunar orbit, for eventual impact with the Moon. As with the majority of space missions, launch cost is a severely limiting factor so it is necessary to carefully plan the trajectory before launch, to ensure lunar capture and minimise the amount of fuel needed by the spacecraft.

This thesis outlines work conducted to find a robust fuel-optimal trajectory for *Lunar Mission BW-1* to reach the Moon. Several unique aspects of this craft require a novel approach to that optimisation. Firstly, the spacecraft uses a new low-cost propulsion system, severely limiting manoeuvrability and accessibility of transfer trajectories. Secondly, to reduce the mass and complexity of moving parts, the solar panels are fixed to the body; consequently, the craft must rotate itself to point its solar panels towards the Sun to recharge. No thrusting can occur during this time. This magnifies the effect of the third design decision, which is to restrict the dry mass of the craft by giving it very little on-board power storage. After approximately an hour of accelerating it is expected to need to coast for several hours to recharge its batteries, resulting in a relatively high frequency stop-go-stop thrust profile.

Due to these constraints, the trajectory optimisation is one of the most complex ever attempted. Since the craft will be built and launched, many simplifications made in purely theoretical studies could not be utilised, such as neglecting the weaker forces acting on the spacecraft in cis-lunar space.

The very low thrust results in very long transfer times, during which even small magnitude forces acting on the spacecraft can significantly perturb its trajectory. However, including these forces creates non-linearities in the equations of motion associated with spacecraft trajectories, limiting the optimisation methods that could be used, and increasing computational complexity.

Optimisation methods for low-thrust spacecraft trajectories have been the subject of much research, but most studies conclude that knowledge is still lacking in this area. Furthermore, many optimisation methods investigated in existing literature are incompatible with the intermittent thrust profile required by the *Lunar Mission BW-1* thrusters. For this reason it was necessary to thoroughly review available optimisation methods and determine which may be adapted to this scenario. The resulting optimisation method was applied to the *Lunar Mission BW-1* scenario to determine an efficient thrusting profile that will get the craft to the Moon.

It was found that very few established optimisation algorithms can support the number of variables required for such a complex, long duration trajectory. The Sparse Optimal Control Software (SOCS) marketed by The Boeing Corporation was used via an interface developed at the University of Stuttgart called the the Graphical Environment for Simulation and Optimisation (GESOP). Due to unknown constraints such as launch date, the phases defined by the mission architecture were modelled and optimised independently. This approach allows mission planning flexibility while still providing reliable estimates for optimal fuel use, mission duration and power limitations.

A trajectory is presented for each of the phases, ascending from the intial geosynchronous transfer orbit (GTO) to the eventual low lunar orbit (LLO). The resulting science phase is propagated forward in time to ensure orbital lifetime meets the mission requirements. Recommendations are subsequently made for the continuing development of the mission architecture.

The primary outcome of this study is a procedure for developing an operational trajectory for *Lunar Mission BW-1* after launch details are

known. Given the current mission architecture and assumed launch details, the thermal arcjet requires 1205.28 hours (50.22 days) of operation while consuming 93.25 kg of ammonia propellant, and the pulsed plasma thrusters require 29176.82 hours (3.33 years) of operation while consuming 18.98 kg propellant. Power constraints were not found to be mission limiting for the current spacecraft configuration. Consequently, although the laboratory testing burden on the PPTs is already quite heavy, it is recommended that the mission architecture be adjusted to shorten arcjet phases and lengthen PPT phases. Furthermore, this project found that the optimisation package SOCS was the best commercially available option for low-thrust trajectory optimisation, but that it would benefit greatly by adaptation to a parallel shooting algorithm that may be distributed amongst multiple computer processors.

Statement of Originality

I, Rogan Shimmin, certify that this work contains no material which has been accepted for the award of any other degree or diploma in any university or other tertiary institution and, to the best of my knowledge and belief, contains no material previously published or written by another person, except where due reference has been made in the text.

I give consent to this copy of my thesis, when deposited in the University Library, being made available for loan and photocopying, subject to the provisions of the Copyright Act 1968. I also give permission for the digital version of my thesis to be made available on the web, via the University's digital research repository, the Library catalogue, and also through web search engines, unless permission has been granted by the University to restrict access for a period of time.

Rogan Shimmin

Date

Acknowledgements

Firstly I would like to thank my principal supervisor Dr Ben Cazzolato for accepting me as his student after Dr Matt Tetlow's departure, bravely taking on a new field of research at the same time. His guidance and support were invaluable to me in finishing this thesis. Thanks also to Dr Vince Wheatley for being my connection with space research during my early days in Adelaide, and of course, thanks to Matt for helping me get started, then lending me his insight and experience in all things optimisation, orbital mechanics, and Stuttgart-related over the course of my work before resuming as my supervisor just in time to review this thesis! Thanks also to the rest of the AIAA Adelaide Section for fostering my dreams of space throughout my university education.

On the other side of the world I'd like to add my gratitude to Prof. Dr Hans-Peter Röser for formalising my stay in Stuttgart and providing me with such an incredible international experience, and the opportunity to work on such an ambitious project with such great people. Heartfelt thanks to the recently appalled Dr-Ing. Oliver Zeile for being my main mentor and sounding board in Germany, but moreso for his unflagging enthusiasm and friendship over the past years. I also owe a debt of gratitude to Dr-Ing. René Laufer for starting the *Kleinsatellitenprogramm* and always being available for long, rambling discussions while I was working on it, but even more for encouraging me to attend the International Space University. A huge thankyou must then go out to the ISU community, for reigniting my motivation and further inspiring me to pursue a career in space.

Big thanks must go to the ASTOS boys, in particular Francesco Cremaschi and Christian Möllman, for their technical support and assistance

with the optimisation software throughout my studies. I really appreciate the time you put in, above and beyond our original agreement.

I wish to thank the Deutscher Academischer Austauch Dienst (DAAD) for financial support during my stay in Germany, and thanks also to the people of The School of Mechanical Engineering at The University of Adelaide, and the Institut für Raumfahrtsysteme at Universität Stuttgart for facilitating my work on such a fantastic project in two top quality research environments. Deserving of special mention are Billy Constantine, for keeping my computer in brilliantly working order in Adelaide, Edgar Schreiber, for trying to do the same in Stuttgart, and Kay Leverett, for her patient guidance through The University of Adelaide's library resources regardless of where in the world I was.

I really could not have finished this project without the support of my friends in Stuttgart and Adelaide, and elsewhere around the world. You guys really gave me the motivation to finish this thing! Here I really have to single out Tristan Williams, for lending many hours of programming expertise remotely from Helsinki. Last but perhaps most importantly, sincere thanks to my family, who have always supported me throughout my studies. Special thanks go to Mum for making me take this task on in the first place, and Dad for looking after Orlando during my lengthy absences.

Chapter 1

Introduction

1.1 Historical background

The idea of electric propulsion was first published by Konstantin Tsiolkovsky in 1911 (Choueiri 2004). During the 1960s when space travel was becoming a reality, the theory of electric propulsion was extended to low-thrust spacecraft transfers. Unfortunately there were many technological hurdles to realising these thrusters as primary propulsion at the time, so interest in the topic waned. From the early 1990s, enough of these hurdles were overcome to allow the first electric spacecraft thrusters to be developed and tested. Since then there has been a resurgence of research into how best to utilise low thrust engines in missions ranging from Earth orbit transfers to interstellar travel.

The advantage of low-thrust propulsion is that it is capable of delivering a greater payload fraction compared to conventional chemical propulsion systems, as highlighted in literature such as Kluever and Pierson (1995) and Yang (2007). Greater payload fraction means less fuel mass is required to propel a given payload into orbit. This results in large savings, because as Manzella (2008) points out, despite advances in launch-vehicle technology over the past 40 years, the cost of space launch has remained nearly constant at around USD\$10,000 per kilogram.

The aim of this project was to design a fuel-optimal lunar trajectory

for a specific very-low-thrust, power-limited spacecraft.

1.2 *Lunar Mission BW-1*

The inspiration for this project came from the Small Satellites Program (*Kleinsatellitenprogramm*) being run at the Institut für Raumfahrtssystem (IRS) of Universität Stuttgart. The ultimate objective of this program is to launch the craft *Lunar Mission BW-1* to the Moon, as proposed by Röser et al. (2006). The latest CAD model of the vehicle is shown in Figure 1.1. Immediately apparent are the 6 square metres of triple junction gallium arsenide solar panels, which fold up against the cubic metre body for launch. The communications dishes are fixed with respect to the frame, and consist of an S-band dipole antenna for good atmospheric penetration, and a parabolic Ka-band antenna that provides higher bandwidth (and therefore data rate) but is more susceptible to weather conditions.

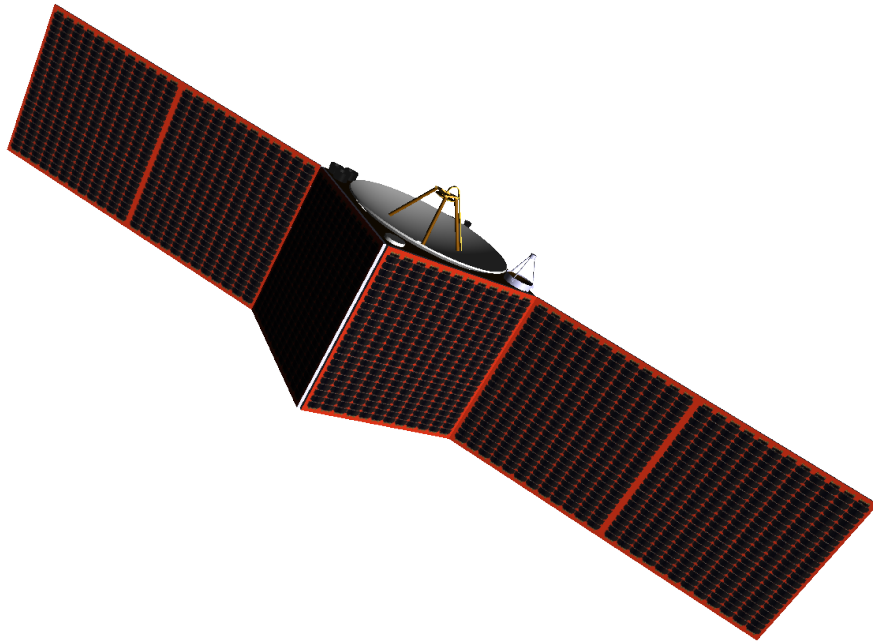


Figure 1.1: Lunar Mission BW-1

Lunar Mission BW-1 will be propelled by a combination of Pulsed

Plasma Thrusters (PPTs), developed at IRS by Nawaz et al. (2008) and a thermal arcjet similarly developed at IRS by Bock et al. (2007). Performance parameters for these thrusters based on laboratory tests are listed in Table 1.1. The thrusters will be arranged as seen in Figure 1.2, with an arcjet surrounded by four PPTs. This arrangement was recommended to allow reaction wheel desaturation in pitch and yaw; the deflector plate was a conceptual idea to allow roll desaturation. The author declines to comment on the efficacy of this mechanism, as it is well outside the scope of this project.

Table 1.1: *Performance parameters of Lunar Mission BW-1 thrusters*

Propulsion system	Arcjet	PPT
Number of active units	1	4
Power required per unit (W)	801	52
Thrust produced per unit (mN)	102.5	1.22
Exhaust velocity (ms^{-1})	4768	27000

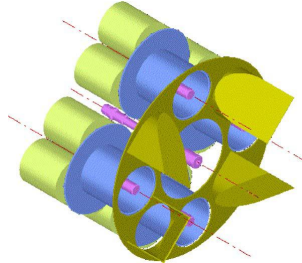


Figure 1.2: *Arrangement of arcjet (centre) and 4 PPTs on Lunar Mission BW-1, with a conceptual mechanism allowing for thrust vectoring. Image used courtesy of Röser et al. (2006).*

Due to the design decision to fix both the solar panels and the thrusters with respect to the body, the spacecraft will have to alternate between thrusting along the desired vector with reduced power generation, and coasting in order to orient the solar panels towards the sun. Consequently on-board power storage is required, to hold the charge generated during the coasting arcs and discharge it during the thrust arcs.

Table 1.2: *The phases of Lunar Mission BW-1, as published by Institut für Raumfahrtssysteme, Universität Stuttgart (2008).*

Phase	Objective
Launch	The spacecraft is delivered into Geosynchronous Transfer Orbit (GTO).
Ascent	The spacecraft's orbit is extended above the van Allen belts using the arcjet.
Cruise	Orbit extension up to lunar gravitational sphere of influence using PPTs.
Capture	Insertion into highly elliptical lunar orbit using the arcjet.
Descent	Transfer of the satellite into a high, inclined circular orbit (approximately 100 km altitude) using PPTs.
Science	Remote sensing of the surface of the Moon (stable orbit requiring minimal stationkeeping; however energy requirements are increased by scientific instruments and data transfer).
Impact	Controlled impact of the satellite onto the lunar surface using the arcjet.

The *Lunar Mission BW-1* mission architecture has been broken down into the seven phases shown in Table 1.2. Phase one is expected to be provided by a commercial launch vehicle such as the Indian Space Research Organisation (ISRO)'s Geosynchronous Satellite Launch Vehicle (GSLV), seen in Figure 1.3, which launches from Sriharikota, India. Phase two, concerning ascent from GTO to an orbit above the van Allen belts, has undergone preliminary analysis by Letterio (2005). Phase four has undergone preliminary study by Möllman (2005), while the specifications for the lunar orbit (phase six) have been developed by Zeile et al. (2010). Various impact scenarios have been developed by Trawny et al. (2004). The research presented in this thesis brings these preliminary studies together, including more detailed and accurate constraints, and examines the inter-dependencies between phases 2 to 5.



Figure 1.3: *Indian Geosynchronous Satellite Launch Vehicle. Image used courtesy of ISRO.*

1.3 GESOP

Lunar Mission BW-1 is intended to feature and exploit as much in-house technology as possible, a philosophy that extends to mission design tools. Trajectory optimisation in particular has a long heritage at Universität Stuttgart. In 1989 a number of optimisation algorithms were coded for specific application to trajectory optimisation at Deutsches Zentrum für Luft- und Raumfahrt (German Centre for Aeronautics and Astronautics, DLR) in Oberpfaffenhofen. This project was continued at the Institut für Flugmekanik und Flugregelung (Institute of Flight Mechanics and Flight Control, IFR) in Stuttgart from 1994 and designated GESOP (Graphical Environment for Simulation and Optimisation). A graphical front end and model library was developed for this software called ASTOS (Aerospace Trajectory Optimisation Software), shortly before the development was privatised under the name ASTOS Solutions GmbH. The development continues in close cooperation with the university, so it was suggested that

by using ASTOS less detailed knowledge of the optimisation process would be needed for the project. Midway through the project it was discovered that the ASTOS interface was too restrictive for the task, so the dynamics were modelled in C and applied to the GESOP programming interface.

1.4 Summary

A mission called *Lunar Mission BW-1* is being pursued by the University of Stuttgart Institute for Space Systems. This mission is intended to feature in-house technology. A coarse mission architecture has been established, but needs to be refined and optimised for fuel efficiency. This project aims to take initial steps towards that goal, by modelling the system and performing some optimisation using the program GESOP. This mission design will help quantify whether a relatively low cost mission, with a very low thrust propulsion system, is capable of reaching the Moon, and further into the solar system. This will hopefully encourage other universities and associated groups around the world to launch their own missions, and bring electric propulsion into more mainstream use.

Chapter 2

Scope of research

2.1 Introduction

Published studies in the area of low-thrust trajectory optimisation, such as Petropoulos et al. (2007), frequently conclude that available optimisation techniques require further improvement, particularly in the areas of global search and modelling fidelity. Thus the most important question in this research project is how best to optimise a low-thrust trajectory.

The primary objective of optimising a low-thrust trajectory leads into two very interesting secondary outcomes of this project. Firstly, investigating the severity of perturbing forces on the spacecraft during transit, and to what extent they can be exploited. Secondly, developing a robust model to include a variety of non-linear trajectory constraints in the optimisation process.

2.2 Optimisation of a low-thrust trajectory

The broad objective of optimising a low-thrust trajectory was broken down into the following tasks.

1. Derive an appropriate model for the spacecraft, moving within a realistic space environment.

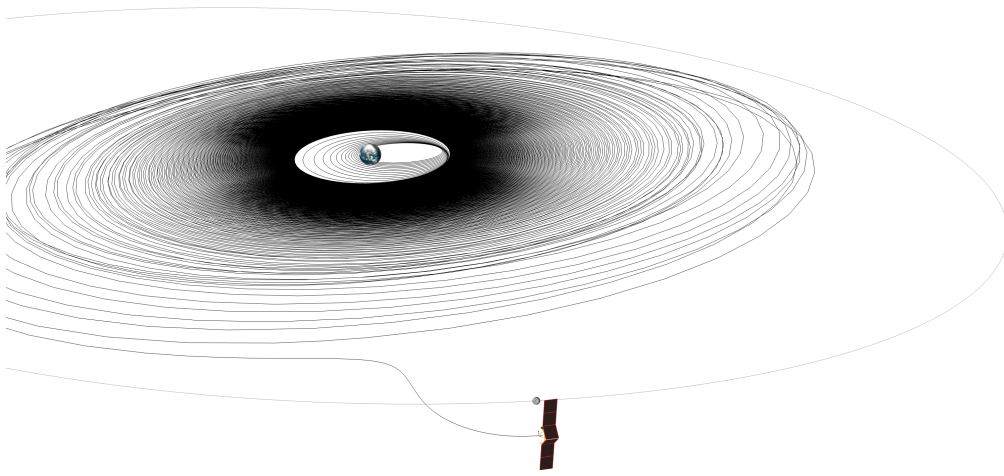


Figure 2.1: A simplified trajectory prepared for demonstration purposes early in the Kleinsatelliten program.

2. Examine optimisation techniques and select one appropriate to this scenario.
3. Explore different initial guesses for the optimisation, based on knowledge of orbital mechanics and exploitation of perturbing forces.
4. Apply non-linear constraints to the optimisation.

2.2.1 Modelling

A complete description of the spacecraft and space environment model is presented in Chapter 5. Although there are multiple solutions available for each modelling hurdle, there are fairly well established best-practice solutions for the high fidelity modelling required over the long durations associated with low-thrust missions.

2.2.2 Investigation of optimisation techniques

Optimisation techniques suitable for trajectory optimisation were examined. Reviewed literature repeatedly cited the inadequacies of existing

search methods as a major problem with existing optimisation methods, as addressed in detail in Chapter 3. In particular, it was noticed that previous optimisations generally ignore non-linear thruster constraints, due to the additional complexity and stiffness they add to the optimisation problem. Therefore finding a computationally efficient way to include non-linear constraints over long time spans was essential to the suitability of the optimisation techniques used for this mission.

2.2.3 Exploring different initial guesses

Most optimisation techniques require an initial guess of the solution to be input into the algorithm, from whence they can improve their objective function. Existing search methods often have strong dependencies on the initial guess, as addressed frequently in literature such as Dachwald (2005). Consequently it is important to investigate the performance of the optimisation under a variety of initial guesses. Based on orbital mechanics theory, a number of potentially optimal scenarios were investigated in this thesis, as outlined in Chapter 8. These were then compared to a number of randomly chosen initial guesses, to determine the breadth of the basin of convergence and the ability of the optimiser to handle multiple basins. Additionally a number of severely sub-optimal initial guesses were examined.

2.2.4 Application of non-linear constraints

There are a number of very unique constraints on *Lunar Mission BW-1*. The thrusters produce substantially less thrust than modelled in most previous studies, resulting in a much narrower range of possible trajectories. The craft used in this program is also very limited by onboard power storage. This is yet another practical engineering issue barely considered in existing literature. Every few hours the craft must rotate to point its solar panels towards the Sun, and recharge its batteries. Once fully charged, it then rotates back to continue thrust vectoring for guidance control. Consequently the optimisation model must allow for variable thrust, including

the ability to constrain thrust magnitude (to zero) at certain times. Developing a method to optimise intermittent thrust profiles like this will ensure the theoretical research of trajectory optimisation is applicable to real spacecraft.

First, a highly simplified low-thrust lunar trajectory was developed. This assisted in developing an initial guess for the final optimisation. From this state, the optimiser was developed to include more complex constraints. Coast phases were introduced to the existing constant-thrust profile, producing a bang-bang control scenario. Then the length of these coasting and thrusting phases was released, followed by the magnitude of the thrust. The electric power consumed during a thrust phase was modelled, with the constraint that it cannot drop below zero. An approximation of power generated by the solar panels was implemented, and then improved based on sunlight angle of incidence, Earth shadow and solar panel decay. This technique identified coasting phases required for recharging the spacecraft, providing constraints on the Attitude Control System (ACS). Propellant use was modelled, based on the thrust profile and constrained by power availability. Reaction wheel desaturation will be required to improve the fuel usage model, although this improvement is dependent on other project members working on the ACS and consequently has not been addressed.

2.3 Investigation of perturbations

This project provides a rare opportunity to actually test a low-thrust trajectory in orbit. Due to the prohibitive cost of space exploration, most studies of this nature are purely academic. Academic studies such as Betts (2000) often simplify or neglect the more awkward perturbing forces acting on the spacecraft such as solar wind and inhomogeneous gravity fields, for the sake of elegant mathematical solutions. The combination of very-low-thrust and the fact that the trajectory resulting from this study will actually be flown, requires that it take into account a much greater range of possible perturbations than most previous studies. The question of how

significant these perturbations are, and particularly to what extent they may be exploited to reduce the effort needed to propel the spacecraft towards the Moon, may greatly affect the final launch.

To address this question, once a robust model was developed for the trajectory optimisation, the impact of perturbations on the trajectory was investigated. This objective was required to highlight two major characteristics of the trajectory: firstly, the robustness of the trajectory in the event of unanticipated perturbations, and secondly whether anticipated perturbing forces may be exploited to propel the spacecraft.

It is well known from interplanetary trajectories such as those presented by Petukhov et al. (2007) that a large amount of propulsive effort can be saved by exploiting gravitational assists. Some textbooks, such as Kemble (2006), and other publications such as Letterio (2005) discuss the possibility of exploiting the Moon’s gravity in a series of lunar “resonances” to assist a low thrust lunar transfer. A small number of missions have succeeded in doing this, such as NASA’s ARTEMIS (Angelopoulos 2011, Sweetser et al. 2011). These anticipated perturbations are implicitly exploited by the optimiser since they represent optimal scenarios, however due to imperfections in optimisation algorithms the initial guess strongly affects whether the gravitational assist is found.

2.4 Investigation of non-linear constraints

As additional constraints and non-linearities were progressively added to the model, the impact of each constraint on the behaviour of the optimisation process was investigated to determine its effect on both the optimisation process and the resulting optimal trajectory. Optimal intermittent thrust profiles were compared with results for a comparable continual thrust profile to demonstrate the improvement (for example, thrusting twice as much at periapsis and then coasting compared to thrusting continuously throughout the orbit).

Other issues that were addressed in this project, that have been neglected or ignored in most previous studies, include the spacecraft tran-

siting through the Earth's shadow (eclipse), the possibility of varying the thrust level to conserve power, integrating the probable battery charge level throughout the transfer (based on sunlight received versus power used), intervals required for attitude control and reaction wheel desaturation and the amount of propellant required, and position monitoring and communication windows from the available groundstations. Many of these non-linear constraints have not been considered in previous studies, so the question of how to mathematically represent them such that they may be included in the optimisation is very important.

2.5 Limits of the scope

It was anticipated that by judiciously choosing the thrust phases, the fuel efficiency could be improved. However, there are always limitations to such a project. The optimal thrust profile for this mission is very closely tied to the Attitude Control System (ACS). This provides further constraints on the project, and adds another whole level of modelling complexity. However, the ACS for *Lunar Mission BW-1* is still being finalised and will be tested on the forthcoming test satellites *Flying Laptop* and *Perseus*. Consequently modelling and optimising the ACS is beyond the scope of the project.

Throughout this thesis it is assumed that the ACS can provide the attitude required, when required, for as long as required. A corollary of this assumption is that the spacecraft may be modelled as a point mass. Another consequence is that reaction wheel saturation cannot yet be predicted. Thus reaction wheel desaturation could not be included in this project, although given the rotation rate of 1° per second specified in the design it is anticipated that the time required to reorient the spacecraft will have minimal effect on the thrust profile.

A thorough outline of factors influencing the trajectory is presented in Table 2.1. Many of the factors have been considered and subsequently neglected, usually for reasons presented later in this thesis. Some depend on design parameters that are yet to be defined, but have been accounted

for in the model.

2.6 Summary of research scope

Several fundamental objectives have been outlined for optimising the trajectory of *Lunar Mission BW-1*. These objectives include establishing reliable modelling and optimisation techniques within the Institute for Space Systems, determining efficient ways to model the non-linear forces present on an exo-atmospheric trajectory, and investigating how significant those forces are over the course of the the trajectory. Establishing some ground rules for practically optimising the trajectory of a spacecraft in this manner will improve the existing knowledge of low-thrust spacecraft trajectories.

Table 2.1: Inclusion of factors influencing the spacecraft trajectory.

Factor	Inclusion
Perturbing forces	
Primary gravity	Inherent in equations of motion
Earth gravity field	JGM3 included in Moon-centred phases to degree and order 20
Moon gravity field	LP165 included in Earth-centred phases to degree and order 20
Sun gravity	Included
Mercury gravity	Not included
Venus gravity	Included
Mars gravity	Included
Jupiter gravity	Included
Saturn gravity	Not included
Solar wind	Included as a time-average
Vehicular constraints	
Thruster duty cycle	Neglected (see Section 7.1)
Thruster power	Included (see Section 7.1)
Solar panel power	Included (see Section 7.3.1)
Payload power	To be defined (see Section 7.3.2)
Communications power	To be defined (see Section 7.3.2)
Battery capacity	Included (see Section 7.3)
ACS	Neglected (see Section 2.5)
Reaction wheel desaturation	Neglected (see Section 2.5)
Communications windows	To be defined (see Section 7.3.2)
Navigation windows	To be defined
Observation windows	To be defined
Thermal effects	Neglected
Environmental considerations	
Radiation	Neglected (see Section 4.2.1)
Debris	Neglected (see Section 4.2.2)
Eclipse	Included (see Section 7.2)

Chapter 3

Review of relevant literature

3.1 Introduction

There are two major fields of literature relevant to this project. Firstly, studies and technical reports delivered within engineering organisations relating to real spacecraft missions are examined, and compared to *Lunar Mission BW-1*. Secondly, there has been a long history of theoretical study into optimising spacecraft trajectories, from early impulsive space-craft research to more recent low-thrust scenarios. A brief explanation of optimisation theory is provided, followed by a more in-depth investigation into recent application of these methods to low-thrust trajectory optimisation.

3.2 Past missions

While LePage (1991) shows that there have been numerous Earth-orbiting satellites using electric thrusters for attitude control or station keeping, only a small number of spacecraft have ever escaped the Earth's sphere of influence using electric propulsion as the primary thrust. These are listed in Table 3.1, along with key specifications of their respective propulsion systems. Within the table, *thrust* represents the maximum force that the primary propulsion system can exert on the craft. *Power consumption* is

the amount of electrical power used to operate at this maximum thrust. *Specific impulse*, I_{sp} , is the momentum added by the thrusters per unit weight-on-Earth of propellant, and consequently represents the fuel efficiency of the thrusters. Electric propulsion is characterised by relatively high I_{sp} .

Table 3.1: Past low-thrust missions to escape Earth's sphere of influence

Spacecraft	Propulsion type	Total Power Consumption (W)	Total Thrust (mN)	I_{sp} (s)
DS-1 ^a	Electrostatic Ion Thruster	2100	92	3300
Hayabusa ^b	4× Microwave ECR Thrusters	1400	32	3200
SMART-1 ^c	Hall Effect Thruster	1200	73	1640
Dawn ^d	Electrostatic Ion Thruster	2100	90	3100
Lunar Mission BW-1 ^e	4× Pulsed Plasma Thrusters	220	4.9	2753
	Thermal Arcjet	801	103	486

^aJet Propulsion Laboratory (2008b)

^bJapanese Aerospace Exploration Agency (2008)

^cEuropean Space Agency (2008b)

^dJet Propulsion Laboratory (2008a)

^eInstitut für Raumfahrtssysteme, Universität Stuttgart (2008)

For the purposes of comparison, the Apollo program trans-lunar injection (TLI) was performed using a chemical propulsion system providing a thrust of approximately 1 MN (9 orders of magnitude greater than *Lunar Mission BW-1*) on a mass of 119,900 kg (only 3 orders of magnitude greater than *Lunar Mission BW-1*) at a specific impulse of 421 s. The Saturn V third stage that performed the TLI is shown at launch in Figure 3.1.



Figure 3.1: *Saturn V from the Apollo program. Image used courtesy of National Aeronautics and Space Administration (2012).*

3.2.1 Deep Space One

Deep Space One (DS-1), shown conceptually in Figure 3.2, was launched on 24 October 1998 with a mass of 374 kg (Jet Propulsion Laboratory 2008b). After launch, an electrostatic ion thruster took over propulsion on its one-way mission to the asteroid *9969 Braille* and the comet *19P/Borrelly*. This thruster generated 92 mN of thrust at a maximum input power of 2100 W.

DS-1 had several similarities to the intended mission of *Lunar Mission BW-1*. Rayman and Lehman (1997) state that once or twice each week the spacecraft had to rotate away from its thrust vector in order to collect optical navigation data and communicate with the Deep Space Network (DSN) on Earth, which required shutting down the propulsion system.



Figure 3.2: *Deep Space One.* Image used courtesy of Jet Propulsion Laboratory (2008b).

Key differences from *Lunar Mission BW-1* however, include the frequency and duration of these thrusting and coasting phases, and the nature of the trajectory. The interplanetary trajectory of DS-1 was dominated by a heliocentric orbit, with gravity assists from the Earth, Mars and a number of asteroids. This means that the thrust vector was almost tangential to the orbital velocity around the Sun, and therefore the optimal orientation of solar panels (towards the Sun) was always perpendicular to the desired thrust vector (around the Sun). In contrast to this, *Lunar Mission BW-1* will occupy a cis-lunar orbit. This poses two difficulties: not only will the trajectory optimisation have to switch its reference frame from Earth-centric to lunar-centric in mid-flight, but optimal orientation of the solar panels relative to the direction of thrust is constantly changing. To overcome this the thrusting profile of *Lunar Mission BW-1* must shut down much more frequently than DS-1 did: hourly, rather than weekly, so that it can point its solar panels towards the Sun to recharge.

Rayman et al. (1999) provide a brief outline of the optimisation strategies used to design the DS-1 trajectory. A legacy in-house routine called the Solar Electric Propulsion Trajectory Optimization Program (SEP-

TOP) was used to determine an initial guess, implementing a calculus-of-variations optimisation technique. To reduce computational complexity, the heliocentric trajectory was constrained to month-long thrust arcs with a thrust vector fixed relative to a rotating frame. SEPTOP was then used to perform sensitivity analysis and to examine failure scenarios, before the coarse trajectory was then refined in a custom-built tool called the Computer Algorithm for Trajectory Optimization (CATO). This trajectory was then uploaded to the on-board navigation system AutoNav.

3.2.2 Hayabusa

Hayabusa (launched 9 May 2003), shown conceptually in Figure 3.3, was designed by the Japanese Aerospace Exploration Agency (JAXA) to perform a rendezvous with asteroid *25143 Itokawa* (Japanese Aerospace Exploration Agency 2008). It had a launch mass of 510 kg, including 130 kg of xenon gas used by the four microwave ECR (Electron Cyclotron Resonance) thrusters, providing $4 \times 8 \text{ mN} = 32 \text{ mN}$ thrust at maximum input power of $4 \times 350 \text{ W} = 1400 \text{ W}$.

Hayabusa had a similarly weak thrust to *Lunar Mission BW-1*, but was once again in a heliocentric orbit. Hayabusa successfully re-entered Earth's atmosphere and was recovered near Woomera, South Australia in June 2010, despite numerous failures including almost complete failure of all four ECR thrusters. The original trajectory design was published by Masatoshi et al. (2003) in Japanese, but remains unverified due to the repeated major revisions required due to system failures.

3.2.3 SMART-1

Small Missions for Advanced Research in Technology One (SMART-1) (launched 27 September 2003) had a Hall effect plasma thruster providing 73 mN thrust at 1200 W power consumption (European Space Agency 2008b). The craft, shown conceptually in Figure 3.4, was a comparable size to *Lunar Mission BW-1*, but twice as heavy: 367 kg including 80 kg of xenon propellant. On September 3, 2006 SMART-1 was deliberately

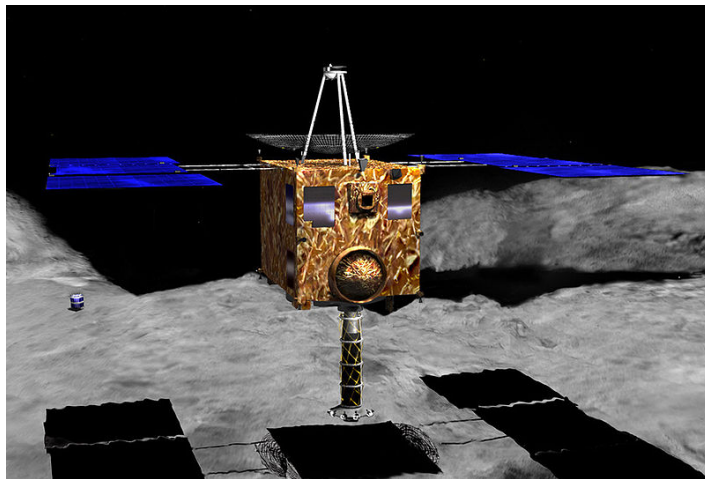


Figure 3.3: Japanese *Hayabusa* probe. Image used courtesy of National Space Science Data Center (2008).

crashed into the Moon’s surface. This mission profile is closest to that intended for *Lunar Mission BW-1*, but had an order of magnitude higher thrust.

Unlike *Lunar Mission BW-1*, SMART-1 had a mechanism to adjust the solar panel angle relative to the body to maximise incident sunlight. Estublier et al. (2007) provides a useful summary of SMART-1 performance data, including that the GaAs solar panel performance started at 23.7% efficiency, and decayed to 18-19%. To allow continued thrusting during eclipse, Li-ion batteries were included allowing up to 2.1 hours of thrust. The Snecma PPS-1350G Hall effect thruster was mounted on a gimbal to allow reaction wheel unloading.

Schönmäkers (2004) outlines the procedure and design factors influencing the trajectory design, but does not expound on optimisation methods used. Amongst a comprehensive summary of the entire mission and spacecraft design, Racca et al. (2002) provides some information on the techniques used. SMART-1’s first phase (GTO to 20,000 km periapsis) simply thrusted continuously along the orbital tangent. Phases 2 (cruise to 338,000 km apoapsis) was optimised using the Pontryagin maximum principle, by optimising the length of thrust and coast arcs within each orbit. Out-of-plane components were allowed, particularly during the higher



Figure 3.4: SMART-1. Image used courtesy of U.S. Geological Survey (2008).

orbits later in the phase, to perform a plane change. The third phase, incorporating the difficult lunar capture, utilised a gradient projection method to optimise a set of parameters defining the control law, thereby limiting the computational complexity of optimising a continuously variable thrust vector. Finally, the lunar descent from 60,000 km once again used the Pontryagin maximum principle to optimise the right ascension of the ascending node and arrival epoch of the final LLO, although thrust was constrained to the negative velocity vector thus severely limiting the computational complexity of the optimisation. Backwards integration was used to avoid the difficulties associated with lunar capture.

3.2.4 Dawn

Dawn (launched 27 September 2007) is using the same thrusters developed for DS-1 to propel it towards the dwarf planet *1 Ceres* by 2015 (Jet Propulsion Laboratory 2008a), following a successful rendezvous with the main-belt asteroid *4 Vesta* in June 2011. Getting to Vesta it consumed 275 kg xenon, and will use another estimated 110 kg to get to Ceres, out

of a total of 425 kg of on-board propellant. Dawn, shown conceptually in Figure 3.5, had a total launch mass of 1250 kg.

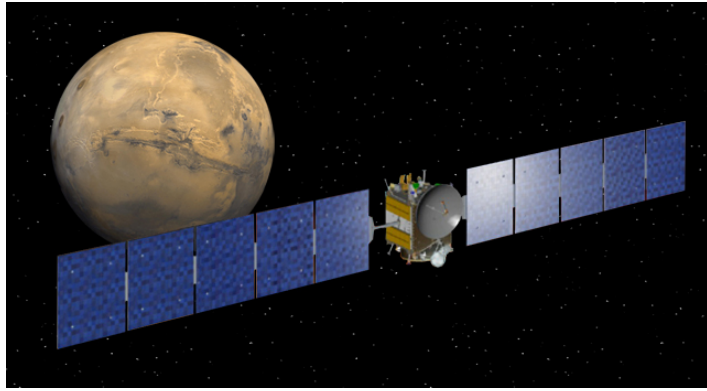


Figure 3.5: Dawn. Image used courtesy of Jet Propulsion Laboratory (2008a).

Genetic algorithms and simulated annealing were investigated during Dawn mission planning (Lee et al. 2005a), but the mission resorted to the same optimisation methods used by Deep Space-1 (Rayman et al. 2007).

3.2.5 Planned missions

Planned electrically propelled missions include SMART-2, also known as LISA Pathfinder (European Space Agency 2008a), and Space-Technology 7 (ST-7) to be launched by NASA. Common to all of these missions is thrust substantially higher than *Lunar Mission BW-1* will have available, and consequently *Lunar Mission BW-1* will have a less flexible escape trajectory.

Lunar Mission BW-1 will be only the fifth electrically propelled space-craft to leave Earth orbit, and the first mission with this type of electric propulsion. To increase its chances of success, a fuel-optimal trajectory must be sought.

3.3 The process of optimisation

Optimisation is, intuitively, the process of finding an optimum value (minimum or maximum) for a given function. This is achieved by defining an *objective function* or *cost function* to rank results based on perceived value, allowing the result with the highest value to be chosen. The difficulty of performing optimisation arises from the potentially large number of results, and the difficulty of mathematically defining what is “good” or “bad”.

3.3.1 Problem formulation

Typically, optimal control problems are formulated to find the required control history $\mathbf{u}(t)$ to deliver something (in this case, a vehicle) from an initial state $\mathbf{x}(t_0)$ to a final state $\mathbf{x}(t_f)$ while minimising the cost function F , where t is some smoothly increasing or decreasing parameter.

Along with the control history there are several other parameters (such as departure date, slackness within the initial and final conditions, and phase lengths) that make up the optimisable parameter set \mathbf{p} . The generic optimisation problem is

$$\min F(\mathbf{u}(t), \mathbf{p}). \quad (3.1)$$

This optimisation is, of course, subject to certain equality constraints g_{eq} and inequality constraints g_{ineq} which depend on the state \mathbf{x} , control parameters \mathbf{u} , optimisable parameters \mathbf{p} and independent parameter t ,

$$g_{eq}(\mathbf{x}(t), \mathbf{u}(t), \mathbf{p}, t) = 0, \quad (3.2a)$$

$$g_{ineq}(\mathbf{x}(t), \mathbf{u}(t), \mathbf{p}, t) \geq 0. \quad (3.2b)$$

The differential equation (3.3) then describes how the state evolves over the trajectory,

$$\frac{d\mathbf{x}}{dt} = f(\mathbf{x}(t), \mathbf{u}(t), \mathbf{p}, t). \quad (3.3)$$

For computational reasons (see Section 6.6.2), upper and lower bounds

are supplied for the states, controls and optimisation parameters,

$$\mathbf{x}_l \leq \mathbf{x}(t) \leq \mathbf{x}_u, \quad (3.4a)$$

$$\mathbf{u}_l \leq \mathbf{u}(t) \leq \mathbf{u}_u, \quad (3.4b)$$

$$\mathbf{p}_l \leq \mathbf{p} \leq \mathbf{p}_u. \quad (3.4c)$$

The cost function F must be defined with the same parameters, but may include components evaluated at the start of the trajectory, end of the trajectory, and integrated over the trajectory, added together with appropriate weighting factors σ ,

$$F_0 = f(\mathbf{x}(t_0), \mathbf{u}(t_0), \mathbf{p}, t_0), \quad (3.5a)$$

$$F_f = f(\mathbf{x}(t_f), \mathbf{u}(t_f), \mathbf{p}, t_f), \quad (3.5b)$$

$$F_i = \int_{t_0}^{t_f} f(\mathbf{x}(t), \mathbf{u}(t), \mathbf{p}, t) dt, \quad (3.5c)$$

$$F = \sigma_0 F_0 + \sigma_f F_f + \sigma_i F_i, \quad (3.5d)$$

where the subscripts 0, f , and i represent initial, final and integrated cost functions, respectively.

3.3.2 Trajectory propagation

The path between initial and final states is defined by a differential equation of motion as outlined in equation (3.3). A number of numerical methods are available for approximating the solution to differential equations such as these. In general, the gradient at some starting point is used to estimate another point a small distance away. Most common are the Runge-Kutta methods, which use an iterative estimate of the gradient at the midpoint to get a more accurate estimate for the endpoint. The fourth

order Runge-Kutta method for $y' = f(t, y)$ is calculated by

$$y_{n+1} = y_n + \frac{1}{6} (k_1 + 2k_2 + 2k_3 + k_4), \quad (3.6a)$$

$$k_1 = hf(t_n, y_n), \quad (3.6b)$$

$$k_2 = hf\left(t_n + \frac{h}{2}, y_n + \frac{k_1}{2}\right), \quad (3.6c)$$

$$k_3 = hf\left(t_n + \frac{h}{2}, y_n + \frac{k_2}{2}\right), \quad (3.6d)$$

$$k_4 = hf(t_n + h, y_n + k_3), \quad (3.6e)$$

where h is the step size (Kreyszig 1979, p. 797). A similar, commonly used method in optimal control is Hermite-Simpson interpolation (Kreyszig 1979, p. 197).

Adaptive Runge-Kutta methods use the difference between two fixed-step Runge-Kutta methods to place bounds on the accuracy of the estimated endpoint. If the accuracy is not within some predefined tolerance, the interval size is revised. Particular care must be taken when integrating a non-linear differential equation over an extended duration such as the *Lunar Mission BW-1*, due to the accumulation of numerical errors.

Regardless of the numerical method used, trajectory optimisation requires solving the differential equations over a span of time; low-thrust trajectory optimisation requires very long timespans. Every integration step is associated with a potential error, which accumulates over the timespan. Methods that integrate from the start to the finish, termed *direct shooting* or *single shooting* methods, become increasingly error-prone as the timespan increases. Small changes early in the trajectory create large changes later on, which can make the constraints behave very non-linearly (Betts 1998).

If some intermediate states can be reliably guessed, the integration may be started anew from that “node”. Any discontinuity at the node is added to the set of constraints, resulting in a relatively larger number of optimisation variables. Methods that perform multiple independent integrations like this, termed *multiple shooting* methods, are less prone to integration

error, but convergence is heavily dependent on the accuracy of the intermediate state guesses (Betts 1998, Fischer et al. 2008). Consequently, many multiple shooting methods now incorporate automatic initial guess estimation. Multiple shooting is sometimes called *parallel shooting*, because each segment may be calculated in parallel. This method therefore lends itself well to parallel processing, across multiple core processors or even clusters of networked computers.

Finally, to reduce computational complexity the changes in control and/or state over time may be approximated by a piecewise linear or polynomial function. Any algorithm that uses a simplification like this is said to solve the *parameterised optimal control problem*. If the algorithm approximates control and state nodes at the same points, it is a *collocation* method. Since this reduces the number of nodes required, collocation is generally faster than multiple shooting, but not as accurate.

3.3.3 Optimisation methods

Any trajectory propagated as in Section 3.3.2 that satisfies the boundary value problem stated in Section 3.3.1, within acceptable error bounds, is a potential solution to the optimal control problem. These solutions may then be ranked using the objective function presented in equation (3.5). The remaining task is to evaluate enough potential solutions to be confident that the highest scoring one is indeed optimal.

There are two general approaches to this problem, classified consistently across literature such as Betts (1998) and Fischer et al. (2008). *Indirect methods* attempt to solve the derivative of the cost function and thus determine a stationary point in the function space. *Direct methods* simply evaluate the cost function at a number of nearby points in the function space, and repeat the process from the best solution found. Once no adjacent points in the function space possess better costs, an optimum has been attained. Both of these methods satisfy the necessary and sufficient conditions of an optimum.

Necessary and sufficient conditions

Pierre de Fermat first proved that optima of unconstrained problems are found at stationary points in the objective function (Fermat 1891–1912). The addition of inequality constraints adds some complexity in that the global optimum may be located on the edge of the acceptable set; that is, where an active constraint disallows any points deeper along the gradient. These constraints may be appended to the objective function to form a *Lagrangian*, which modifies the overall problem into an unconstrained set. Because this test requires the gradient or first derivative of the Lagrangian (called the *Jacobian*) to be calculated, it is called a *first order condition*. Satisfying the first order condition is necessary for the point to be a local optimum.

While the first order test identifies points that might be optima, it does not distinguish a minimum from a maximum or an inflection point. When the objective function is twice differentiable, these cases can be distinguished by checking the second derivative (the gradient of the gradient, called the *Hessian*). The conditions that distinguish maxima, or minima, from other stationary points are called *second order conditions*. If a candidate solution satisfies the first order conditions, then satisfaction of the second order conditions is sufficient to establish at least local optimality.

Indirect methods rely on these tests to determine search direction. Direct methods include these tests implicitly by adjusting the search space towards the most favourable solution (consequently along the steepest gradient) until there is no more favourable solution nearby (the gradient is zero). If the second order test were not satisfied, better solutions would be found adjacent to the candidate solution. Both types of methods require evaluation of the Lagrangian.

Lagrangian

As mentioned above, adding the constraints to the cost function transforms the constrained problem into an unconstrained problem. The resulting cost

function is known as the Lagrangian, \mathcal{L} , and is defined as

$$\mathcal{L} = F(\mathbf{u}(t), \mathbf{p}) - \sum \lambda g_{eq}(\mathbf{x}, \mathbf{u}, \mathbf{p}, t) - \sum \mu g_{ineq}(\mathbf{x}, \mathbf{u}, \mathbf{p}, t), \quad (3.7)$$

where the cost function F was explained in Section 3.3.1. The Karush-Kuhn-Tucker (KKT) multipliers, λ and μ , are added to the set of optimisable parameters, and subject to additional constraints ($\lambda_i \geq 0$ and $\mu_i \geq 0$ for all i). This forms the *complementary slackness condition*. For any feasible solution, the equality constraints and active inequality constraints will give $g(\mathbf{x}) = 0$. Since the inactive inequality constraints $g(\mathbf{x}) > 0$, their respective KKT multipliers will be driven down to improve the Lagrangian until $\lambda = 0$. Therefore, minimising the Lagrangian minimises the objective function and ensures all constraints are met.

Indirect methods

Indirect methods attempt to solve the optimal control problem by finding a stationary point in the solution space that satisfies the second order condition of being an optimum. Traditionally this is achieved analytically through the calculus of variations, using Pontryagin's minimum principle (Pontryagin et al. 1962).

Pontryagin's minimum principle requires solution of the adjoint equations. The existence of an analytical solution consequently becomes highly dependent on the linearity of the adjoint equations, but assumptions and simplifications can sometimes be made in order to determine a general solution to the equations. These assumptions are usually only valid for short duration scenarios such as the missile trajectory described by Ohlmeyer and Phillips (2006) and the re-entry of the two exo-atmospheric stages of the Saturn V rocket presented by Haeussermann (1965). Given the long durations and non-linearities present in low-thrust trajectories, an analytical solution usually cannot be found.

An alternative to solving the infinite-dimensional optimal control problem is to discretise the problem and solve the resulting high- but finite-dimensional problem using indirect numerical methods. Forgoing a general

solution to the objective function, these methods break the problem down into many sub-problems, each of which may be solved locally. This is collectively known as nonlinear programming (NLP) (Betts 1998).

The general approach to nonlinear programming is to take a candidate solution, \mathbf{x}_0 . An iterative procedure is then used to improve this solution by varying the state a certain amount, α , in a certain direction, \mathbf{k} , as defined in equation (3.8). The sign of the step direction, α , determines whether the algorithm finds a minimum or a maximum,

$$\mathbf{x}_{n+1} = \mathbf{x}_n + \alpha \mathbf{k}. \quad (3.8)$$

Gauss (1827) pioneered gradient-based methods in the early 19th century, by using the Jacobian of the Lagrangian with respect to the state vector, $\nabla \mathcal{L}$, as the search direction,

$$\mathbf{x}_{n+1} = \mathbf{x}_n + \alpha \nabla \mathcal{L}(\mathbf{x}_n). \quad (3.9)$$

This technique is also known as the method of steepest descent, because the Jacobian matrix functions as a multi-dimensional gradient. When a candidate solution is found with no gradient that leads to a better solution, the candidate solution must be a local optimum.

Pure gradient methods are prone to slow optimisation, particularly with stiff problems. A second-order variant on this scheme is often referred to as *Newton's method* because it uses the iterative root-finding scheme devised by Newton (1711, 1736) to determine the zeroes of the gradient. Since the gradient is itself a derivative of the Lagrangian, this technique requires computation of a second derivative,

$$\mathbf{x}_{n+1} = \mathbf{x}_n + \alpha \frac{\nabla \mathcal{L}(\mathbf{x}_n)}{\nabla^2 \mathcal{L}(\mathbf{x}_n)}. \quad (3.10)$$

The curvature information held within the second derivative matrix (called the Hessian matrix, $\nabla^2 \mathcal{L}$) allows this technique to converge faster, but each iteration takes more computational effort.

Various schemes exist to calculate the step size, α . These algorithms, collectively called a *line search*, can often be very computationally inefficient and time consuming. When the step size, α is equal to one, gradient methods assume a linear behaviour in the vicinity of the candidate solution, and select the next iteration accordingly. Newton's method assumes a quadratic behaviour in the vicinity. Variations on Newton's method have been used to great success in many optimisation applications, not least trajectory optimisation, leading to the techniques being collectively named *sequential quadratic programming* (SQP). Quasi-Newton methods such as the Broyden-Fletcher-Goldfarb-Shanno (BFGS) method use an approximation of the Hessian to speed up computation while retaining the benefits of second-order gradient information.

In certain applications such as low thrust trajectories, the long propagation times requiring many grid points result in very large, sparse Jacobian and Hessian matrices. A sparse matrix is characterised by very few non-zero terms (Stoer and Bulirsch 2002), due to very loose coupling; changes early in the trajectory do not have a direct effect on the later stages of the trajectory except by influencing all of the intervening states. Some algorithms are able to exploit this sparsity to calculate the Hessian and Jacobian matrices very efficiently.

Direct methods

Direct methods, in contrast to indirect methods, do not try to determine additional information from the objective function. They simply evaluate the objective function at a number of points, and then adjust the search space towards the best solution found. Consequently direct methods cannot be analytical.

There are many different techniques to determine which solutions to evaluate. A number of techniques, such as tabu search and hill-climbing, merely search adjacent solutions and consequently function only as local search methods. Without using gradient information each iteration must exhaustively search the adjacent function space, so these techniques are

less efficient than indirect methods (subject to the difficulty of gradient computation). The real advantage of direct methods emerges when each iteration is allowed to search a wider space.

The largest group of direct methods is evolutionary algorithms. In general, these techniques evaluate a number of candidate states, make a few random changes and then re-evaluate the new generation, picking the best solutions to continue with. For example, genetic algorithms avoid local minima by performing random mutations and genetic crossovers, emulating the biological process of evolution. Another example called simulated annealing was introduced by Kirkpatrick et al. (1983), and emulates a blacksmithing technique where the metal is cooled slowly to allow the particles to align into an optimised (crystallised) low energy state.

Evolutionary algorithms are heavily dependent on their implementation, and the efficiency of their mutations, to steer the evolution of the solution. Furthermore, with delicate problems such as *Lunar Mission BW-1*, random mutations frequently lead to invalid solutions (the spacecraft does not reach the target orbit) and consequently these techniques can struggle to find alternative feasible solutions, as changes may be required to multiple parameters before another basin of convergence is found.

Another group of direct methods is called dynamic programming. These techniques are particularly used in financial programming and management science, with the aim of finding the path of least cost in a discrete system by evaluating each step backwards from the goal using the recursive Bellman equations (Bellman 1957). As such dynamic programming is best suited to heavily discretised states and paths between states, and consequently a very limited number of controls. Dynamic programming has been expanded to solve continuous time problems using the Hamilton-Jacobi-Bellman equations, but this adaptation requires calculation of the cost function gradient, converting the technique to an indirect method (Bellman 1957).

In general, direct methods are more robust, and tolerate stiffness and caverns in the solution space better than indirect methods. They are often described as a better global search, which is not necessarily true. Unlike

indirect methods, they can find alternative basins of convergence, but essentially rely on guided guesses to find these basins. With large, complex problems, the probability of finding the correct basin diminishes. While various metaheuristics, many of which are described in Dréo et al. (2006), have different degrees of success in finding basins of convergence, as the size and complexity of the problem scales up they all must approach a brute force search before they can be certain of finding the global optimum.

3.3.4 Survey of commercial optimisation algorithms

There have been many implementations of the optimisation methods described above. Examples of direct methods include the collocation method OTIS (Optimal Trajectories by Implicit Simulation, Hargraves and Paris 1987), and the single shooting control parameterised method POST (Program to Optimize Simulated Trajectories, Brauer et al. 1977), both developed by US industry. These codes are both in widespread use at NASA and at various US government laboratories and universities, but are not generally available to other organisations. TOMP (Trajectory Optimization by Mathematical Programming, Kraft 1994) is very similar to POST. MUSCOD (Multiple Shooting Code for optimization, Bock and Plitt 1984), developed at the University of Heidelberg, combines control parameterisation with multiple shooting.

The sequential gradient restoration algorithm (SGRA, Miele 1975) is an indirect method as are the codes ASTROP developed by Bartholomew-Biggs et al. (1988) and BNDSCO by Bulirsch (1971). ASTROP has been used at the European Space Operations Centre (ESOC) extensively for exo-atmospheric trajectory optimization.

These methods are mostly superseded by newer methods with additional features, and so were not selected for inclusion in GESOP. Instead, TROPIC (Trajectory Optimisation by Direct Collocation) and PROMIS (Parameterised Trajectory Optimisation by Direct Multiple Shooting) are two transcription algorithms developed at DLR (Jänsch and Paus 1990). CAMTOS (Collocation And Multiple Shooting Trajectory Optimisation

Software) was developed internally by ASTOS Solutions GmbH. Each of these algorithms transcribes the optimal control problem into smaller NLPs.

Two SQP methods are then available within GESOP to solve the subproblems. SLLSQP is a fairly generic SQP solver, and computes local optima in order n^3 time, where n is the number of optimisable parameters. Consequently it is useful for scenarios with up to about 100 parameters. SNOPT (Sparse Nonlinear Optimizer, Gill et al. 1997) was developed at Stanford University and is a widely used BFGS implementation with a dense quasi-Newton Hessian approximation. It improves upon SLLSQP with a few modifications that exploit sparsity within the Jacobian matrix (by treating non-linear parameters as linear within a constrained region) thus allowing it to compute local optima in order n^2 time. However it cannot exploit sparsity of the Hessian matrix, and consequently is ill suited for large sparse optimisations such as low-thrust trajectories (Betts and Gablonsky 2002). SNOPT is useful for problems of about 1000 parameters (Fischer et al. 2008).

For larger problems, ASTOS Solutions GmbH has licensed SOCS (Sparse Optimal Control Software, Betts and Huffman 2002). SOCS is a combined transcription and SQP algorithm developed by The Boeing Company. Its direct collocation method further exploits sparsity, resulting in a computational time that increases with order n . SOCS has documented solutions for problems with over 500,000 parameters. The subroutine within SOCS that solves the nonlinear problems is another BFGS implementation, called HDSNLP, using a Schur-complement developed by Gill et al. (1987) to solve the SQP. The Jacobian and Hessian matrices are computed efficiently using sparse finite differencing as proposed by Curtis et al. (1974) and Coleman and Moré (1983).

CGA (Constrained Genetic Algorithm, Fischer et al. 2008) is an early implementation of a genetic algorithm developed by ASTOS Solutions GmbH, currently limited to integer parameters. It gives a better global search than the other implemented methods (all gradient based methods) but is not very computationally efficient, and has been empirically shown

to be ineffective for more than about 20 parameters in its current form.

3.4 Application of optimisation methods to low thrust problems

Traditional high-thrust chemical rocket trajectories do not need optimisation for lunar missions, since the duration is sufficiently small that perturbing forces are negligible. In the resulting restricted three-body scenario (the Earth and Moon are defined as static, with a spacecraft of negligible mass orbiting them) there are simple analytical solutions for the trajectory (Euler 1911).

As outlined in Chapter 2 the task of optimising a low-thrust trajectory is somewhat more complex due to the long duration of forces acting on the spacecraft requiring lengthy integrations. Section 3.3 provided an explanation of optimisation methods, and Section 3.3.4 introduced a number of implementations of these methods used in industry. This section will address how effective previous studies have found these methods to be, and how applicable they are to *Lunar Mission BW-1*.

Firstly there are a number of existing literature reviews compiled by other authors. Betts (1998) provides a generalised explanation of the different optimisation algorithms, without addressing any particular scenarios. McKay et al. (2011) provide a survey of non-Keplerian orbits, which they define as any orbit with forces additional to the primary point-mass gravitational force. Literature is included in their survey covering a broad spectrum of trajectory planning and optimisation from optimal control and sequential quadratic programming to genetic algorithms. Their study was focussed towards using low thrust propulsion to maintain a stable orbit in the presence of these secondary forces, and while *Lunar Mission BW-1* requires a transfer trajectory rather than a stable orbit their paper does conclude that there are some serious deficiencies with established research in the area:

“It is clear, however, that work still has to be done to trans-

form the steadily growing body of literature on highly-non-Keplerian orbits from interesting theory into actual, practical missions” (McKay et al. 2011, p.663).

Their survey did not include analysis of any actual missions, but rather compared existing theoretical studies. For the purposes of this literature review, the following, more extensive review of literature will be divided into indirect optimal control and gradient projection methods, direct non-linear programming techniques, and other direct numerical techniques, as defined in Section 3.3.3.

Optimal control and gradient projection methods

Chemical rocket trajectories do not generally need optimisation for lunar missions. Interplanetary missions are a different matter entirely, because gravitational assists can lead to a very complex solution space. The traditional approach is to patch simplified two-body segments together. Consequently, this technique was widely used to apply optimal control theory to low-thrust trajectory optimisation, such as that performed by Stuhlinger (1964). However, many technological hurdles emerged restricting the uptake of electrical propulsion systems on spacecraft, so interest in the topic waned.

Most of these hurdles had been overcome by the early 1990s. Golan and Breakwell (1994) returned to trajectory planning by optimal control for low-thrust spacecraft, starting from an analytical solution developed by Breakwell and Rauch (1966). Golan and Breakwell expanded on the previous work by patching two optimally-controlled spirals together in an Earth-Moon fixed frame, albeit assuming a specific thrust of $9.81 \times 10^{-3} \text{ ms}^{-2}$, over 200 times more thrust per kilogram than *Lunar Mission BW-1* will have. While their trajectory analysis does allow for a variable thrust engine, it does not consider practical issues such as coasting phases to recharge the batteries, or transits through the Earth’s shadow. The larger thrust allows a much shorter transfer time than anticipated for *Lunar Mission BW-1*, so weaker perturbations such as the Earth’s oblateness and the

gravitational pull of the Sun and Jupiter were neglected.

Guelman (1995) performed a similar optimal control based trajectory analysis within a three-body plane. An interesting difference to Golan and Breakwell's approach is that Guelman centred his coordinate system at the Earth-Moon barycentre. This smoothes the equations of motion in the region where the Earth and Moon have comparable influence on the spacecraft; however, since a lunar transfer generally spends very little time in this region, it is usually preferable to model with the conceptually easier Earth- and lunar-centred frames. Guelman still uses a very simplified gravitational model, with a continuously thrusting spacecraft. Variable thrust is allowed for by minimising the total thrust required to achieve a lunar orbit/impact given a constant thrust duration. This approach achieved lower magnitude thrust profiles than Golan and Breakwell at the expense of mission duration (given 1000 hours of thrust Guelman found a maximum of $4.3 \times 10^{-3} \text{ ms}^{-2}$ was required, whereas Golan and Breakwell's spacecraft took approximately 10.8 days to reach lunar orbit, or about 260 hours). However, this technique is inappropriate in the current scenario because the mission is constrained by impulse (total thrust delivered over the flight) rather than thrust magnitude. Furthermore, calculating the gravitational field within a barycentric frame becomes increasingly complex with the number of bodies in the gravitational model, making it unsuitable for very low thrust missions which must allow for the weaker perturbations mentioned above.

Guelman et al. (2000) improved on their earlier gravitational model by time averaging the effects of gravity and thrust, ignoring the short term cyclical changes and focussing instead on the slower changes of orbital elements and thrust profile. This scenario was then solved via Pontryagin's Maximum Principle using their own SQP procedure. However, even with this simplification they ran into severe computational problems, requiring "about 100,000 evaluations of trigonometric integrands per integration node. Thus even a modest number of nodes, say 100 per trajectory, requires significant time expenditure" (Guelman et al. 2000, p. 497).

In contrast, Pierson and Kluever (1994) simplified the optimal control

problem by breaking it into three two-dimensional stages. These three stages consisted of a constant thrust Earth-escape, a cis-lunar coast, and a constant thrust lunar capture. This method was extended to a full three-dimensional problem by Kluever and Pierson (1995), Kluever and Chang (1996), Kluever and Pierson (1997). However, they all assume a continuous thrust profile which is incompatible with both *Lunar Mission BW-1*'s thrust constraints, and the inherent restrictions placed on thrusting by passing through the Earth's shadow. Furthermore, the optimisation method developed in these papers is adapted from Edelbaum (1964), using curve fitting to develop an approximate solution with much less computational effort than the analytical methods utilised previously. Sequential quadratic programming is then used to solve the curve-fitted problem. The starting conditions used by Pierson and Kluever (1994) of 100,000 kg with 2942 N of electric propulsion pose a confusingly ambitious scenario, given the magnitude of thrust available from current electric propulsion systems and the expectation of sending a mass similar to that of the International Space Station to the Moon. Worthy of note, however, is their utilisation of backwards propagation to assist with achieving lunar capture. To ensure strong capture, their optimisation minimised orbital energy with respect to the Moon over a fixed time. Within their two-dimensional model, they investigated the difference between targeting posigrade and retrograde about the Moon, and found a slight advantage in the posigrade orbit (final LLO mass of 93,092 kg compared with 93,032 kg for retrograde) due to the residual horizontal velocity in the S-shaped posigrade transfer compared to the 3-shaped retrograde transfer. Both scenarios improved on their respective initial guesses by less than 10 kg (about 0.1%) suggesting that either the optimisation method employed was not particularly effective, or the problem was particularly smooth and very little improvement could be made. Given the gains achieved in other similar studies, the former conclusion seems more probable.

The papers of Kluever and Pierson (1995) and Kluever and Chang (1996) adapt Pierson and Kluever (1994)'s solution technique into a hybrid approach. First a numerical procedure is presented to find an initial

guess. The trajectory under full thrust is simulated, and the phase time increased until the spacecraft gets near the lunar sphere of influence (SOI, defined in Section 4.4). The simulation is extended with no thrust to observe the lunar fly-by, and the initial angle is adjusted (in a 2D moon-fixed frame) until the coasting trajectory enters the lunar SOI with a negative radial velocity relative to the Moon. The process is then repeated in reverse for the lunar descent, and the problem then reduces to making the two trajectories meet in the middle. This two dimensional solution technique assumes that the initial orbit of the spacecraft about the Earth is coplanar with the Moon’s orbit. Many other simplifications are made, such as neglecting forces external to the Earth-Moon system. These simplifications were required so that the inverse costate equations could be found allowing Pontryagin’s principle to be exploited, giving a very accurate initial guess for the thrust profiles in ascent and descent phases. SQP was then used to blend the phases together. All of these papers assume the (very large) spacecraft can deliver constant thrust due to constant mass flow as propellant is expelled, without any possibility of variable thrust control. They do not address initial launch conditions such as inclination, not to mention the feasibility of launching such a mass in the first place.

Kluever and Pierson (1997) extended the work to three dimensions, and even targeted a polar lunar orbit. The transfer still starts from very high earth orbit, and still implements a thrust-to-weight ratio of $1.3 \times 10^{-4} \text{ ms}^{-2}$, much higher than *Lunar Mission BW-1* will have available. Pontryagin necessary conditions were used to parameterise the intial guess control profile, but the problem was then solved entirely using direct optimisation. Their initial guess was based on the 2D optimisations for a GEO-HLO transfer, with the plane change occuring during the HLO-LLO descent phase. During optimisation the plane change was slowly adjusted from the HLO-LLO phase until it was almost entirely included in GEO-HLO phase, demonstrating the efficiency of trajectory targeting maneouvres in cis-lunar space.

Nonlinear programming and sequential quadratic programming methods

Enright and Conway (1992) parameterised the state and control variables with a piecewise polynomial, thus establishing a collocation method. Extensive work was then dedicated to demonstrating that the resulting nonlinear problems approximate the optimal control problem, and that the Lagrange (KKT) multipliers are equivalent to the Pontryagin adjoint variables. A number of scenarios including an Earth-Moon transfer were then presented to verify their Hermite-Simpson direct transcription technique and Runge-Kutta parallel shooting technique. Enright and Conway concluded by identifying some shortcomings of their study, and then outlined how solving these larger problems may be accomplished.

“... it is desirable to solve lunar transfer problems for lower thrust levels, lower initial and final orbit radii, and for the noncoplanar case. The main obstacle is the size of the nonlinear programming problem that results. (Other enhancements, such as lunar eccentricity and a better Earth gravity potential, do not affect the problem size.)” (Enright and Conway 1992, p. 1001).

“First, the previous problem was solved using uniform mesh point distribution within a phase (and also the same number of mesh points for each phase). The data suggest that this is extremely inefficient, and an intelligent redistribution should be performed. Second, the NLP algorithm NPSOL is not designed to handle large sparse problems efficiently. The authors have had some success with the MINOS package that is designed for large-scale systems, and we recommend it for problems with more than 400 variables. Finally, alternate coordinate systems could be employed to possibly increase the smoothness of the solution, reducing the number of mesh points required. A variation-of-parameters approach or other strategies might be attempted.” (Enright and Conway 1992, p. 1001).

Herman and Conway (1998) use what they describe as a “very low” thrust magnitude of 10^{-4} times Earth’s gravity, g_0 . They identify that lower thrust increases the size of the problem, and consequently the difficulty. However, their entire transfer takes only 32 days, with 9 Earth orbits and 7 lunar orbits. Nonetheless, the problem is solved using collocation to transcribe the optimal control problem into non-linear subproblems. It implements constant thrust and then optimises for time, which has the same effect as optimising for fuel use. The non-linear problems are solved using a proprietary McDonnell-Douglas optimisation algorithm called NZOPT. Despite the simpler scenario, this study does establish collocation and nonlinear programming as a promising approach to solving the low-thrust trajectory optimisation problem.

Betts and Huffman (1993) investigated computationally efficient numerical techniques to determine near-optimal trajectories, by exploiting sparsity within the Jacobian and Hessian matrices. In particular, they utilised direct transcription and collocation to approximate the optimisation problem, which was then solved numerically using sparse nonlinear programming.

Betts (1994) introduced a package called Sparse Optimal Control Software (SOCS), and concluded that it is a very computationally efficient method for numerically optimising low-thrust trajectories that include nonlinearities caused by perturbing forces. This appears to be a very promising approach, but Betts (2000) acknowledges that none of his papers included tesseral harmonics of the Earth’s gravitational field, third-body gravitational perturbations from the Sun, Moon, or Jupiter, variable thruster duty cycles, the Earth’s shadow limits, or atmospheric drag at low altitudes. Betts (2000) used a polar orbit-raising transfer with a spacecraft thrusting at $1.25 \times 10^{-4} \text{ ms}^{-2}$ as a test case (this is still an order of magnitude greater thrust than *Lunar Mission BW-1*). The resulting optimisation problem had 416123 variables and 249674 constraints.

The direct transcription approach of Betts and Huffman (1993) was extended by Erb (2002) and then Betts and Erb (2003), by optimising a lunar transfer from GTO employing solar electric propulsion; a mission

profile very similar to that of SMART-1. These papers verified that the direct transcription method with sparse non-linear programming is a suitable approach for low-thrust lunar missions, but once again assumed constant thrust throughout the transfer, as well as neglecting Earth shadowing and tesseral Earth harmonics. While this method may be useful for optimising *Lunar Mission BW-1*, as a numerical approach it is not guaranteed to find the optimal path. The performance is also heavily reliant on the initial guess.

“The design of an initial guess for a trajectory with a vast number of revolutions, significant inclination changes, capturing and orbital corrections is a challenging task on its own” (Betts and Erb 2003, p. 144).

Letterio (2005) described the optimisation of a low thrust transfer using an identical thrust regime to *Lunar Mission BW-1* (Letterio’s study was completed as part of the same project with Universität Stuttgart). However, his study only covers the ascent phase, from geosynchronous transfer orbit (GTO) to the outer limits of the van Allen belts, using the higher thrust arcjet. The emphasis was on increasing the radius of the orbit as quickly as possible to escape the van Allen belts. Furthermore, at these relatively low altitudes the gravitational perturbations due to the Moon’s gravity are fairly uniform. This limits the extent to which they can be exploited to optimise the trajectory of the spacecraft.

An interesting series of articles in *Acta Astronautica* (Volume 61 Issue 9) describe a competition devised by ESA to develop a benchmark test for low thrust optimisation. The inaugural competition, held in 2007, was to optimise a low-thrust interplanetary trajectory requiring an asteroid rendezvous. As the winners of the inaugural competition, Petropoulos et al. (2007) summarised their findings:

“...it seems that a rough global search, based on simple numerical schemes coupled with mission design intuitions, is a necessary precursor activity to the local optimisation, and one

which is a rich area for research” (Petropoulos et al. 2007, p. 814).

The 2007 competition was dominated by gravity assists to maximise a spacecraft’s velocity, and as such is more relevant to inter-planetary trajectories than lunar transfers. Nonetheless, several entries attempted to optimise direct transfers from Earth to the target orbit, a scenario with similarities to the planned lunar transfer of *Lunar Mission BW-1*. In particular, Dachwald and Ohndorf (2007) developed a program called Intelligent Trajectory Optimization using NeuroController Evolution (InTrance) that combines evolutionary algorithms and neural networks to search for an optimal thrust profile. Despite the apparent failure of this method in the competition, their diagnosis of the resulting trajectory demonstrates key aspects of exploiting gravitational perturbations.

Subsequent to the competition, work was continued on using evolutionary algorithms and neural networks to optimise parameterised steering strategies for interplanetary missions (Carnelli et al. 2007, Carnelli et al. 2009). Ohndorf et al. (2009) has investigated the applicability of InTrance for Earth-Moon trajectories, and concludes that the method shows promise but is not yet fully developed. Furthermore, the parameterised steering strategies implemented in InTrance successfully restrict the computational complexity of the optimisation problem, but at the cost of inherently restricting the flexibility of the optimision process.

Other methods

There are of course many alternatives to gradient based methods of optimisation. Techniques such as genetic algorithms and simulated annealing have attracted an increasing amount of interest in recent decades, as outlined by Ren et al. (2007). The primary advantage of these methods is that they provide a better global search before descending into a basin of convergence. Unfortunately there is still no way to be certain that the basin selected will have a better optimum than others, however an implicit assumption that the gradient is generally fairly uniform across the search

area (that is, the problem is not very stiff) suggests that the basin with a better objective function at the top will have a better objective function at the bottom also. The assumption of a non-stiff search area also implies that the optimal solution will be located at the bottom of the widest basin of convergence, which is additionally the most likely to be found by the search algorithm.

An interesting methodological approach to optimisation is presented by Jackson and Coverstone (2008). Rather than developing an analytic equation to optimise, or a numerical algorithm to iteratively determine a search direction, a coarse mesh of possible trajectories is plotted based on a few controlled parameters. The largest basin of convergence is then selected based on the assumption that it will be the most robust - even if the global optimum is found using another technique, the spacecraft will never be able to follow that trajectory *exactly*. If the basin of convergence is too narrow, any number of unexpected events could easily push the spacecraft onto a severely sub-optimal trajectory, potentially resulting in the spacecraft not completing its mission. Iteratively calculating trajectories over a mesh of possible launch parameters determines a near-optimal trajectory, within a very broad basin of convergence. While the test case used by Jackson and Coverstone (2008) involved continual thrust from Earth orbit to the Sun-Earth libration point L1, the methodological nature of this approach allows easy implementation of discontinuous thrust profiles for *Lunar Mission BW-1*.

Lee et al. (2005b) performed a number of interplanetary trajectory optimisations using the more commonplace direct methods of genetic algorithms and simulated annealing. He points out that evolutionary algorithms often need distributed computing environments due to the number of computations involved. Computing power is becoming cheaper, but the parameterised problems are becoming larger.

Reviewed literature such as Dachwald (2005) and Jackson and Coverstone (2008) has shown an increasing trend using these direct methods to perform a global search identifying the most promising basins of convergence. However, depending on the implementation direct methods often

have difficulty determining the local optimum within the basin. Consequently there is a large and promising body of work utilising direct methods for global search, followed by indirect gradient methods to find the local optima within those basins (Stryck and Bulirsch 1992, Kluever and Pierson 1995, Vasile and Locatelli 2009, Yam et al. 2011).

3.5 Summary of gaps in existing knowledge

There is a variety of literature on trajectory optimisation for low-thrust space vehicles, although surprisingly few reports have been written on the trajectory optimisation of missions launched over the last decade. Consequently, the majority of literature is highly theoretical, and in most cases heavily simplified.

Early research in low-thrust trajectory analysis consisted of analytical solutions to two dimensional, two-body and restricted three-body scenarios. As more complex perturbing forces were included, the non-linearity of the functions to be optimised increased dramatically. More recent papers have resorted to numerical optimisation techniques. These numerical techniques are very computationally intensive, and are not guaranteed to find an optimal solution.

Even when these studies have included perturbing forces, they have been viewed as an unfortunate side-effect of space travel. Certainly, they do complicate the mathematics of spacecraft trajectory planning. As the spacecraft thrust becomes smaller and the transfer duration increases, the influence of external perturbing forces becomes larger. With an electric propulsion system as weak as that onboard *Lunar Mission BW-1*, the perturbing force of the Moon's gravity can dominate the thrust. Consequently, it seems appropriate to search for a computationally efficient optimisation method to exploit these perturbing forces to increase the spacecraft's orbital velocity and radius.

There is a vast amount of literature on low thrust trajectory optimisation methods. Early efforts focussed on indirect optimal control theory, which was soon discretised and solved with numerical gradient techniques.

Algorithms have been improving to allow more complex higher order problems to be solved using these techniques. Meanwhile, much work has been done recently developing direct optimisation techniques. These allow more flexibility in modelling, as required by the complexity of orbital dynamics, and can tolerate stiffer problems with undulating solution spaces.

The most promise for future developments appears to come from evolutionary algorithms, but unfortunately the genetic algorithm implemented in GESOP is still quite immature. Consequently the *Lunar Mission BW-1* trajectory design proceeded using the sparse optimal control software most suitable for higher order problems. This optimal control technique required determination of an intial guess for every optimisation, calling for a thorough knowledge of orbital dynamics and the forces acting on the spacecraft throughout the transfer, and the mechanics of lunar capture.

Chapter 4

Rocket science

4.1 Orbits

A large amount of specialised terminology is used throughout this thesis. It is assumed that professionals within the space industry are already familiar with this terminology, but for the purposes of completeness a brief explanation is provided here.

Firstly, the motion of bodies in space is defined by their position relative to each other, r , and their velocity relative to each other, v . These determine their relative orbital energy, ϵ , given by

$$\epsilon = \epsilon_k + \epsilon_p \quad (4.1a)$$

$$= \frac{v^2}{2} - \frac{\mu}{r}, \quad (4.1b)$$

where μ is the gravitational parameter of the other body, and the subscripts k and p represent kinetic and potential energies, respectively.

In the absence of external forces, orbital energy must be conserved. Under this constraint, two-body orbits take the form of conic sections, a mathematical construct studied as early as 200 BC by Apollonius of Perga. The non-degenerate forms of conic sections are a circle, an ellipse, a parabola, and a hyperbola (the degenerate forms are a single point, a straight line, or two intersecting straight lines). Each of these correspond

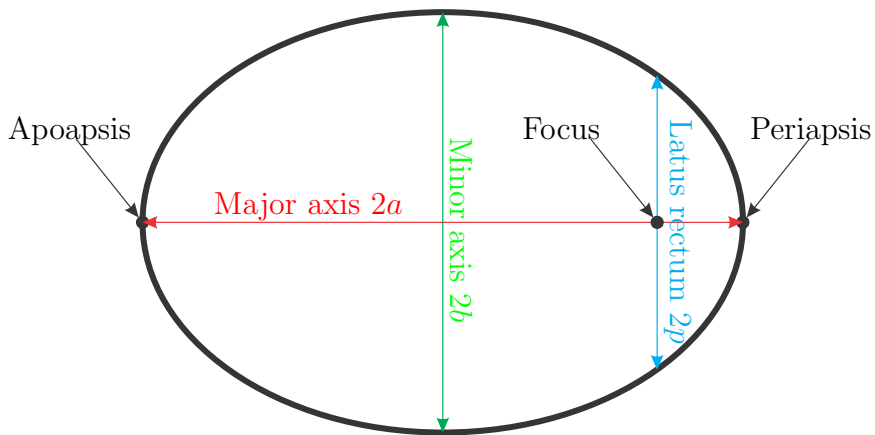


Figure 4.1: Elliptical parameters.

to a particular type of orbit.

Only two of these conic sections are important within orbital mechanics. In a frame centred on one of the bodies, a hyperbola describes the path of a second body with net positive orbital energy, and an ellipse describes the path of a second body with net negative orbital energy. A parabola is a special case where relative orbital energy is exactly zero, and a circular orbit is a special case of the ellipse.

The primary body is at a point mathematically defined by the conic section, called a focus. A number of other parameters are defined for all conic sections, but only shown for an ellipse in Figure 4.1 since ellipses are conceptually easier and the majority of *Lunar Mission BW-1*'s orbit is expected to be elliptical.

The semimajor axis, a , is half of the length of the major axis, and the semilatus rectum, p , is half of the length of the latus rectum. Finally, the *periapsis* is the point in the orbit closest to the primary body, whilst the *apoapsis* is the point furthest from the primary body.

4.2 The space environment

During the transfer from Earth to Moon, there are a number of issues to consider that may impact the durability of the spacecraft. Two of these

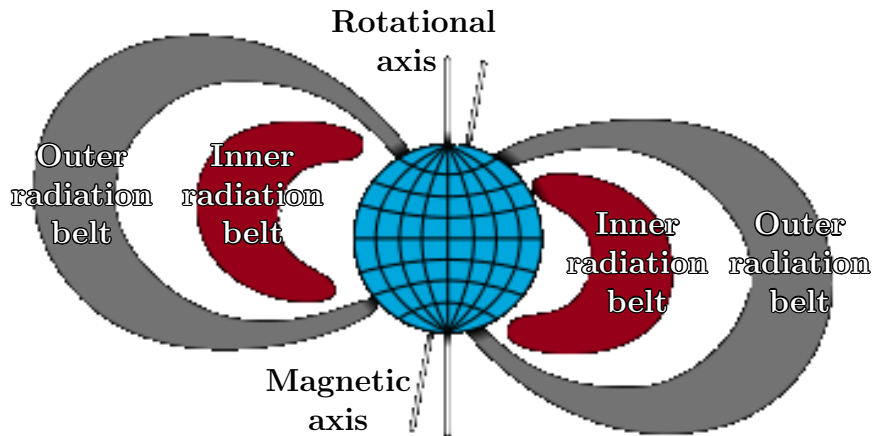


Figure 4.2: Conceptual image of the van Allen belts.

are discussed in the following sections.

4.2.1 The van Allen belts

The greatest hazard to *Lunar Mission BW-1* during the transfer is radiation. In particular, the Earth's magnetosphere traps particle radiation in two bands above the magnetic equator, as seen in the conceptual cross-section in Figure 4.2.

The outer radiation belt extends from an altitude of about three to ten Earth radii, and is characterised by a relatively high density of energetic (0.1-10 MeV) electrons and some protons. The density varies wildly based on geomagnetic storms and variations in solar wind, but an averaged distribution is shown in Figure 4.3.

Much more problematic is the inner belt which extends from an altitude of 100 km (the limit of our atmosphere) to about 10,000 km, and consists of high concentrations of energetic protons (some over 400 MeV, which can penetrate 143 mm of lead) thought to be caused by cosmic ray collisions with nuclei of the upper atmosphere (Hess 1968). The averaged distribution of higher-energy protons is shown in Figure 4.4.

While the lower energy radiation can and frequently does corrupt computer data on satellites, preventive measures can be taken such as using

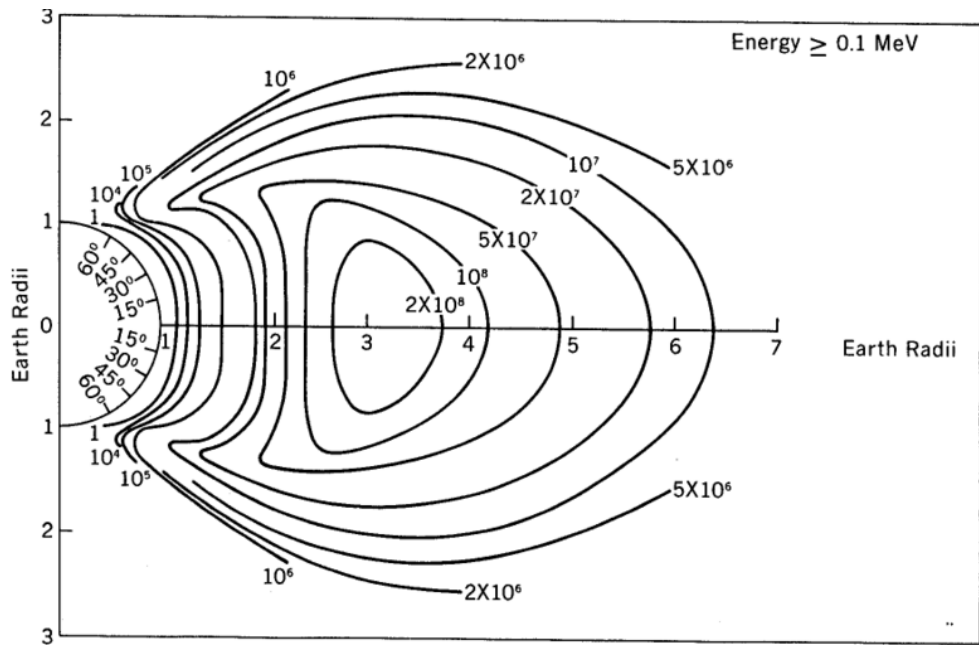


Figure 4.3: NASA's AP8MIN van Allen Belt proton flux distribution model (Sawyer and Vette 1976). Contours represent particles per square centimetre per second.

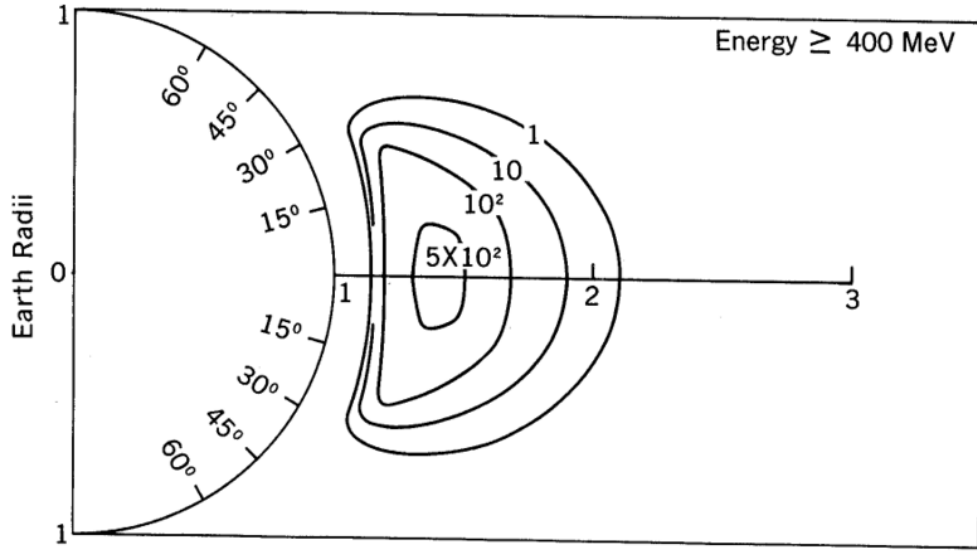


Figure 4.4: NASA's AP8MIN van Allen Belt proton flux distribution model (Sawyer and Vette 1976). Contours represent particles per square centimetre per second.

radiation hardened hardware, or shielding the processors. The higher energy radiation however damages the solar panels, reducing the amount of power they can generate. The only known solution to this problem is to spend as little time within the van Allen belts as possible. This is the reason for the higher thrust ascent phase. Similar mission architecture considerations are seen in most low-thrust missions, including SMART-1 (Racca et al. 2002).

4.2.2 Space debris

Another hazard to spaceflight is orbital debris, in the form of defunct satellites and rocket parts, as well as micrometeorites. NASA's Orbital Debris Program Office maintains a catalogue of the largest known pieces. Once a completed trajectory is known for *Lunar Mission BW-1*, it will be checked against this catalogue. If the trajectory comes within a predetermined distance of any known object, it will be recalculated with an adjusted thrust profile or departure date. However, the orbits of smaller pieces of space junk and micrometeorites are unknown, and impacts remain a risk to the mission.

4.3 Rocket performance

4.3.1 Specific Impulse

A key figure in measuring the performance of a thruster is the specific impulse, I_{sp} . As mentioned in Section 3.2, specific impulse is the momentum added by the thrusters per unit of propellant expended.

Impulse is the scalar sum of force applied over a given time,

$$I = \int_{t_0}^{t_f} |\mathbf{F}| dt. \quad (4.2a)$$

By Newton (1687)'s second law $\mathbf{F} = \frac{d\mathbf{p}}{dt}$ it is possible to derive the impulse

in terms of momentum,

$$I = \int_{t_0}^{t_f} \frac{d\mathbf{p}}{dt} dt \quad (4.2b)$$

$$= \int_{t_0}^{t_f} d\mathbf{p}, \quad (4.2c)$$

which has units of kgms^{-1} , and in the special case of collinear forces is equal to the change in momentum Δp .

By the conservation of momentum in the spacecraft's moving frame, its increase in momentum is equal and opposite to the momentum imparted to the exhaust,

$$\Delta p_{craft} - \Delta p_{exhaust} = 0 \quad (4.3a)$$

$$\Delta p_{craft} = m_{exhaust} v_{exhaust} \quad (4.3b)$$

$$I = m_{exhaust} v_{exhaust}. \quad (4.3c)$$

Therefore the specific impulse of the spacecraft should be equal to the exhaust velocity, and its units should be ms^{-1} . However, the use of imperial units meant that specific impulse was traditionally reported as momentum change per unit *weight* of propellant, so the final value is divided by standard gravity on Earth, g_0 . Consequently specific impulse is reported in seconds,

$$I_{sp} = \frac{v_{exhaust}}{g_0}. \quad (4.4)$$

4.3.2 Delta-v

Since every circular orbit has a unique orbital speed associated with it, a common measure of rocket capability is the change in velocity the rocket can provide. Mathematically, this *delta-v* is calculated as the integral of the acceleration the rocket provides, or more intuitively, the total thrust the rocket provides over time,

$$\Delta v = \int_{t_0}^{t_1} \frac{T(t)}{m(t)} dt, \quad (4.5)$$

where $T(t)$ is the instantaneous thrust magnitude, and $m(t)$ is the instantaneous mass.

Conversely, orbital transfers may be described by the typical change in velocity required. This is known as a delta-v budget. Launching to low Earth orbit (LEO) requires a change of 7.8 kms^{-1} , but typically an additional 1.5 to 2 kms^{-1} is lost to atmospheric drag and gravity losses. Ascent from LEO to low lunar orbit (LLO) requires an additional 4.1 kms^{-1} (this mission profile was used by Apollo). Thrust vectoring adds further losses depending upon the angle of thrust.

These atmospheric, gravitational, and thrust vectoring losses can be calculated with similar integrals over the flight, respectively

$$\Delta v_{drag} = \int_{t_0}^{t_1} \frac{D(t)}{m(t)} dt, \quad (4.6a)$$

$$\Delta v_{gravity} = \int_{t_0}^{t_1} g(r) \cdot \sin \gamma dt, \quad (4.6b)$$

$$\Delta v_\varepsilon = \int_{t_0}^{t_1} \frac{T(t)}{m(t)} (1 - \cos(\alpha - \varepsilon)) dt, \quad (4.6c)$$

where $D(t)$ is the instantaneous aerodynamic drag magnitude, $g(r)$ is the local gravitational acceleration r metres from the centre of the Earth, γ is the angle from the velocity vector to the local horizontal (defined in Section 5.2), α is the body axis line (above the velocity vector) and ε is the thrust vector (above the body axis line), as shown in Figure 4.5 (Tetlow 2003). Because the thrusters of *Lunar Mission BW-1* are fixed relative to the body, the thrust vector is fixed at $\varepsilon = 0^\circ$.

Little can be done within the scope of this project to reduce atmospheric drag and gravity losses, since these effects are strongest during launch. However, gravity losses are still present during orbit raising if the thrust line has any component parallel to the gravitational force; when this occurs, the thrust is fighting against gravity rather than increasing the velocity of the spacecraft (and providing orbital energy). Similarly, thrust vectoring decreases effective delta-v because the thrust is changing the direction of the spacecraft, rather than increasing its speed.

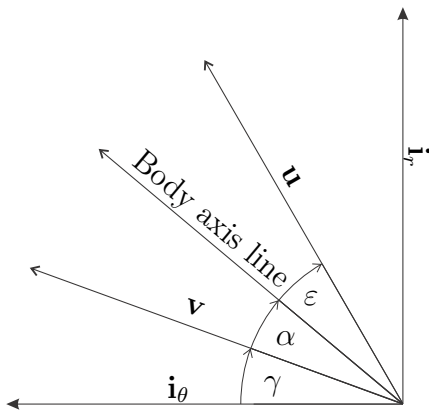


Figure 4.5: Flight angle γ , body orientation α , and thrust vector angle ϵ of the spacecraft relative to LVLH frame. \mathbf{i}_r and \mathbf{i}_θ are the local vertical and horizontal, respectively (see Section 5.2 for definition). The thrust vector is \mathbf{u} and the velocity vector is \mathbf{v} . The body axis line represents the orientation of the vehicle.

Delta-v forms a very important performance criterion. It is particularly important in tracking gravitational assists from the Moon, as velocity may be gained without expending delta-v in the form of thrust. Initial simulations at the Institut für Raumfahrtsystem determined an approximate benchmark of 3.5 kms^{-1} for *Lunar Mission BW-1* (Röser et al. 2006). This includes an estimated 1.1 kms^{-1} in phase 2 to ascend beyond the van Allen belts, 1.6 kms^{-1} in phase 3 to cruise to near EML1, 0.5 kms^{-1} in phase 4 to be captured into a lunar orbit, and 0.4 kms^{-1} in phase 5 to descend into the operating orbit.

4.3.3 Tsiolkovsky's rocket equation

A well established equation, derived in the 19th century by Konstantin Tsiolkovsky, describes the delta-v available from expending a given mass of fuel from the vehicle at a given exhaust velocity,

$$\Delta v = v_e \ln \frac{m_0}{m_1}, \quad (4.7)$$

where m_0 represents the initial wet mass of the rocket (structural mass plus fuel), m_1 represents the final mass, v_e is the exhaust velocity (Tsiolkovsky 1903, Chobotov 2002). Tsiolkovsky's rocket equation is particularly relevant to low thrust missions because it shows that the most efficient way to achieve a fixed delta-v requirement such as an Earth escape orbit or lunar transfer orbit, is to increase the propellant exhaust velocity. Missions such as *Lunar Mission BW-1* maximise their delta-v by increasing propellant exhaust velocity at the expense of other design parameters, such as thrust.

The SIMPLEX pulsed plasma thrusters developed at the Institut für Raumfahrtssysteme (Nawaz et al. 2008) provide an exhaust velocity of about 27000 ms^{-1} as stated in Table 1.1, resulting in a specific impulse of about 2750 s. Assuming a dry mass of 150 kg, 75 kg of fuel should allow for a delta-v of 10.9 kms^{-1} , far more than is theoretically required for ascent from GTO to lunar orbit.

4.4 Sphere of influence

The sphere of influence approximates the region of space in which a primary body dominates the gravitational forces on any small object such as a spacecraft. This is traditionally used to determine coasting trajectories of chemically propelled spacecraft, thus ignoring third-body gravitational forces. Due to the longer transfer times of low-thrust spacecraft it is necessary to include these additional gravitational forces across the entire trajectory, although the sphere of influence provides a convenient point to switch reference frames. The sphere of influence is defined as

$$r_{SOI} = a_s \left(\frac{m_p}{m_s} \right)^{\frac{2}{5}}, \quad (4.8)$$

where m_p and m_s are the mass of the primary and secondary bodies respectively, and a_s is the semimajor axis of the secondary body's orbit around the primary (Kemble 2006). The Earth-Moon system spheres of influence are shown in Figure 4.6. Note that the Moon's sphere of influence (with

respect to the Earth)¹ lies entirely within the Earth's (with respect to the Sun)².

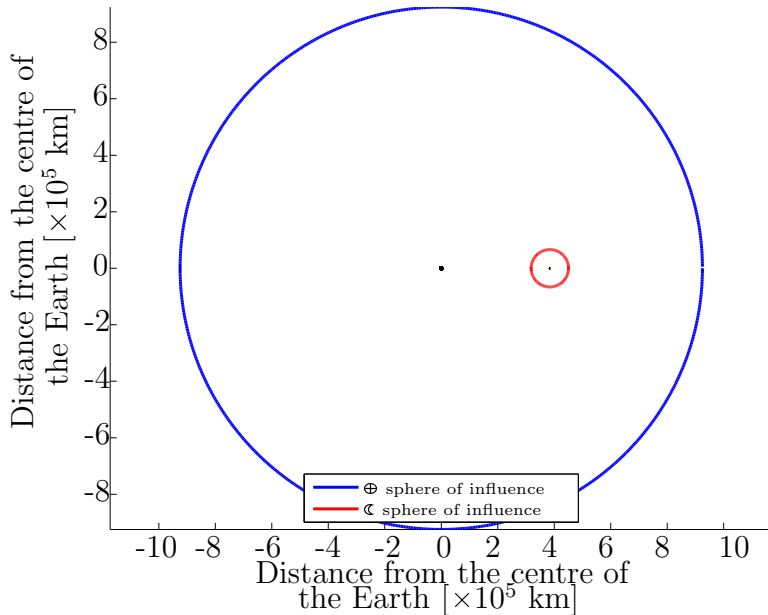


Figure 4.6: *Earth and Moon spheres of influence.*

4.5 Summary

A number of important phenomena related to the lunar trajectory were presented in this chapter. First, terminology related to elliptical and hyperbolic orbits was introduced for later sections. Then hazards to the mission were presented, notably the radiation in the van Allen belts and space debris. A number of performance measures were then outlined, before the sphere of influence was defined.

¹calculated as just over 66,000 km from the Moon's centre, just under 5/6 of the distance from the Earth to the Moon.

²calculated as almost 925,000 km from the Earth's centre.

Chapter 5

Orbital dynamics and modelling

5.1 Epoch

In any dynamic system, time is one of the most important parameters. Since the Universe is constantly changing, most of it beyond human control, any timescale needs an arbitrary starting point assigned. The current best practice is to use the epoch J2000, defined as noon, 1st January 2000, Terrestrial Time (TT). Terrestrial time is a theoretical time standard allowing for gravitational time dilation at the Earth's surface (general relativity) and the Lorentz transformation for moving bodies (special relativity); however, the Earth's rotation is also slowing down, so another transformation is needed to convert to Universal Coordinate Time (UTC) as outlined by the U.S. Naval Observatory (USNO, 2008).

Due to the discontinuous timescales traditionally used for time (seconds, minutes, hours, days and years) there are a number of measures commonly used to identify time. The Julian date (JD) is the time in days and fractions of a day (defined as 86,400 seconds) since noon, 1st January 4713BC UTC, giving the J2000 epoch a JD of 2451545.0 TT. For the optimisation, a fixed offset of 5113.5 was used, bringing the epoch up to midnight, 1st January 2014 UTC. Adding the optimisable parameter for

departure date gives the start of the trajectory. The time elapsed since this departure date (mission time) at each integration node is calculated as the trajectory is propagated forwards. Some applications required conversion to another continuous time scale called Ephemeris Time (ET). As outlined by the Navigation and Ancillary Information Facility (2010), Ephemeris Time is the number of seconds since the J2000 epoch (seconds themselves being defined by oscillations of caesium atoms).

5.2 Reference frames

In order to model a dynamic rigid body system, it is important to first define the appropriate reference frames. The International Earth Rotation Service (IERS) defined the International Celestial Reference Frame (ICRF) as a quasi-inertial frame centred on the barycentre of our solar system (Mao et al. 1998). Relativity requires that no truly inertial frames can exist, but by defining the ICRF relative to extragalactic microwave sources the angular rotation of the frame is so slow it can be assumed to be negligible for this project.

The fundamental XY plane of the ICRF coincides with the Earth's equatorial plane at Julian epoch J2000. The x -axis is defined as the intersection of the equatorial and ecliptic planes (the ecliptic plane is the plane within which the Earth orbits the Sun, as shown in Figure 5.1), with positive being towards the Earth during the March (vernal) equinox at Julian epoch J2000. Because this direction points roughly towards the constellation Aries it is often denoted Υ . This coordinate system is useful as an absolute reference within the solar system. However, since the majority of *Lunar Mission BW-1*'s trajectory will be an Earth escape spiral, an Earth-centred inertial (ECI) reference frame will be used.

ECI frames remain quasi-inertial because of neglected centrifugal and Coriolis forces due to the solar system's orbit around the galactic centre. Additionally there are residual centrifugal forces within the frame as the origin (the Earth) orbits around the Sun. These forces may be compensated by including the Sun as a gravitational perturbation (as outlined in

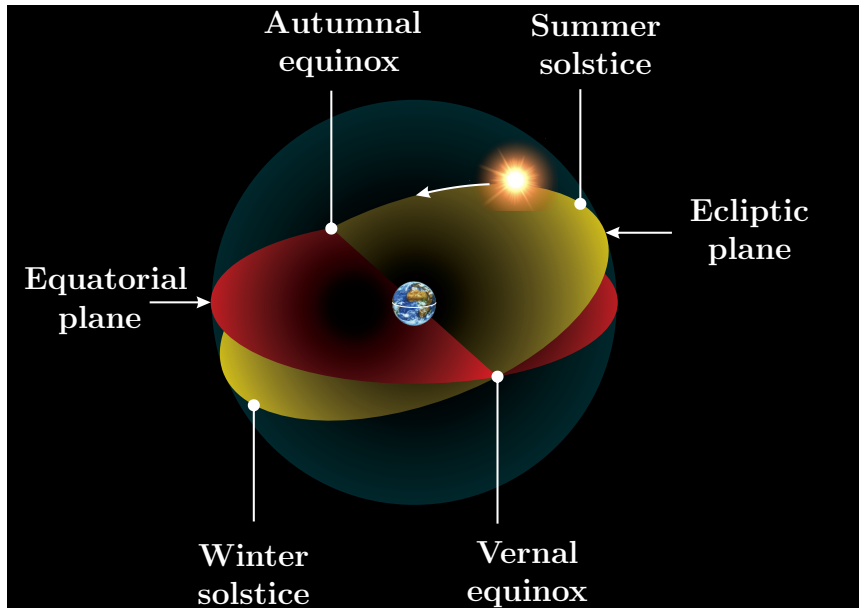


Figure 5.1: Ecliptic and equatorial planes. From an Earth-centred frame, the Sun appears to orbit the Earth. The plane of its orbit is the ecliptic plane. The solstices and equinoctia are labelled based on the northern hemisphere seasons.

Section 5.5.1).

While it is possible to translate the ICRF to be Earth-centred, the ICRF has not been universally adopted yet. In particular, the NASA SPICE libraries use an older standard, the J2000.0 frame (not to be confused with the J2000 epoch, upon which it is dependent), based on optical measurements of galactic stars called the FK5 catalogue. Due to this discrepancy in measurement, the J2000 reference frame is offset from the ICRF by a small rotation: the J2000 pole offset is about 18 milliarcseconds (mas) and the equinox offset is approximately 78 mas, increasing by about 3 mas per year (Gontier et al. 2002). For compatibility with the NASA SPICE libraries the optimisations performed in GESOP were restricted to the J2000.0 frame, so for consistency it was also used in the STK simulations described in Section 8.2.3.

Surface coverage analysis and higher order gravitational forces (discussed in Section 5.5.2) require an additional frame that rotates about

the poles (the z -axis) in time with the body's rotation, so that the surface appears stationary. This is often called a surface-fixed frame, but is sometimes given a dedicated name (for example, the lunar-centred fixed frame is often called *selenocentric*, and the Earth-fixed frame is often called *geodetic*). The IERS maintains an Earth-centred fixed (ECF) frame called the International Terrestrial Reference Frame (ITRF). The NASA SPICE libraries implement ITRF93, which allows for precession based on the 1976 IAU model by Lieske et al. (1977), nutation based on the 1980 model with IERS corrections by Herring et al. (1986), the differences between terrestrial time and atomic sidereal time, and polar motion due to changes in the Earth's moment of inertia (Montenbruck and Gill 2000).

During the later stages of *Lunar Mission BW-1* the spacecraft will be orbiting the Moon. Since most coordinate systems (discussed in Section 5.3) are designed to have the primary body at the origin, a lunar-centred inertial (LCI) frame will be used for these phases. Translation to lunar centred frames requires accurate determination of the Moon's position, addressed in Section 5.5.1. The rotation required to determine a fixed lunar frame is available in both STK and SPICE and known as the Mean Earth frame. The z -axis is defined along the primary inertial axis of the Moon, while the x -axis is defined towards the mean position of the Earth relative to the Moon (since the Moon is tidally locked to the Earth, the Earth vector traces a circle on the Moon's surface) (LRO Project and LGCWG White Paper 2008).

Finally, to model the forces acting on the spacecraft it is necessary to define a local frame. Within the ECI frame, \mathbf{r} represents the position vector of the spacecraft from the origin (defined as the centre of the primary body), as shown in Figure 5.2, while \mathbf{v} is the velocity vector of the spacecraft. Designating the position vector as the local vertical, and the tangent relative to the central body as the local horizontal, this defines a local frame known as the Gauss frame, or the Local Vertical-Local Horizontal (LVLH) frame (*STK Suite Help Files* 2011). It is important to note that the local horizontal is not necessarily parallel to the velocity, as highlighted in Figure 5.3.

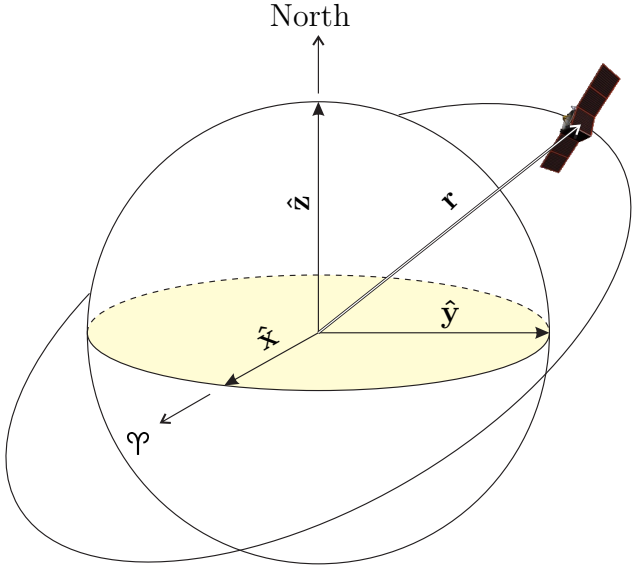


Figure 5.2: *Earth-Centred Inertial frame.* Axes \hat{x} , \hat{y} , \hat{z} represent the J2000.0 frame, where \hat{x} points towards the vernal equinox φ and \hat{z} points through the North pole of the Earth.

For compatibility with the majority of cited literature, including Keppler (2000)'s comprehensive study of various coordinate systems applicable to orbital dynamics, the following notation shall be used throughout this thesis. The radial direction (from the centre of the primary body to the orbiting spacecraft) is a unit vector based on the spacecraft's position \mathbf{r} , and is defined as

$$\hat{\mathbf{i}}_r = \frac{\mathbf{r}}{r}. \quad (5.1a)$$

The normal direction, $\hat{\mathbf{i}}_h$, is perpendicular to the orbital plane. The subscript h is used because this vector is in the direction of specific angular momentum, $\mathbf{h} = \mathbf{r} \times \mathbf{v}$. Since \mathbf{r} and \mathbf{v} are both within the orbital plane, this vector may be derived using

$$\hat{\mathbf{i}}_h = \frac{\mathbf{r} \times \mathbf{v}}{\|\mathbf{r} \times \mathbf{v}\|}. \quad (5.1b)$$

The tangential direction, $\hat{\mathbf{i}}_\theta$, is perpendicular to radial direction, but still within the orbital plane. It is important to note that this direction is

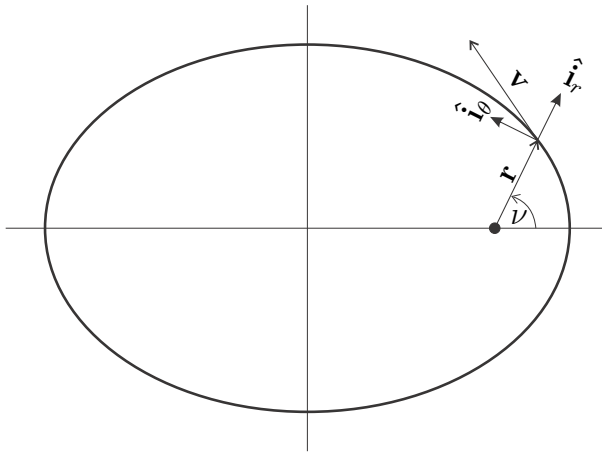


Figure 5.3: Local Gauss frame. Vector \mathbf{v} represents the spacecraft's velocity. Vector \mathbf{r} represents the spacecraft's position relative to the primary body. True anomaly ν represents the angle of this position relative to the periapsis.

not necessarily parallel to velocity, and so should be derived using

$$\hat{\mathbf{i}}_\theta = \hat{\mathbf{i}}_h \times \hat{\mathbf{i}}_r. \quad (5.1c)$$

5.3 Orbital elements

Orbital motion essentially stems from Newton (1687)'s universal law of gravitation,

$$\mathbf{F} = -m \frac{\mu}{r^2} \hat{\mathbf{i}}_r, \quad (5.2)$$

where μ represents the gravitational constant of the primary body, m represents the mass of the orbiting body and r represents the distance between the two.

Kaplan (1976) provides a thorough derivation of orbital dynamics demonstrating that in the absence of external forces this law results in elliptical motion (when escape velocity is not exceeded).

As described by Letterio (2005), Cartesian positions and velocities are not suitable elements for modelling elliptical motion because they result

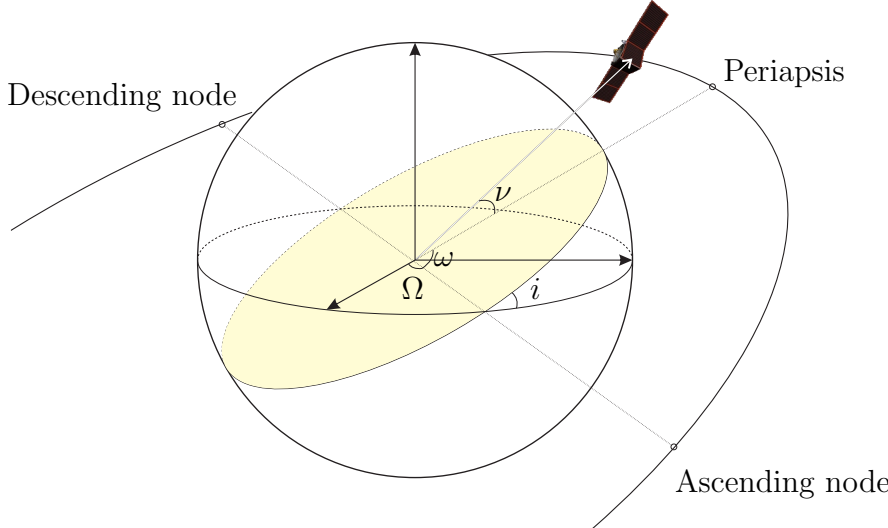


Figure 5.4: Keplerian orbital elements. Semimajor axis a and eccentricity e define the shape of the elliptical orbit. Inclination i represents the angle between the orbital plane from the equatorial plane, while right ascension of the ascending node Ω defines the axis along which the orbital plane is inclined, relative to the vernal equinox. The argument of periapsis ω defines the orientation of the orbit within this plane, by locating the periapsis relative to the ascending node.

in complex trigonometric equations for even the simple case of circular motion. Keplerian coordinates (semi-major axis a , eccentricity e , inclination i , argument of periapsis ω , longitude of the ascending node Ω and true anomaly ν) shown in Figure 5.4 describe orbits very efficiently. Unfortunately, Keplerian coordinates exhibit singularities as inclination or eccentricity approach zero, causing computational difficulties during optimisation¹.

The singularities in Keplerian elements severely limit the step size that can be used during optimisation without accumulating large errors in the calculations. Therefore the recent trend is to use equinoctial elements for

¹Division by a parameter close to zero creates a *fast variable*, where even small changes in one parameter can result in large changes to another. This requires very small step sizes when using numerical integration, hence increasing the number of computations required. Furthermore, when e is equal to zero, ω is undefined (a circular orbit does not have a periapsis) and when the i is equal to zero, Ω is undefined (an equatorial orbit does not have an ascending node).

optimising orbital trajectories. A review of orbital element sets by Hintz (2008) came to the same conclusion as Letterio and Keppler: the elements resulting in the smoothest trajectories are the *modified equinoctial element set* proposed by Walker et al. (1985),

$$p = a(1 - e^2), \quad (5.3a)$$

$$f = e \cos(\omega + \Omega), \quad (5.3b)$$

$$g = e \sin(\omega + \Omega), \quad (5.3c)$$

$$h = \tan \frac{i}{2} \cos \Omega, \quad (5.3d)$$

$$k = \tan \frac{i}{2} \sin \Omega, \quad (5.3e)$$

$$L = \omega + \Omega + \nu, \quad (5.3f)$$

where p represents the semi-latus rectum, as explained in Section 4.1, L represents the true longitude and f , g , h and k are convenient non-singular transformations of the Keplerian elements, with no physical meaning.

The lack of physical meaning in equinoctial elements has hindered their uptake. Many published studies still use Keplerian or even Cartesian coordinates, and many widely used textbooks do not even mention the modified equinoctial element set. For example Chobotov (2002, p. 194) outlines the original set of equinoctial elements proposed by Broucke and Cefola (1972), but neglects the modified set.

5.4 Orbital equations of motion

Differentiating equations (5.3) defining the modified equinoctial elements and then substituting through by those same equations to remove the Keplerian terms, gives the Gaussian equations of motion as presented by Walker et al. (1985), Walker (1986), Keppler (2000), Erb (2002), Letterio

(2005), Hintz (2008)²,

$$\dot{p} = \sqrt{\frac{p}{\mu}} \frac{2p}{w} \Delta_\theta, \quad (5.4a)$$

$$\dot{f} = \sqrt{\frac{p}{\mu}} \left(\Delta_r \sin L + \frac{(w+1) \cos L + f}{w} \Delta_\theta - \frac{g(h \sin L - k \cos L)}{w} \Delta_h \right), \quad (5.4b)$$

$$\dot{g} = \sqrt{\frac{p}{\mu}} \left(-\Delta_r \cos L + \frac{(w+1) \sin L + g}{w} \Delta_\theta + \frac{f(h \sin L - k \cos L)}{w} \Delta_h \right), \quad (5.4c)$$

$$\dot{h} = \sqrt{\frac{p}{\mu}} \frac{s^2 \cos L}{2w} \Delta_h, \quad (5.4d)$$

$$\dot{k} = \sqrt{\frac{p}{\mu}} \frac{s^2 \sin L}{2w} \Delta_h, \quad (5.4e)$$

$$\dot{L} = \sqrt{\frac{p}{\mu}} \left(\frac{h \sin L - k \cos L}{w} \Delta_h \right) + \sqrt{\mu p} \left(\frac{w}{p} \right)^2, \quad (5.4f)$$

which have been simplified (and made more computationally efficient) using the terms

$$w = 1 + f \cos L + g \sin L, \quad (5.4g)$$

$$s^2 = 1 + h^2 + k^2, \quad (5.4h)$$

where μ represents the gravitational constant of the primary body ($398600.4418 \times 10^9 \text{ m}^3 \text{s}^{-2}$ for the Earth as per National Imagery and Mapping Agency 2000 and $4902.7989 \times 10^9 \text{ m}^3 \text{s}^{-2}$ for the Moon as per Zhang 1994). The perturbations Δ_r , Δ_θ and Δ_h represent the total acceleration due to forces other than the primary body's classical gravity, split into vector components using the LVLH frame outlined in Section 5.2. Note that Δ_θ is not necessarily parallel to the velocity vector. Also note that in the absence of perturbations, the only time-varying element is L , the true longitude. This is because the other elements specify an orbit, whereas the true longitude represents the position of the orbiting body within that orbit. In the absence of perturbing forces the orbit remains constant.

²Note the equation for \dot{g} was corrected in Walker (1986). This correction is sometimes missed in later publications, such as Hintz (2008).

5.5 Perturbations

The total perturbing force [Δ_r Δ_θ Δ_h] outlined in Section 5.4 is resolved from the influence of third bodies Δ_q , the oblateness of the primary body Δ_g , the solar wind Δ_\odot , and the applied thrust of the spacecraft Δ_T . Erb (2002) states that,

“The acceleration Δ_q can, depending upon the overall situation, either be something to take advantage of, or something that needs to be compensated [for]” (Erb 2002, p. 8).

This sentence summarises one of the key objectives of this study: to plan the spacecraft’s trajectory such that the gravitational assists Δ_q increase the velocity of the spacecraft relative to the Earth as much as possible, thereby reducing the thrust requirements on the propulsion system.

5.5.1 Third-body perturbations

Reviewed literature unanimously agrees that the most accurate model available for relative positions of bodies within the solar system is the NASA JPL Planetary and Lunar Ephemerides. This data is accessible from Jet Propulsion Laboratory (2004), in the form of Cartesian coordinates for celestial bodies at any given Julian Date. Many prior studies have used the JPL DE-405 Ephemeris, but for this project the JPL Ephemeris DE-421 were implemented through the NASA SPICE libraries. As explained in their supporting documentation, “While the lunar orbit in DE 421 is close to that in DE 418, it is a major improvement over the widely distributed DE 405 (Standish 1998). For DE 405 the lunar orbit was not fit in a way consistent with the other planets” (Folkner et al. 2008, p. 1).

To calculate the distance between the respective bodies, it is necessary to translate the spacecraft’s position into Cartesian coordinates. Betts (1994) derives the following set of equations for this purpose, although more recent literature often makes typographical mistakes when reproducing them, particularly with regard to the signs of some terms (for example

Keppeler 2000, Erb 2002, Letterio 2005),

$$r_x = \frac{r}{s^2} (\cos(L) + \alpha^2 \cos(L) + 2hk \sin(L)), \quad (5.5a)$$

$$r_y = \frac{r}{s^2} (\sin(L) - \alpha^2 \sin(L) + 2hk \cos(L)), \quad (5.5b)$$

$$r_z = \frac{2r}{s^2} (h \sin(L) - k \cos(L)), \quad (5.5c)$$

$$v_x = -\frac{1}{s^2} \sqrt{\frac{\mu}{p}} (\sin(L) + \alpha^2 \sin(L) - 2hk \cos(L) + g - 2fhk + \alpha^2 g), \quad (5.5d)$$

$$v_y = -\frac{1}{s^2} \sqrt{\frac{\mu}{p}} (-\cos(L) + \alpha^2 \cos(L) + 2hk \sin(L) - f + 2ghk + \alpha^2 f), \quad (5.5e)$$

$$v_z = \frac{2}{s^2} \sqrt{\frac{\mu}{p}} (h \cos(L) + k \sin(L) + fh + gk), \quad (5.5f)$$

where $r_{x,y,z}$ and $v_{x,y,z}$ are the position and velocity respectively of the spacecraft in Cartesian axes, p, f, g, h, k and L are the modified equinoctial elements of the spacecraft as per equation (5.3), w and s^2 are the helper functions as per equations (5.4g) and (5.4h) respectively, $\alpha^2 = h^2 - k^2$ and $r = \frac{p}{w}$ are two additional helper functions, and μ once again is the gravitational constant of the primary body the spacecraft is orbiting.

Betts (1994) demonstrates that the gravitational acceleration Δ_q on a spacecraft due to n multiple bodies within a frame centred on the primary body is described by

$$\Delta_q = - \sum_{j=1}^n \mu_j \left[\frac{\mathbf{d}_j}{d_j^3} + \frac{\mathbf{s}_j}{s_j^3} \right], \quad (5.6)$$

where μ_j is the gravitational constant of the j -th body, \mathbf{d}_j is the distance of the j -th body (from the satellite), and \mathbf{s}_j is the distance of the j -th body from the primary body. This is required to remove the bias from the j -th body attracting the primary body (and thereby, the origin of our reference frame). As explained by Kaplan (1976, p. 357), “The *effective attraction* of the Moon on a unit mass near Earth is just the Moon’s attraction at the mass minus the Moon’s attraction at the Earth’s center”.

While equation (5.6) can provide the third body perturbing forces di-

rectly, Battin (1999) shows that the equation is prone to truncation error due to the potentially large difference in distances involved. Therefore an alternative algorithm is recommended,

$$F(q_k) = q_k \left[\frac{3 + 3q_k + q_k^2}{1 + (\sqrt{1 + q_k})^3} \right], \quad (5.7a)$$

where

$$q_k = \frac{\mathbf{r}^T(\mathbf{r} - 2\mathbf{s}_k)}{\mathbf{s}_k^T \mathbf{s}_k}. \quad (5.7b)$$

The acceleration vector is then resolved as

$$\Delta_{\mathbf{q}} = - \sum_{k=1}^n \frac{\mu_k}{d_k^3} (\mathbf{r} + F(q_k) \mathbf{s}_k). \quad (5.8)$$

These equations were used repeatedly in the calculation of every phase of this study, to calculate the perturbing forces due to the Moon's gravity (while in the Earth's sphere of influence), the Earth's gravity (while in the Moon's sphere of influence), and the gravity from the Sun, Jupiter, Mars, and Venus. Saturn is usually excluded even from low-thrust long duration studies such as this due to its large orbit (9-10 AU, compared to Jupiter's 5 AU) and comparatively low mass (95 Earths, compared to Jupiter's 317 Earths).

For this study, the gravity due to the Sun, Mars, Venus, and the Moon was calculated from their respective centres of mass. The total gravity from the Jupiter system was calculated from its barycentre.

5.5.2 Oblateness of primary body

The Earth is not a perfect sphere. These imperfections are most commonly approximated with spherical harmonics, which models a uniform density ellipsoid. Whilst the differences between a sphere and an ellipsoid of identical mass are only noticeable in low altitude orbits, since this is where the spacecraft trajectory is most susceptible to parameter variations it can have a substantial effect on the final state. Consequently it is important to

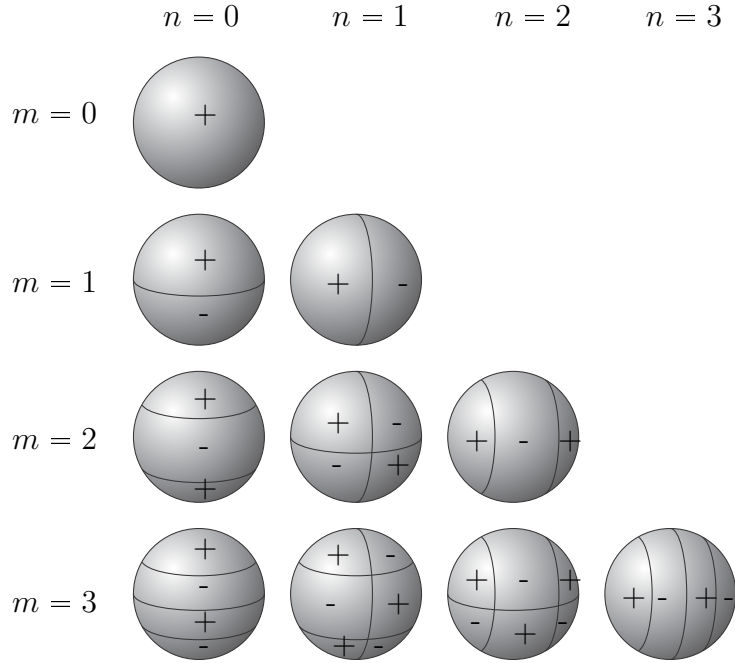


Figure 5.5: *Spherical Harmonics. The degree of the zonal harmonic is m , and the order of the sectorial harmonic is n .*

include these variations in the model. Latitudinal harmonics are known as *zonal harmonics*, longitudinal harmonics are known as *sectorial harmonics*, and any combination of the two is known as a *tesseral harmonic*. Some examples of spherical harmonics are shown in Figure 5.5.

The centrifugal force of the Earth spinning causes it to bulge outwards at the equator. This causes the equatorial radius of the Earth to be over 30 km greater than the polar radius, resulting in a significant first zonal harmonic coefficient, J_2 ($m=2, n=0$). Since the Earth's J_2 coefficient is three orders of magnitude greater than its J_3 and J_4 coefficients these higher order terms have often been neglected in simulations, such as those performed by Yang (2007).

However, modelling the central body as an ellipsoid does not allow for inconsistent density of the body's crust. The Moon in particular has very inconsistent density due to the presence of mass concentrations or *mascons*, so severe that most low lunar orbits (LLOs) will decay and impact the surface within 6 months (Zeile et al. 2010). To include variations in

density, recent satellite missions have developed very accurate models of the gravitational potential around the Earth (such as the Gravity Recovery and Climate Experiment mission, GRACE, sponsored by the Deutsches GeoForschungsZentrum 2009), and the Moon (such as NASA's Gravity Recovery and Interior Laboratory, GRAIL).

Potential energy (W) is defined in the Global Geodetic Survey (National Imagery and Mapping Agency 2000)

$$W = V + \Phi, \quad (5.9)$$

where Φ is the potential due to the body's angular momentum, when rotating at angular velocity ω about an axis r metres away, given by

$$\Phi = \frac{1}{2}\omega^2 r^2. \quad (5.10)$$

The gravitational potential function (V , units m^2s^{-2}) is defined as

$$V = \frac{\mu}{r} \left[1 + \sum_{n=2}^{n_{max}} \sum_{m=0}^n \left(\frac{a}{r} \right)^n \bar{P}_{n,m}(\sin \phi') (\bar{C}_{n,m} \cos m\lambda + \bar{S}_{n,m} \sin m\lambda) \right], \quad (5.11)$$

where μ is the body's gravitational constant (defined in Section 5.4), a is the semi-major axis of the ellipsoid body (defined by National Imagery and Mapping Agency as 6378137.0 m for the Earth). The geographic parameters of satellite radius r , longitude λ and latitude ϕ are calculated by converting the inertial frame to a surface-fixed frame, as outlined by the International Earth Rotation Service (Petit and Luzum 2010). $\bar{P}_{n,m}(\sin \phi')$ represents the series of normalised associated Legendre polynomials defined by National Imagery and Mapping Agency (2000) and reproduced in Appendix A. Parameters n and m represent the degree and order of the normalised gravitational coefficients $C_{n,m}$ and $S_{n,m}$. It is these normalised coefficients that are calculated, recorded and published.

For this study, the normalised gravitational coefficients $\bar{C}_{n,m}$ and $\bar{S}_{n,m}$ for the Earth were taken from the Joint Gravity Model 3 (JGM3, Tapley et al. 1996) due to availability of data. Several newer models have been

released such as the GRACE models mentioned earlier, but the JGM3 accuracy was sufficient for this project. For similar reasons the gravitational model of the Moon was based on data from the Lunar Prospector mission (LP165, Konopliv et al. 2001).

The perturbing force acting on the spacecraft is then determined using

$$\Delta_g = \nabla W. \quad (5.12)$$

Unfortunately the factorials and summations make this equation inappropriate for repetitive computer evaluation. A recursive algorithm developed by Montenbruck and Gill (2000) was used to simplify the calculation, while still retaining the higher order accuracy.

The impact of gravitational harmonics is obviously going to be greater at lower altitudes. The Earth harmonics, dominated by the J_2 bulge, affect mostly ω and Ω (Montenbruck and Gill 2000, Eshagh and Najafi Alamdari 2007); for example, a sun-synchronous orbit (SSO) precesses around the Earth by 360° per year, but suffers minimal inclination change. For rough analysis of results, this behaviour is approximated by

$$\dot{\Omega} = -\pi \frac{3J_2}{r_{peri}^2 \mu} \cos i, \quad (5.13a)$$

$$\dot{\omega} = \pi \frac{3J_2}{2r_{peri}^2 \mu} (5 \cos^2 i - 1), \quad (5.13b)$$

where r_{peri} is the periapsis radius.

5.5.3 Solar wind

The solar wind consists of particles emitted by the Sun, mainly ionised nuclei and electrons. Because of the charged particles in the solar wind, it does not penetrate the magnetosphere around the Earth, except at the magnetic poles. The magnetosphere starts at about 10 Earth radii from the centre of the Earth. Thus, solar wind may be neglected during the ascent phase.

The average solar power density is calculated by dividing the average

solar luminosity, L_\odot , by the surface area of a sphere centred on the Sun, $4\pi r_\odot^2$, giving approximately 1367.5 W of radiation per square metre of area near the Earth-Moon system. The momentum is subsequently determined by dividing through the speed of light, c , giving approximately 4.56×10^{-6} Ns per square metre of cross-sectional area per second, in other words, a continual force of 4.56×10^{-6} N on every square metre of area seen from the Sun. This “constant” forms the basis of Chobotov’s equation to average the acceleration of a body due to solar wind (Chobotov 2002, p. 223). Unfortunately Chobotov’s equation is intended for spacecraft in geostationary orbit. *Lunar Mission BW-1* travels much further from the Earth than GEO, and consequently requires calculation of the spacecraft’s distance from the Sun to determine average solar pressure, as given by

$$\Delta_\odot = -\frac{L_\odot}{4\pi r_\odot^2 c} \left(\frac{A_{eff}}{m} \right) (1 + \beta) \hat{\mathbf{r}}_\odot, \quad (5.14)$$

where Δ_\odot is the magnitude of the acceleration due to solar wind, in ms^{-2} , β is the optical reflection constant (+1 for total mirror reflection, 0 for total black body absorption, -1 for total transparent transmission), A_{eff} is the effective satellite projected area, and m is the total spacecraft mass. The speed of light, c , is $299792458.0 \text{ ms}^{-1}$, and the average solar luminosity, L_\odot , is $3.846 \times 10^{26} \text{ W}$.

For assumed values of 250 kg and 5.4 m^2 projected surface area, *Lunar Mission BW-1* will have an acceleration due to solar wind varying from $1.906 \times 10^{-7} \text{ ms}^{-2}$ to $2.038 \times 10^{-7} \text{ ms}^{-2}$ over the course of the year. This force is two orders of magnitude less than the maximum thrust available to *Lunar Mission BW-1*.

5.5.4 Applied thrust

The *Lunar Mission BW-1* craft has four PPT thrusters at 1.5 mN each, providing a total thrust of 6 mN. This accelerates the 200 kg craft at $3 \times 10^{-5} \text{ ms}^{-2}$. Since the direction of thrust is a design parameter (adjustable by rotating the spacecraft to point the thruster in the desired direction) a

unit vector providing this direction is defined as

$$\hat{\mathbf{u}} = \begin{bmatrix} u_r \\ u_\theta \\ u_h \end{bmatrix}, \quad (5.15)$$

such that the thrust vector is given by

$$\Delta_{\mathbf{T}} = \frac{T}{m} \hat{\mathbf{u}}, \quad (5.16)$$

where T is the instantaneous thrust, and m is the instantaneous craft wet mass.

In an elliptical orbit, thrust (approximately) tangential to orbital radius is the most efficient way to increase orbital speed and therefore push the spacecraft into a higher orbit. This has the unfortunate side effect of continually increasing the orbital period, and consequently decreasing the rotation rate required to steer the thrust vector (the spacecraft must rotate once per orbit to thrust in a constant direction relative to the Earth). This will need to be compensated for with the attitude control system.

5.5.5 Total perturbing forces

Since these perturbing forces vary over the course of the trajectory, and are often quite computationally intensive to calculate, a plot of them all clearly demonstrates which forces need be included in the optimisation. Since many of these forces vary with a cyclical nature depending on the orbits of the satellite, the Moon and other bodies, the plot in Figure 5.6 shows the upper limit of these forces. Jupiter's gravitational pull is almost negligible compared with the spacecraft's thrust, and the acceleration due to the Earth's J_2 spherical harmonic (representative of the total force due to Earth oblateness) is only significant for the first 10^8 metres.

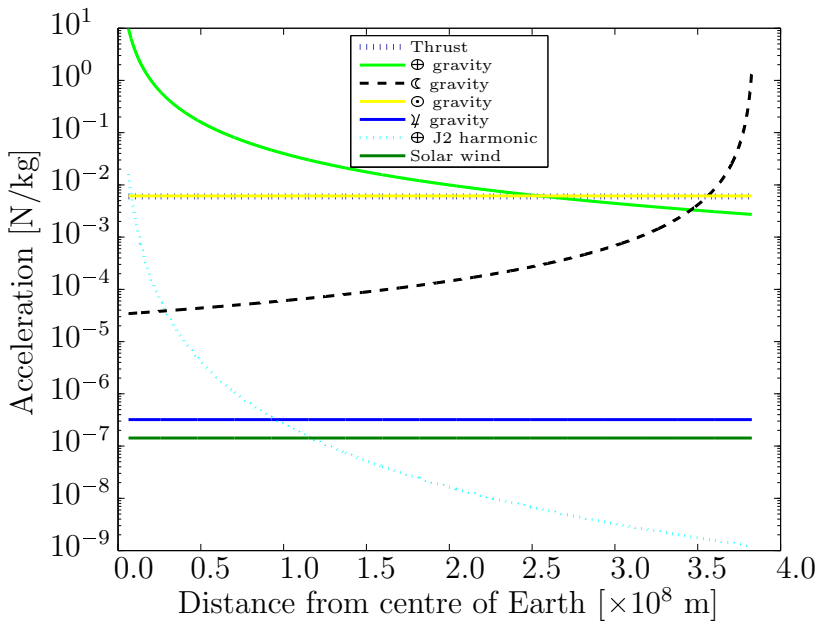


Figure 5.6: Upper limit on perturbing forces in the region between the Earth and the Moon.

5.6 Summary of orbital dynamics

Designing and optimising a low-thrust space trajectory requires a carefully selected, high fidelity model. To this end, reference times or *epochs* were defined, followed by Earth-centred, Moon-centred and spacecraft-centred reference frames. The infrequently used *equinoctial elements* were reproduced from literature as the best available representation of a slowly-changing orbit. The equations of motion derived from these equinoctial elements include a term for perturbing forces, such as 3rd body gravitational forces, gravitational oblateness of the Earth and the Moon, the force acting on the spacecraft due to solar wind, and the applied thrust.

Chapter 6

Optimisation

6.1 Introduction

This chapter describes how the mathematical process of optimisation, described in Section 3.3, applies to *Lunar Mission BW-1*.

6.2 State vector

Since we are concerned with the state of the spacecraft, in this particular scenario the state vector \mathbf{x} represents the position, velocity and mass of the spacecraft. The osculating orbit is stored in modified equinoctial elements p , f , g , h , k and L as outlined in Section 5.3. Mass is appended to the state vector, and is reduced by thrusting the propellant (reaction mass) out the back of the spacecraft,

$$\dot{m} = -\frac{T}{v_{exhaust}}, \quad (6.1)$$

where T is the instantaneous thrust magnitude and $v_{exhaust}$ is the exhaust velocity. “Real time” is added as another (albeit independent) state to allow ephemeris calculation. Finally the energy stored in the batteries is also critical to the state of the spacecraft, and similarly to the mass, it is reduced by using the thrusters (dependent on the power level required by

the thrusters over the given phase), as defined by

$$\Delta E = \int_{t_0}^{t_f} P(t) \, dt, \quad (6.2a)$$

$$\dot{E} = P(t), \quad (6.2b)$$

where $P(t)$ is the instantaneous net power consumption (or generation). Unlike the mass, the energy level may be increased, as the solar panels may cause $P(t)$ to become positive.

Consequently, the differential equation (3.3) becomes the equations of motion described in Section 5.4, appended with equations (6.1) and (6.2b). However, these differential equations assume time as the independent parameter.

6.3 Independent parameter

Traditionally the independent parameter in trajectory optimisation is time. However, due to the high velocity of the space vehicle near periapsis, time is not the best independent parameter because very few gridpoints would occur in this important area - ideally, gridpoints would concentrate near periapsis. The easiest alternative to equal-time steps is to model is equiangular steps, a technique previously used by Betts and Erb (2003).

Equiangular stepping is implemented by using the true longitude (angle of the spacecraft relative to its starting position) as the independent parameter. However, using the longitude as the independent parameter causes a large discontinuity at the transition from the Earth-centred to the lunar-centred frame, so a normalised phase longitude is defined by

$$Ln(t) = \frac{L(t) - L(t_0)}{\Delta L} + \Phi, \quad (6.3)$$

where $L(t_0)$ is the (constant but optimisable) starting position for the given phase, ΔL is the (constant but optimisable) phase length, and Φ is the phase number.

6.3.1 Substitution of parameters

Given the state vector of $\mathbf{x} = \{p, f, g, h, k, L, m, t, E\}$, the time-domain differential equations (5.4) must be modified to allow the normalised true anomaly, Ln , as the independent parameter. Therefore a substitution of parameters is required to give derivatives with respect to Ln , $\frac{d}{dLn}$. Differentiating equation (6.3) gives

$$\frac{dLn}{dt} = \frac{1}{\Delta L} \frac{dL}{dt} \quad (6.4a)$$

$$\frac{dLn}{dt} \cdot \frac{dt}{dL} = \frac{1}{\Delta L} \quad (6.4b)$$

$$\frac{dLn}{dL} = \frac{1}{\Delta L} \quad (6.4c)$$

$$\frac{dL}{dLn} = \Delta L. \quad (6.4d)$$

Using this identity, the state differential equations with respect to normalised longitude may be determined, starting with (5.4a),

$$\frac{dp}{dLn} = \frac{dp}{dt} \cdot \frac{dt}{dLn} \quad (6.5a)$$

$$= \frac{dp}{dt} \cdot \frac{dt}{dL} \cdot \frac{dL}{dLn} \quad (6.5b)$$

$$= \frac{\dot{p}}{\dot{L}} \Delta L. \quad (6.5c)$$

The remaining differential equations (5.4), (6.1) and (6.2b) are modified

similarly, resulting in the differential equations

$$\frac{dp}{dL_n} = \frac{\dot{p}}{\dot{L}} \Delta L, \quad (6.6a)$$

$$\frac{df}{dL_n} = \frac{\dot{f}}{\dot{L}} \Delta L, \quad (6.6b)$$

$$\frac{dg}{dL_n} = \frac{\dot{g}}{\dot{L}} \Delta L, \quad (6.6c)$$

$$\frac{dh}{dL_n} = \frac{\dot{h}}{\dot{L}} \Delta L, \quad (6.6d)$$

$$\frac{dk}{dL_n} = \frac{\dot{k}}{\dot{L}} \Delta L, \quad (6.6e)$$

$$\frac{dL}{dL_n} = \Delta L, \quad (6.6f)$$

$$\frac{dm}{dL_n} = \frac{\dot{m}}{\dot{L}} \Delta L, \quad (6.6g)$$

$$\frac{dt}{dL_n} = \frac{1}{\dot{L}} \Delta L, \quad (6.6h)$$

$$\frac{dE}{dL_n} = \frac{P}{\dot{L}} \Delta L, \quad (6.6i)$$

where \dot{p} , \dot{f} , \dot{g} , \dot{h} , \dot{k} and \dot{L} are the original time-domain differential equations (5.4) provided by Walker et al. (1985).

Delta-v calculation

The universal definition for delta-v was provided in Section 4.3.2. Unfortunately this definition also depends on time-domain integration. Therefore another substitution of parameters is required, using similar arithmetic to the state vector. Starting with equation (4.5),

$$\Delta v = \int_{L_{n_i}}^{L_{n_f}} \frac{T}{m} \frac{dt}{dL_n} dL_n \quad (6.7a)$$

$$= \int_0^1 \frac{T}{m} \frac{dt}{dL} \cdot \frac{dL}{dL_n} dL_n \quad (6.7b)$$

$$= \int_0^1 \frac{T}{m} \frac{\Delta L}{\dot{L}} dL_n. \quad (6.7c)$$

6.4 Objective function

Fundamentally, any trajectory that safely gets the spacecraft from Earth orbit to lunar orbit is a candidate solution. The only further considerations are the amount of fuel it takes to get there, and the amount of time it takes. Consequently, the simplest objective function for *Lunar Mission BW-1* is the total fuel used,

$$F = -m(t_f). \quad (6.8)$$

This objective function is commonly used throughout entire low-thrust trajectory analyses in literature (for example, Ichimura and Ichikawa 2008). Many other studies instead search for Pareto-optimality, based on the economic theory by Vilfredo Pareto. Pareto-optimisation is a search for the best solution that can be found without compromising other objectives, in this case the best fuel efficiency that can be found without taking an unreasonable amount of time (Lee et al. 2005b, Coverstone-Carroll et al. 2000).

Since the dry mass of *Lunar Mission BW-1* was unknown, a starting wet mass was assumed; therefore to minimise the fuel used one must simply maximise the final mass. A time penalty was considered to discourage unreasonably long transfer times, but found to be unnecessary. Preliminary, simplified optimisations for the cruise phase used an additional term to minimise the orbital energy with respect to the Moon, ϵ_{LCI} , to encourage a stronger capture. This helped develop the initial guess, but was found to be very sensitive to the weighting factors, σ_1 and σ_2 , in the modified cost function

$$F = \sigma_1\epsilon_{LCI} - \sigma_2m(t_f). \quad (6.9)$$

6.5 Boundary value problem

As mentioned in Section 6.4, candidate states include any trajectory that safely gets the spacecraft from the given Earth orbit to the desired lunar orbit. This resolves into a two-point boundary value problem: given an initial state, parameters must be chosen to get to the final state subject to some path constraints (usually differential equations).

6.5.1 Boundary constraints

In the case of orbital trajectories, the initial and final states are orbits. For preliminary simulations, a GTO with periapsis 175 km, apoapsis 35975 km, and inclination 21.7° was used, as the approximate *Lunar Mission BW-1* parking orbit after launch via GSLV (Indian Space Research Organisation Publications and Public Relations 2007). This corresponds to Keplerian elements as shown in Table 6.1. The argument of periapsis, ω , and right ascension of the ascending node, Ω , are dependent on the launch date, which as previously stated remains unknown. For the purposes of optimisation these were initialised at 180° and 0° respectively. Optimisations were performed with other values, although these proved to have very little effect on the results. True anomaly, ν , is an arbitrary starting point within the defined orbit, and so was initialised to 0° (periapsis).

Table 6.1: Keplerian elements for the initial orbit of Lunar Mission BW-1 trajectory optimisation (start of ascent phase).

Parameter	Value
Semimajor axis, a (m)	$= 2.45 \times 10^7$
Eccentricity, e (-)	$= 0.732$
Inclination, i (rad)	$= 0.379$

Since the purpose of the ascent phase is to escape the van Allen Belts, the final boundary condition is defined as the lowest point in the orbit (the periapsis) exceeding the outer limits of the van Allen Belts. Letterio (2005) used an orbital radius of 22,668 km from the centre of the Earth

as a good estimate for this point. This termination condition forms the initial condition of the next phase, as shown in Table 6.2. A very important additional constraint is that all states must be smooth and continuous over the phase transition.

Table 6.2: Phase 2 to 3 transition constraints.

Parameter	Value
Periapsis, r_{peri} (m)	$\geq 2.2668 \times 10^7$

The original mission proposal (Röser et al. 2006) suggested that the subsequent cruise phase would terminate on reaching the sphere of influence of the Moon, as defined in Section 4.4. There are two possibilities to determine this transition: either a distance from the lunar centre, or alternately if the forward propagation is required to make no reference to the Moon the SOI can be assumed to be an equivalent distance from the Earth, in which case establishing lunar SOI requires an additional constraint that the phase difference between the Moon and the spacecraft is close to zero (lunar phase difference is primarily a function of when the transfer starts).

There are a number of different parameters that measure the proximity of the satellite from the lunar SOI. First is the basic distance of the satellite from the central body, r . However, this value exhibits large oscillations as the satellite follows an elliptical orbit. There are several orbital parameters proportional to the characteristic energy of an orbit which rise smoothly under thrust, such as radius of periapsis r_{peri} , semimajor axis a , semilatus rectum p and of course the orbital energy itself, ϵ . These parameters are usually interchangeable as they have very similar definitions, proportional to semimajor axis and/or eccentricity,

$$r_{peri} = a(1 - e), \quad (6.10)$$

$$p = a(1 - e^2), \quad (6.11)$$

$$\epsilon = -\frac{\mu}{2a}. \quad (6.12)$$

However, the eccentricity can undergo rapid changes during lunar assists. Consequently, the periapsis and semilatus rectum both reveal sudden jumps. Furthermore, the semimajor axis exhibits a discontinuity when an orbit transitions from elliptical to hyperbolic (that is, if the spacecraft achieves escape velocity). Therefore the orbital energy, ϵ , was chosen as the phase constraint, as shown on the bottom of Table 6.3.

Table 6.3: *Phase 3 to 4 transition constraints.*

Parameter	Value
Lunar distance, r_{LCI} (m)	$\leq 6.6183 \times 10^7$
Distance from Earth, r_{ECI} (m)	$\geq 31.8216 \times 10^7$
Lunar orbital energy, ϵ_{LCI} ($m^2 s^{-2}$)	≤ 0.0
Earth orbital energy, ϵ_{ECI} ($m^2 s^{-2}$)	≤ 0.0

As also defined in the mission architecture by Röser et al. (2006), the subsequent capture phase would then terminate when the spacecraft is less than 1400 km above the lunar surface, as per Table 6.4.

Table 6.4: *Phase 4 to 5 transition constraints.*

Parameter	Value
Lunar altitude, r_{LCI} (m)	$\leq 1.4 \times 10^6$

The final state is lunar orbit at an altitude of 100 km above the surface of the Moon. A polar or near-polar orbit is desired for maximum surface coverage. The corresponding orbital elements are shown in Table 6.5.

Table 6.5: *Keplerian elements for the final orbit of Lunar Mission BW-1 trajectory optimisation (end of descent phase).*

Parameter	Value
Semimajor axis, a (m)	$\leq 1.8371 \times 10^6$
Eccentricity, e (-)	≤ 0.0
Inclination, i (rad)	≤ 1.57

6.5.2 Path constraints

While the path between initial and final states is defined by the differential equations of motion outlined in Section 6.2, there are a number of additional constraints on the trajectory, both physical and operational.

Firstly, the control vector $\mathbf{u} = \{u_1, u_2, u_3\}$ must be a unit vector. This ensures that the thrust level is realistic throughout the simulation, when multiplied by the thrust magnitude T which must also be constrained to the appropriate upper limit for the phase (depending on whether the phase uses the PPTs or the arcjet), leading to the equation

$$|\mathbf{u}| = 1 \quad (6.13a)$$

$$\sqrt{u_1^2 + u_2^2 + u_3^2} = 1 \quad (6.13b)$$

To guide the optimiser towards an appropriate solution, some bounds are placed on the trajectory itself. At no point in the optimisation is the spacecraft allowed to escape Earth orbit (by ensuring that the eccentricity does not approach a parabolic escape orbit), nor is the spacecraft allowed to come within 100km of either the Earth's surface, or the Moon's surface, by enforcing

$$e_{ECI} < 1 \quad (6.14)$$

$$r_{ECI} > R_\oplus + 100\text{km} \quad (6.15)$$

$$r_{LCI} > R_\odot + 100\text{km} \quad (6.16)$$

where R_\oplus is the Earth's mean radius and R_\odot is the Moon's mean radius.

Equinoctial elements are better for this optimisation than Keplerian elements, but they are still not perfect. They do exhibit singularities as the inclination approaches 180° ; in other words, they do not model strongly retrograde orbits well. Constraining the trajectory to keep away from these orbits is not a severe limitation on this optimisation since the optimiser is highly unlikely to suggest a retrograde orbit prior to Earth departure due to the large delta-v required for inclination changes (the spacecraft starts

at 21° and aims for the lunar plane of 6° from the ecliptic, that is $15\text{--}24^\circ$ relative to Earth). Even the polar lunar orbit provides a large margin of safety. Nonetheless, the optimisation should be constrained to avoid these singularities so that

$$i < 180^\circ \quad (6.17)$$

where i is the inclination of the orbit (whether geo-centric or lunar-centric).

Upon implementation of the power generation and consumption model, the constraint that battery charge must be greater than zero had a significant affect on the ascent trajectory, particularly introducing coast phases in the ascent phase. A final intuitive but hugely important numerical constraint is that the spacecraft mass must remain positive, so the remaining path constraints are

$$E \geq 0 \quad (6.18)$$

$$m \geq 0. \quad (6.19)$$

6.6 Numerical considerations

For this project, a multiple shooting Runge-Kutta 4/5 integrator was used to propagate the trajectory from the initial state using the control profile provided in the initial guess, and then again using the optimised parameters and control profile determined by the optimiser. The SOCS algorithm used its inbuilt single shooting collocation separated Hermite-Simpson integrator (Betts 2010) to propagate the trajectory.

6.6.1 Integration error

At the start of this project, in order to verify the flight mechanics described in Chapter 5, the differential equations presented in equation (5.4) were integrated in Matlab over sufficient time to allow the spacecraft to reach the Moon. An absolute error of 10^{-6} was allowed within each orbital element (p metres, f , g , h , k and L dimensionless), and a relative error of 10^{-9} ($10^{-7}\%$). Since the longitude is continually growing (not bound

within 0 to 360) yet the useful information within this parameter (the position of the spacecraft within 0 to 360) is not increasing, relative error must be severely limited. Continual thrust allows *Lunar Mission BW-1* to achieve lunar insertion in about 100 rotations, corresponding to a longitude of 36000°. The relative error in the spacecraft’s position at a radius of 360000 km is therefore 12.96 km, which should be sufficiently small to allow lunar insertion (for initial simulation, at least). The Matlab code used for this project uses the larger of the two tolerances, so at small longitudes (the start of the simulation) absolute tolerance is dominant, minimising unnecessary computational effort.

Milani and Nobili (1987) provide a simple rule of thumb to limit error accumulation by limiting the ratio of simulation timespan to stepsize. If the error at each step is ϵ and the number of steps is N , then $N^2\epsilon$ should remain less than 1. With a relative error of 10^{-9} the number of steps should be limited to 31,500. If more timesteps are needed the relative error may be reduced further, limited only by machine accuracy (in fact, many previous simulations including Milani and Nobili appear to have assumed machine accuracy). According to IEEE standard 754, double precision floating point variables have a mantissa of 52 bits. This corresponds to a relative machine accuracy $\epsilon = 2^{-52} \approx 2.2 \times 10^{-16}$, giving an upper limit of $N = 2^{26} = 67108864$ grid points.

6.6.2 Scaling

In any optimisation the parameters should be scaled so that the optimisation algorithm is not biased towards optimising any one variable at the expense of the others. This is particularly important in low thrust trajectory optimisation using equinoctial elements because variables f , g , h and k are typically between one and minus one, while L grows continually throughout the trajectory and p as the orbital semi-latus rectum can exceed many millions of metres. Consequently, without very specifically chosen weightings in the objective function, the optimiser may (for example) adjust the higher absolute value of p rather than make a tiny

adjustment to f , although the latter change might have a much greater effect on the result.

Linear scaling is often sufficient, however if changes in a variable are very small relative to the average value of that variable then the process of linear scaling on a computer will result in loss of precision due to truncation. The affine transformation (Fischer et al. 2008) uses expected upper and lower bounds for each optimisable parameter to scale it to within 1 and -1, based on absolute upper and lower limits provided by the user for each parameter.

6.7 Summary of the optimisation problem

In this chapter *Lunar Mission BW-1* was defined and fitted to the generic structure of an optimisation problem. Phase boundaries and path constraints were defined numerically. Numerical problems inherent in long-duration optimisation problems were examined, specifically integration error and scaling. An upper limit was established for the number of grid points that can be implemented during optimisation, and an affine transformation was implemented for each optimisable parameter, state and control variable.

Chapter 7

Vehicle modelling and parameterisation

7.1 Propulsion

The biggest impact of vehicle design on the trajectory is the thruster selection. As briefly outlined in Section 1.2, the preliminary design specified a thermal arcjet and four pulsed plasma thrusters (PPTs), all of which were developed within the IRS.

A number of laboratory test results for the PPTs are reproduced in Section B.1. The test apparatus is shown in Figure 7.1. By varying the power supplied to the PPTs, different levels of thrust were achieved for a small sacrifice in I_{sp} . As can be seen in Table B.1, increasing the power supplied to the thruster increases the mass of propellant that is vapourised and then accelerated. This increases the thrust, but the greater mass is not accelerated as efficiently resulting in a lower exhaust velocity, and consequently a lower specific impulse.

The thermal arcjet, shown in Figure 7.2, underwent similar laboratory testing as the PPT, and the results are reproduced in Section B.2. There are many more variables affecting the arcjet performance, mostly not listed in Table B.2, but the biggest difference to the PPTs is that the rate at which propellant is provided to the arcjet can be varied independently of

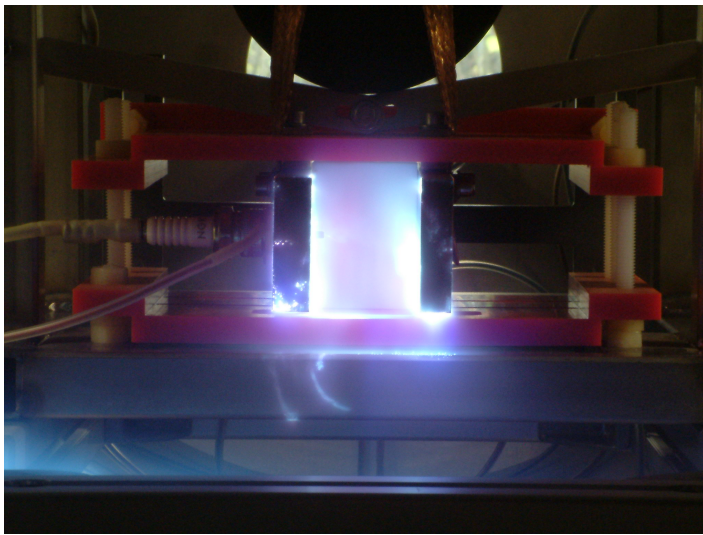


Figure 7.1: *SIMPLEX PPT during a laboratory test. The spark plug (centre left) ignites an arc between the two electrodes (pointing towards the camera) which vapourises the surface of the block of white PTFE between them. The electric field between the two electrodes then accelerates the plasma towards the camera.*

the power.

The thruster development at the time of writing this thesis is focussed on improving power efficiency. The power efficiency, η , is proportional to the thrust squared, T^2 , and inversely proportional to the mass flow, \dot{m} (Wollenhaupt et al. 2011). Since the thrust is directly proportional to mass flow, reducing mass flow will not improve power efficiency. Indeed, based on this criterion some of the arcjet tests found that the power efficiency is highest when the arc is not operated, and the thruster functions purely as a cold gas jet!

$$\eta = \frac{T^2}{2\dot{m}P} \quad (7.1a)$$

$$T = v_e \dot{m} \quad (7.1b)$$

Counter-intuitively given the above definition, during testing the power efficiency often improves at the expense of thrust. This is a cause for concern, as the low thrust of *Lunar Mission BW-1* has already required a much

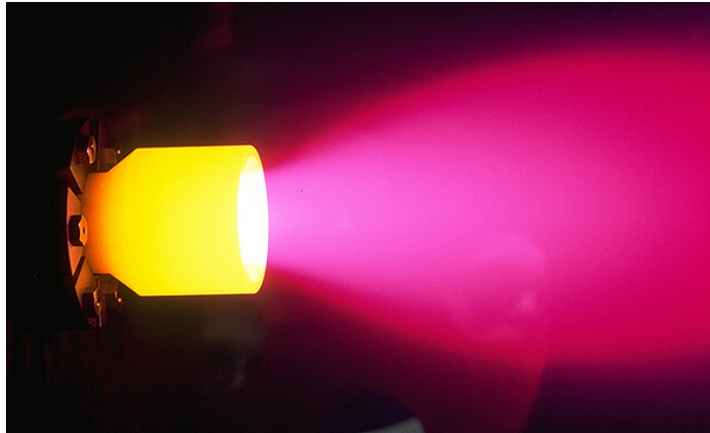


Figure 7.2: *TALOS arcjet during a laboratory test. An arc is generated between the axial cathode and the nozzle anode, which heats up the ammonia, accelerating it outwards.*

longer transfer than any used in the past, and the longer the mission the greater the chance of impact with space debris or micrometeorites, damage from radiation, or computer failure due to solar particle events (SPEs) or galactic cosmic rays (GCRs). Furthermore, during modelling for this project the length of the cruise phase frequently resulted in computational problems, so a number of design compromises were investigated to solve the problem (it is acknowledged by the author that changing hardware design to make the simulation easier is a poor design philosophy, but the project management was interested to know the effects of these changes regardless of any simulation difficulties). For example, a design configuration was being investigated with 6 PPTs rather than 4, thereby increasing the available thrust without losing I_{sp} . The trade-off with this change is the additional thrusters would increase the dry mass of the vehicle, decreasing available payload space. The same effect could be achieved by changing the pulse rate of the PPTs. A higher pulse frequency increases thrust, increases mass flow, and increases power consumption, but impulse is conserved. However, an additional unknown is introduced: the heat flux within the electrodes is increased.

Increasing the heat generated by the PPTs causes a corresponding increase in the electrodes operating temperature, until a new equilibrium is

reached with the heat radiated into space. This higher temperature can cause damage to the electrodes, structural failure in the surrounding satellite components, or even melt the propellant! There is literature indicating that some designs can tolerate higher pulse frequencies (Mueller 2000, Cabrera 2011) but the majority of documented laboratory tests use 1 Hz. Consequently, thorough lifecycle testing will be required on the thrusters to determine operational lifetime variability with pulse frequency before a four year mission such as *Lunar Mission BW-1* may be undertaken.

Nonetheless, when modelling the PPTs an additional variable was implemented representing maximum pulse frequency. Operationally, the variable thrust magnitude would be implemented by reducing the pulse frequency from the maximum available. Colleagues at IRS advised that the SIMPLEX PPT should be able to operate up to at least 3 Hz with minimal side effects (Nawaz et al. 2008).

7.1.1 Resolution of propulsion systems within modelling

The solid polytetrafluoroethylene (PTFE) propellant used by the PPTs is vapourised by a spark from a spark plug which is charged by a capacitor, so the warm-up time before operation is a single cycle. Given that a single impulse is ejected with each cycle of the PPTs, pulse-width modulation is not possible. Therefore both in the model and in practise, the PPTs are frequency modulated.

As introduced in Section 7.4.2, simulations of the cruise phase increased to about 137 grid points per orbit after automatic mesh refinement (100,000 grid points to complete 730 orbits). The orbital period within the cruise phase starts at about 14 hours and slows to almost 16 days. Consequently, the minimum resolution between grid points is about 6 minutes, much coarser than the 1 Hz resolution of the PPTs.

The arcjet allows continuous adjustment of the mass flow rate, and also continuous adjustment of the power to the electrical arc accelerating that mass. While the exact side-effects of this adjustment on the exhaust

velocity are not well known, the modelling assumption of continuously variable thrust remains valid. More importantly, this assumption is made irrelevant by the results of the optimisation procedure, which has resulted in an on-off control scenario (see Chapter 9). Starting from an orbital period of about 11 hours gives a minimum of 1.1 minutes per grid point (30,000 grid points to complete 51 orbits), which should not cause any resolution difficulties given the warm-up time observed in laboratory tests of approximately one second.

7.2 Eclipse

During the *Lunar Mission BW-1* transfer, the spacecraft may be eclipsed by the Earth or the Moon. When either of these large bodies are blocking the Sun, the spacecraft does not gain any charge from its solar panels. It is also unaffected by solar wind.

The occlusion of a luminous sphere by a smaller sphere creates a conical shadow called the *umbra*, as shown in Figure 7.3. Within the umbra a total eclipse is observed. Surrounding the umbra is an inverted cone of partial shadow called the *penumbra*. An observer within the penumbra would experience a partial eclipse. Beyond the umbra is another inverted cone of partial shadow called the *antumbra*, within which an annular eclipse would be observed (Longo and Rickman 1995).

To quantify the impact eclipsing has on the spacecraft, it is important to define key geometric parameters. First the apices and lengths of the cones may be determined using the simple geometry shown in Figure 7.4

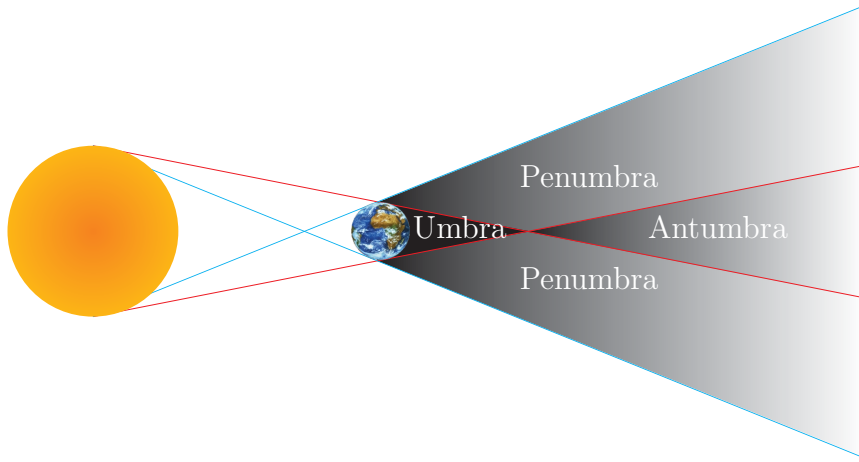


Figure 7.3: Umbra, penumbra and antumbra.

and Figure 7.5 giving the equations

$$\alpha_u = \arcsin \frac{R_\odot - R_\oplus}{r_\oplus}, \quad (7.2a)$$

$$\alpha_p = \arcsin \frac{R_\odot + R_\oplus}{r_\oplus}, \quad (7.2b)$$

$$x_u = \frac{R_\oplus r_\oplus}{R_\oplus - R_\odot}, \quad (7.2c)$$

$$x_p = \frac{R_\oplus r_\oplus}{R_\oplus + R_\odot}, \quad (7.2d)$$

where α_u is the apex angle of the umbral cone and α_p is the apex angle of the penumbral cone, x_u is the length of the umbral cone and x_p is the length of the penumbral cone, R_\odot is the radius of the Sun and R_\oplus is the radius of the Earth, and r_\oplus is the distance between the Earth and the Sun.

The spacecraft's position \mathbf{r} is then projected onto the Earth-Sun vector \mathbf{r}_\oplus giving the satellite's distance from the Earth along the Earth-Sun line x , and the satellite's distance from the Earth-Sun line y is calculated using the geometry shown in Figure 7.6, giving

$$x = \frac{\mathbf{r} \cdot \mathbf{r}_\oplus}{r_\oplus}, \quad (7.3a)$$

$$y = \sqrt{r^2 - x^2}. \quad (7.3b)$$

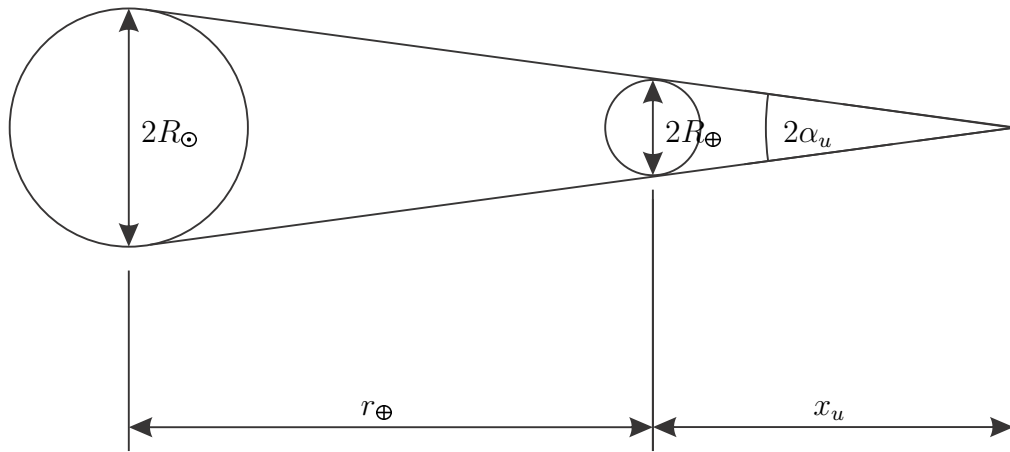


Figure 7.4: Geometry associated with the umbral cone. R_\odot and R_\oplus are the radii of the Sun and the Earth respectively. The distance between the Earth and the Sun is r_\oplus , allowing the calculation of the length of the umbral cone x_u and the apex angle α_u .

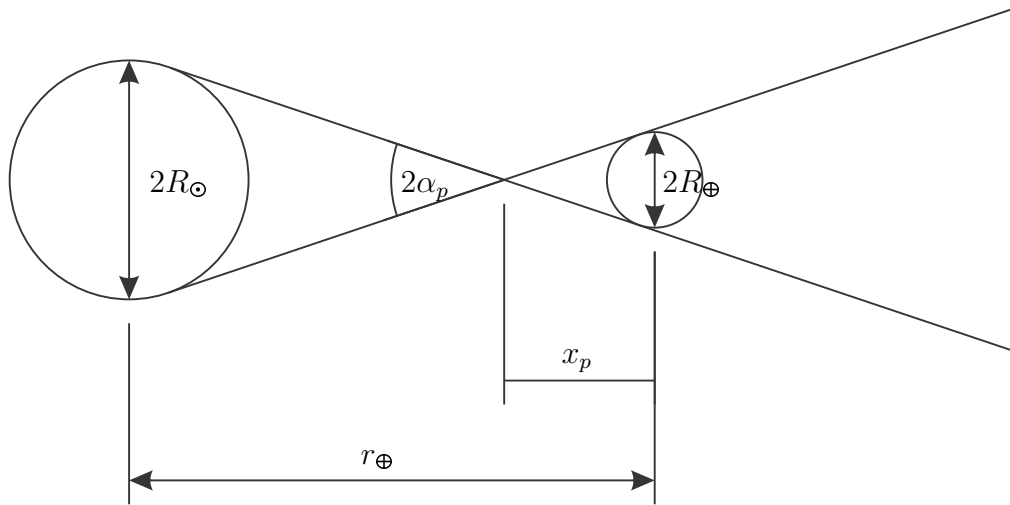


Figure 7.5: Geometry associated with the penumbral cone. R_\odot and R_\oplus are the radii of the Sun and the Earth respectively. The distance between the Earth and the Sun is r_\oplus , allowing the calculation of the length of the penumbral cone x_p and the apex angle α_p .

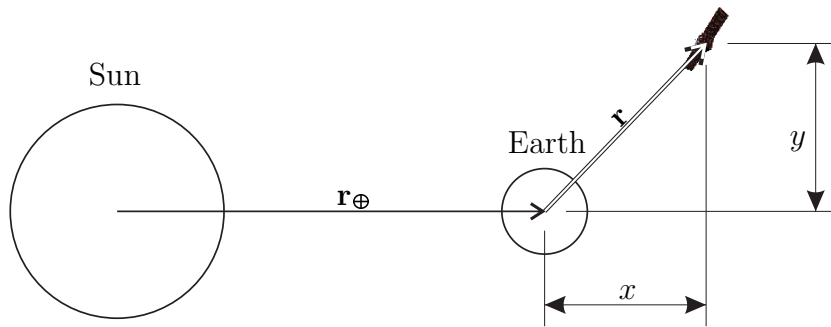


Figure 7.6: *Spacecraft position \mathbf{r} broken down into components x and y relative to Earth-Sun line \mathbf{r}_\oplus .*

Now the radii of the umbral cones at the satellite's position may be calculated,

$$y_u = (x_u - x) \tan \alpha_u, \quad (7.4a)$$

$$y_p = (x + x_p) \tan \alpha_p. \quad (7.4b)$$

Within this frame, if the spacecraft's position y is less than the radius of the umbral cone y_u , the spacecraft experiences total eclipse. If the spacecraft's position is more than the radius of the penumbral cone y_p , the spacecraft is in full sunshine. For simplicity, solar exposure within the penumbra was taken as a linear interpolation of position y between the umbral and penumbral cones. During lunar-centric phases the same equations apply but relative to the Moon $\mathbf{r}_\mathbb{C}$ rather than the Earth \mathbf{r}_\oplus .

7.3 Power

7.3.1 Power generation

At the commencement of this project, it was anticipated that power would be one of the defining factors in determining an optimal trajectory. Consequently power was implemented as one of the states to be tracked during

optimisation. The power generation, P , was calculated using

$$P = Q \times A_{eff} \times \eta_a \times \eta_c \times \eta_{DC} \times \cos \Psi_{\odot} \times \mathfrak{R}, \quad (7.5)$$

where Q represents the solar energy flux near the Earth-Moon system, A_{eff} is the effective area of the solar panels, η_a represents the area efficiency of the solar cells arranged within the panel, η_c represents the solar cell efficiency, and η_{DC} represents the efficiency of the voltage regulator. The angle subtended by the sun on the solar panels is Ψ_{\odot} , and the power degradation is \mathfrak{R} .

The solar energy flux is calculated by dividing the average solar luminosity (3.846×10^{26} W, Montenbruck and Gill 2000) by the surface area of a sphere with radius equal to the spacecraft's distance from the Sun ($4\pi r_{\odot}^2$). This is important because the Earth's distance from the Sun varies by 6% over the year (Montenbruck and Gill 2000) due to the eccentricity of its orbit. The solar intensity is then multiplied by the effective area of the solar panels, A_{eff} . Although the spacecraft has 6 m^2 of panels, because the central two panels are positioned at 45° the effective area is only 5.4 m^2 .

Based on the latest design work by my colleague Alexander Uryu, the area efficiency is about 0.8, that is, only 80% of the effective solar panel area will actually be covered in solar cells, due to the geometric arrangement of the cells and the additional surface area required for circuitry. The solar cells will be state-of-the-art TecStar GaAs/InP 34 series solar arrays with $200 \mu\text{m}$ front cover glass and $500 \mu\text{m}$ back cover glass. Consequently it is estimated that the cell efficiency will be about 27% at launch. The exact power control circuitry is not yet known, but based on modern power conversion circuits it is expected that the DC voltage regulator will be approximately 85% efficient.

It is assumed that while one axis of the solar panels is constrained to the thrust vector \mathbf{u} , the other is free to rotate about the thrust vector to obtain the best sun angle possible. Consequently the sun angle can be

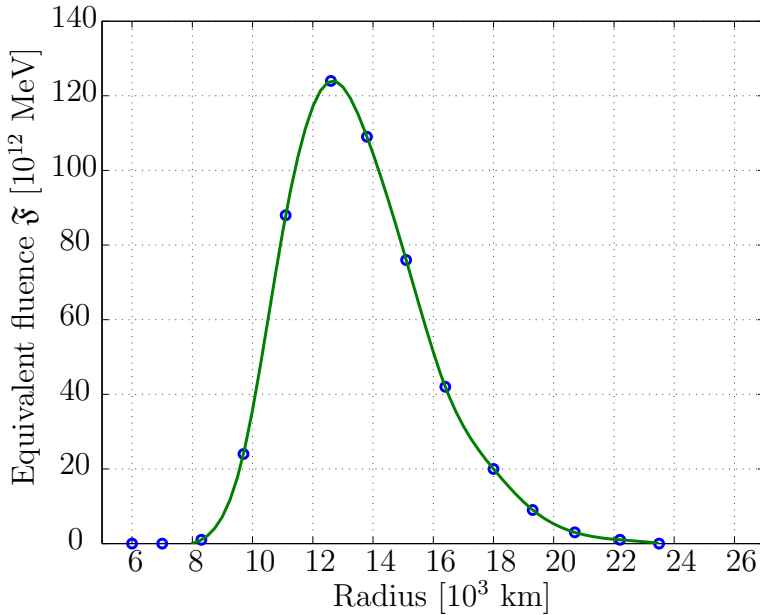


Figure 7.7: Radiation fluence during a 24 hour orbit as a function of distance from Earth, based on data from Erb (2002). The obvious peak is due to the higher concentration of radiation in the van Allen belt.

calculated by

$$\mathbf{u} \cdot \mathbf{r}_\odot = r_\odot \cos \Psi_\odot, \quad (7.6a)$$

$$\Psi_\odot = \arccos \frac{\mathbf{u} \cdot \mathbf{r}_\odot}{r_\odot}. \quad (7.6b)$$

The greatest unknown in the power model is how much the solar cells will degrade over time. As Erb (2002) points out, the solar panel degradation, \mathfrak{R} , is directly related to total equivalent *fluence*, \mathfrak{F} (that is, the radiation dose received), which must be integrated over the transfer, where the derivative with respect to time $\frac{d\mathfrak{F}}{dt}$ is approximated as a function of the distance from Earth, as shown in Figure 7.7.

At each time step the equivalent radiation dose of a 24 hour orbit may be taken from the plotted function, and scaled to the appropriate time interval. This effective radiation dose is added to the accumulated radiation dose. The total accumulated radiation dose may be translated

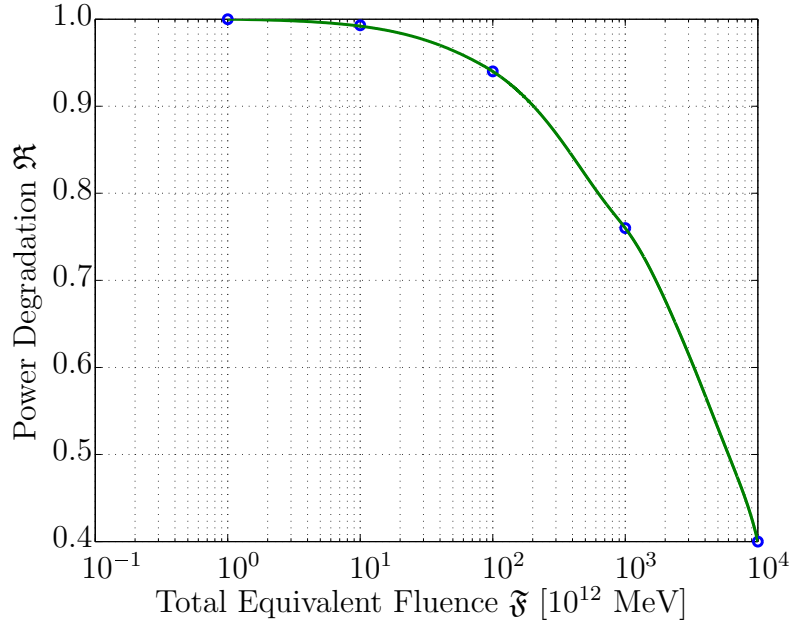


Figure 7.8: Power degradation as a consequence of radiation fluence, based on data from Erb (2002).

to a power degradation factor using Figure 7.8.

Data for the panel degradation model was based on the work done by Hechler (2002) during planning for the SMART-1 mission, via Erb (2002). During the SMART-1 mission, it was found that their solar cells degraded by approximately 0.12% per day, or about 2 W (Racca 2003b). It was also found that during a solar storm on 20 October 2003, an additional 1% panel degradation occurred (Racca 2003c). However, soon after the solar storm, the spacecraft reached a periapsis of 11790 km whereupon no further radiation damage occurred. Thus it can be assumed that the phase boundary defined in the mission architecture may be quite conservative, which should be factored into further power degradation modelling if not simply changing the mission architecture.

7.3.2 Power consumption

At each timestep of the simulation the power required for communications, payload and thrust should be subtracted from the power generated. The power requirements are summarised in Table 7.1.

The payload has not yet been confirmed, but it is expected that most of the payload will be in standby until the spacecraft is confirmed in the science orbit, so power requirements during the transfer will be minimal. During the science phase the payload is expected to require a maximum of 300 W (Institut für Raumfahrtssysteme, Universität Stuttgart 2008), recently refined to 42 W (Laufer 2010), which should be well within the solar panels' remaining capacity.

Agreements are being negotiated with ground stations in Stuttgart, USA, Japan and Australia to give continual access to the satellite during Earth orbit. The only downtime will occur in the later stages of the transfer, when the satellite transits through the Moon's shadow. Access time notwithstanding, the satellite will have to rotate to point its antennae towards the Earth during transmission. Therefore it is expected that communications will only operate a fraction of the transfer time. These communications intervals will be scheduled based on availability of both power and coasting phases. Since the frequency, duration and bandwidth required for transmissions are not yet known, they were not factored into the trajectory design. During communications intervals a maximum of 250 W will be required for the Ka-band transmission, and 10 W for the S-

Table 7.1: *Power requirements for Lunar Mission BW-1*

Subsystem	Power required
Arcjet	801 W
PPTs	208 W
Payload (standby)	Estimated max. 10 W
Payload (active)	42 W
Communications	Estimated 80 W
Mission computer	Estimated max. 10 W

band (recently revised to 60 W for Ka-band and 20 W for S-band, Laufer 2010).

After thruster power is also subtracted from generated power (see Section 7.1), any surplus power generated by the solar panels is added to the battery levels, or any deficit is subtracted from them. According to the initial design stated by Falke et al. (2004), the lithium ion batteries were designed to hold 100 Ah supplying a common bus of 28 V. It is assumed the batteries will be fully charged at launch. At any stage during the transfer, if the batteries become fully charged the spacecraft will roll around its thrust vector to point the solar panels away from the Sun, thus preventing overcharge.

While the capacity and corresponding weight of the batteries have been defined, the exact batteries themselves have not yet been chosen. Consequently issues like degradation over repeated charge/discharge cycles and trickle charging have not been considered in this work.

7.4 Parameterisation

7.4.1 Thrust profile parameterisation

Due to the strongly non-linear variations of the transfer relative to departure date (periodic over 27.5 days based on the Moon’s orbit), a good parameterisation of the departure date would be to use two variables, one to increment an integer number of lunar months forwards or backwards, the other a floating point capped at ± 0.5 to indicate the fraction of a month either side. This would allow the optimiser to find the optimal time of month for a launch, and therefore the optimal position of the Moon, to achieve lunar capture. Then the optimiser can adjust the month forwards or backwards based on other variations in the search space. While this parameterisation would assist in developing a truly optimal solution, since the departure date is not negotiable beyond the time spent in the GTO parking orbit it was not implemented at this time.

An additional parameterisation considered to decrease the numerical

complexity of the optimisation was to model the thrust duty cycle as a percentage of the orbit. Depending on the phase objective, a thrust segment was centred around either the periapsis or the apoapsis, with a parameter controlling length of the thrust segment. However, when implemented as a constant throughout the phase replacing the continuous thrust magnitude, the optimiser's flexibility is severely compromised. When implemented as a constant throughout the phase in addition to the thrust magnitude parameter, there is no improvement in computational load. An alternative would be to implement duty cycle as a continuous variable. The computational load is just as great, but the author suspects that this modification would significantly smooth the search space. Unfortunately, due to the complications experienced when optimising the system with a continuous thrust magnitude parameter this modification was not trialled.

7.4.2 Discretisation

As mentioned in Section 3.3.3, numerical solution methods require the continuous state and control profiles to be discretised into a series of grid points or nodes. GESOP allows these grid points to be distributed arbitrarily over the independent parameter. Given the number of grid points required for low thrust transfers and how the shape of the trajectory can change during optimisation, anything other than a uniform distribution makes no sense.

As mentioned in Section 6.3, longitude was selected as the independent parameter to allow equiangular node distribution. As a rule of thumb, for the initial coarse mesh at least 10 grid points were implemented per orbit. As a result, the cruise phase had over 7300 grid points. Later in the project an automatic mesh generator was implemented in GESOP. Using this mesh generator based on an error tolerance of 10^{-4} gave a starting baseline of 20003 grid points for the cruise phase, equivalent to over 27 per orbit.

Within each of these shooting intervals, a finer mesh of control nodes may be specified. Multiple shooting methods allow the state and control

profiles to be approximated over each of these sub-intervals as a piecewise polynomial function. Thus, with enough control nodes, the state and control profiles appear almost continuously variable. Single shooting methods use only the major nodes, and ignore the control refinement mesh. Constraint violations are evaluated at each shooting node, although GESOP once again allows a finer mesh to be specified by the user. However, SOCS does not support additional constraint evaluations, and as a single shooting method it ignores the control refinement mesh.

Nonetheless, during optimisation the major control mesh undergoes repeated refinement until the optimisation and errors are within user-defined tolerances. At the time when the cruise phase optimisation was stopped (see Section 8.2.4), the mesh had been refined to 99979 grid points. The ascent phase also started from 20003 grid points and was refined to 29999 points by the time it found a feasible solution with a targeted optimisation tolerance of 10^{-4} , constraint tolerance of 10^{-5} and ODE tolerance of 2×10^{-5} . For comparison, the reduced complexity ascent phase (see Section 8.2.2) was started from 1002 grid points, and reached 13990 points by the time it found an optimal solution.

Betts (1998) provides a simple algorithm to estimate the number of variables, n , required in a large optimisation problem, as a function of the number of states n_x , the number of control parameters n_u , the number of optimisable phases M and the number of gridpoints per phase N ,

$$n \approx (n_x + n_u)MN. \quad (7.7)$$

Given the problem formulation outlined for *Lunar Mission BW-1* in Chapter 6, the cruise phase alone generates 1.2×10^6 variables, substantially more than the 500,000 cited by Fischer et al. (2008) as the largest problem SOCS has solved.

7.5 Orbital behaviour

Previous theoretical analysis and numerical studies have identified a number of phenomena related to orbital transfers. A description of the theory behind gravitational assists, the Oberth effect, and weak lunar capture as they relate to *Lunar Mission BW-1* is briefly presented here.

7.5.1 Gravitational assists

Due to the low thrust of spacecraft *Lunar Mission BW-1*, a substantial part of the orbit raising can be achieved by exploiting the gravitational pull of the Moon. This technique has been well studied, although previous higher-thrust missions did not find it efficient to attempt more than one or two lunar assists. Kemble (2006) explains that,

“It is possible to utilise lunar gravity to assist in the orbit raising prior to lunar encounter. This takes the form of a *gravitational pumping* effect if the correct phase with respect to the Moon can be established” (Kemble 2006, p.249).

He quantifies the benefit,

“A typical ΔV saving of 800 ms^{-1} is obtained by use of lunar gravity assist” (Kemble 2006, p.248).

Because lunar gravitational assists provide delta-v without fuel expenditure, they should be implicitly accounted for during optimisation. Preliminary results did indicate this to be the case, as seen in Figure 7.9. From an initial orbit of 180,000 km (semi-cis-lunar, representing the later stages of the cruise phase to highlight the lunar assist) the spacecraft takes two orbits to align its phase with the Moon, then receives a very apparent boost purely from the Moon’s gravity during the close passes seen in Figure 7.10.

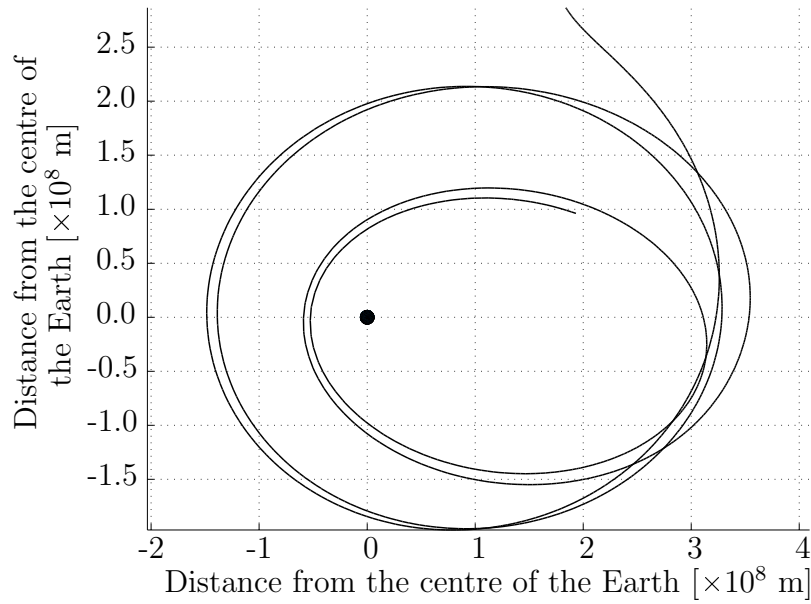


Figure 7.9: Trajectory of preliminary optimisation for Lunar Mission BW-1 showing a lunar resonance implicitly realised by the optimiser.

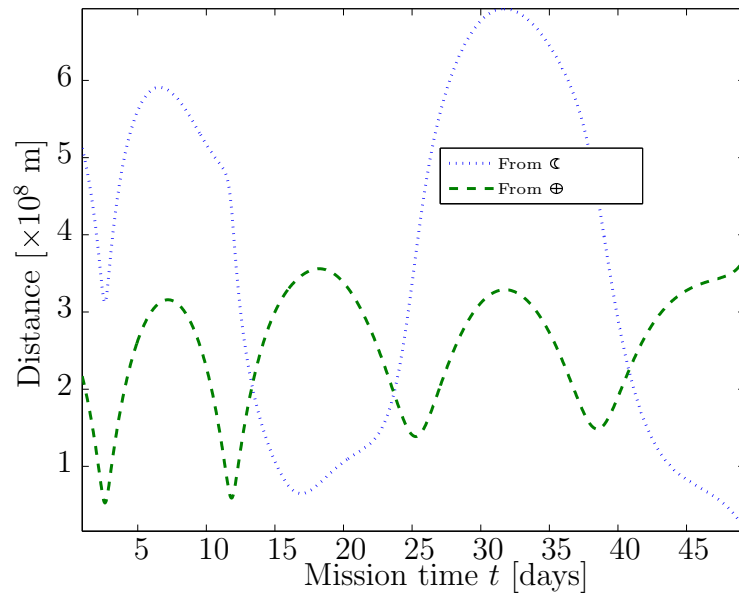


Figure 7.10: Distance of spacecraft from Earth and Moon during preliminary optimisation showing a lunar resonance implicitly realised by the optimiser.

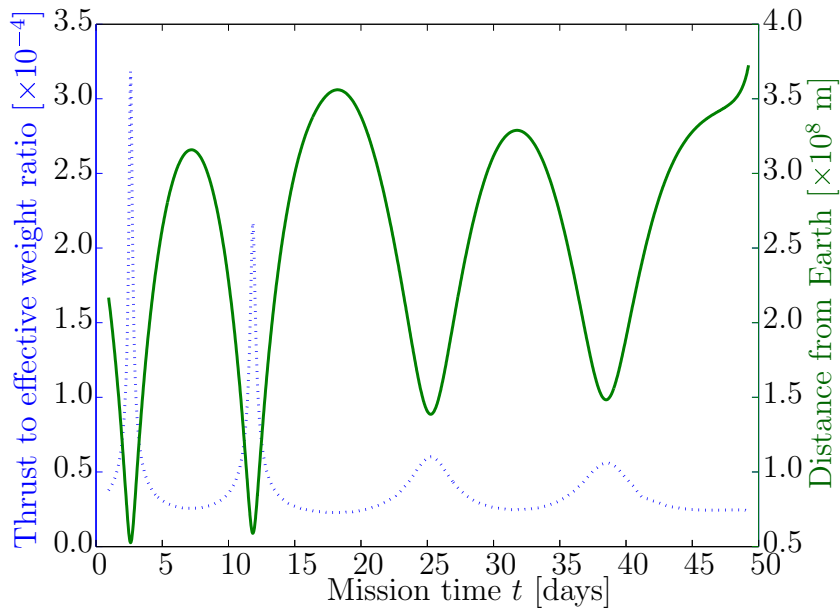


Figure 7.11: Thrust to effective weight ratio (darker line) plotted with distance from Earth (dotted line) during preliminary optimisation demonstrates the Oberth effect.

7.5.2 Oberth effect and optimal thrust profiles

It is well known that thrusting at particular points in the orbit is more efficient than others (Kemble 2006). Oberth (1923) states that the specific orbital energy gained per unit delta-v exerted is equal to the instantaneous speed. Therefore, thrusting is more efficient at high speed, which occurs at periapsis. This is known as the Oberth effect, and is demonstrated quite effectively in Figure 7.11 where the *effective weight* is the weight minus the centrifugal force due to the horizontal velocity.

Constant thrust (tangential to the orbital radius) leads to circular trajectories because an eccentric starting trajectory spends more time at apoapsis than periapsis; hence more impulse is imparted to the vehicle at apoapsis than at periapsis. As evident in a Hohmann transfer, thrusting at apoapsis circularises the orbit. Racca (2003a) found that tangential thrust is the most efficient way to increase the periapsis of a constant-thrust vehicle.

In a vehicle with variable thrust however, the majority of the thrusting should occur near perigee; there is an inverse relationship between optimal thrust magnitude and orbital radius. However, the ascent phase of *Lunar Mission BW-1* requires raising the periapsis above the van Allen belts as quickly as possible. This may be achieved by focussing thrust around the apoapsis; unfortunately this also minimises the orbital energy gained per unit of propellant expended. Consequently, in the subsequent cruise phase once the periapsis requirement is removed and the sole aim is to gain orbital energy as efficiently as possible, it would be expected that thrust is focussed around the periapsis. Racca (2003a) found that the most efficient thrust profile for a constant-thrust vehicle to increase orbital energy (proportional to semimajor axis) is to thrust along the velocity vector. However, *Lunar Mission BW-1* requires additional manoeuvres during each phase to achieve the boundary conditions of the next phase.

In addition to orbital energy and the corresponding semimajor axis, there are well established strategies for efficiently changing other orbital parameters. For example, Edelbaum (1964) demonstrates that the argument of periapsis (ω) is most efficiently changed during a low eccentricity orbit and that the inclination (i) is most efficiently changed at high eccentricity. These results have often been used to anticipate thrust profiles within low-thrust trajectory studies such as Dachwald and Ohndorf (2007). Pollard (2000) and Herbiniere et al. (2000) further describe a number of steering programs for low thrust orbital manoeuvres. Gao (2008) introduces a convenient mathematical parameterisation scheme that generates continuous, smooth parameters describing thrust steering, and can easily be used in an optimisation engine. This modification may be useful to improve the computational complexity in the future, but has not been implemented in this thesis. Nonetheless, the optimiser must adjust the orbital elements during the cruise phase using a combination of these semi-optimal thrust profiles in order to set up a lunar capture.

7.5.3 Lunar capture

A spacecraft orbiting the Moon (in the same direction as the Moon orbits the Earth) undergoes a period of low velocity relative to the Earth every time it is on the Earthward side of the Moon. A spacecraft orbiting the Earth in a highly elliptical orbit undergoes a period of low velocity relative to the Earth when it reaches apoapsis, which is conveniently also the furthest point from the Earth. Therefore the aim to achieve lunar capture is to deliver the spacecraft at apoapsis to a “stationary point” in the intended lunar orbit, such that the Moon’s gravity will then pull it into a steady lunar orbit, avoiding the need for a high-thrust capture manoeuvre.

To maximise the gravitational effect of the Moon on the spacecraft, it should be phase-locked with respect to the Moon’s orbit. However, this would require constantly adjusting the orbital line of apsides, which is a high delta-v manoeuvre. Gravitational resonance is generally exploited by pointing the apoapsis towards the Moon’s ascending node (to remove any dependence on inclination) and adjust the orbital period to resonate with the Moon (that is, the ratio of the spacecraft orbital period to the lunar cycle is a rational fraction, for example the spacecraft completes two orbits to every lunar orbit, or three orbits to every lunar orbit, or five orbits to every two lunar orbits, etcetera). However, based on the unique thrusting constraints of *Lunar Mission BW-1*, an alternative optimal scenario may be to maintain the fastest part of the orbit (periapsis) within the Earth’s shadow (eclipse), to minimise the amount of time that the craft is unable to charge its batteries. In this scenario the spacecraft should also thrust as it passes through the eclipse since it cannot recharge during this time, and thrusting will help it to escape the eclipse as quickly as possible. Racca (2003a) found the SMART-1 trajectory was affected by the need to avoid eclipse, particularly at apoapsis.

Even with capture phases provided by arcjet, there is very little thrust available to perform lunar insertion. When simulating the transfer this problem is compounded by the fact that lunar insertion must be predicted very accurately, as simulating a lunar orbit in an Earth-centred frame, or

vice-versa, causes the trajectory to periodically appear to move backwards relative to the central body. In other words, the anomaly decreases, which causes computational errors.

In cases where the transition from Earth-orbit to lunar-orbit is predicted correctly, the simulation may be transferred from an Earth-centric frame to a lunar-centric frame. Unfortunately, this may still run into computational errors, as the spacecraft may be recaptured by the Earth.

Zero-thrust captures, also known as ballistic captures, have been studied by many authors, most particularly Belbruno and Miller (1993) following the partial failure of the Japanese Hiten probe. Belbruno exploited a low-energy transfer to recover the probe, prompting further study into the phenomenon he termed the *weak stability boundary*. This is a region around the body where the orbital energy is negative (that is, the spacecraft has technically been captured, and would orbit indefinitely in the absence of external forces) but the motion of the spacecraft is unstable. In the case of lunar transfers this is because the spacecraft is usually in a high energy orbit, and after some amount of time the Earth's gravity pulls it back into geocentric orbit. These *weak captures* are rigorously defined by Belbruno (2004).

Unfortunately all of Belbruno's work, and much of the remaining literature, concerns impulsive transfers following invariant manifolds while coasting between burns. Low-thrust transfers follow similar trajectories, but do not possess impulsive thrusters to provide large amounts of delta-v ensuring the spacecraft enters the desired manifold. Consequently even developing an initial guess for the optimisation proved challenging, and required extensive preliminary simulations as outlined in Section 8.2.

7.6 Summary of vehicle modelling

This chapter presented an assortment of important issues uncovered while modelling and optimising the trajectory of *Lunar Mission BW-1*. First, modifications to the differential equations of motion were required due to the implementation of equi-angular grid points over the trajectory instead

of equal-time grid points. Different techniques and models to discretise the thrust profile were discussed, and a number of recommendations were made for future revision of this work.

A discussion of the propulsion systems included performance modelling and potential improvements to the vehicle design. The models used for Earth and Moon shadow, power generation and consumption and degradation of the solar panels were then presented. Finally a number of important phenomena related to orbital mechanics that play a large role in the Earth-Moon transfer were explained, to aid in understanding the results presented in Chapter 9.

Chapter 8

Method

8.1 Introduction

This chapter first explains the different software packages used throughout this project, and then outlines the recommended procedure to determine a suitable trajectory for *Lunar Mission BW-1* once the launch details and configuration are confirmed.

8.2 Developmental procedure

8.2.1 Matlab modelling

As mentioned in Section 6.6, early in the project the orbital mechanics of Chapter 5 were modelled in Matlab to verify the flight mechanics and resolve numerical issues associated with long-duration integration and frame conversion. Matlab's native optimisation procedures were examined, but found inadequate for the number of variables required.

8.2.2 GESOP modelling

Development was then transferred to GESOP. The model library and graphical front-end ASTOS was briefly used but found to be far to restricting for a problem of this complexity. Consequently the vehicle and orbital

mechanics were coded to the C interface available within GESOP. In addition to encapsulating several optimisation procedures, GESOP provided automatic mesh generation as explained in Section 7.4.2, given appropriate error tolerances as explained in Section 6.6.1.

To get an initial idea of the optimal thrust profile, first a reduced complexity ascent trajectory was modelled. This was implemented simply by deactivating secondary and tertiary perturbations, and optimising over a coarse mesh. As a result, this phase was quickly able to reach an optimal solution, giving an idea of the optimal results that would have resulted in the other phases given adequate computing power. Many useful observations were drawn from this preliminary optimised trajectory, so the results have been included in Chapter 9.

Following the reduced complexity ascent, optimisation was attempted for a reduced complexity cruise phase. However, due to the long duration of this phase and the limited computer resources available, the optimisation did not reach an optimal solution in the time available. This exercise did highlight other problems with the procedure, in particular determining a lunar capture. Due to the lunar orbit being very close to the orbital escape energy relative to the Earth (only $5 \times 10^5 \text{ m}^2\text{s}^{-2}$), the vast majority of simulations resulted in the spacecraft escaping the Earth's sphere of influence by gaining a gravitational assist from the Moon. This caused severe computational errors as the longitude and anomaly are no longer independent parameters after escape. Another common failure scenario involved weak capture by the Moon; after one or two orbits around the Moon the spacecraft would then be recaptured by the Earth. Due to the way the system was modelled, this once again caused computational errors: if the spacecraft is in orbit around the Moon in a Earth-centric frame, the anomaly becomes sinusoidal rather than always increasing; the same applies for a spacecraft in Earth orbit during a lunar-centric frame.

Determining conditions for strong lunar capture proved difficult and unreliable. Consequently it was decided to simulate the transfer backwards, from lunar orbit to Earth orbit, using an industry standard tool called Satellite Tool Kit (STK). Backwards propagation has been used by many

previous authors, such as Kluever and Pierson (1995). The main advantage to this approach is that any ascent from lunar orbit must necessarily pass through Earth orbit, whereas the reverse does not apply. Furthermore, with the Moon in a 19° inclined orbit about the Earth, any ascent from the Moon will end up in approximately the same plane as the parking orbit after launch, thus implicitly accounting for the plane changes required to achieve the target lunar orbit. Backwards propagation is particularly well suited to this real-world application, because once the payload mass is finalised backwards propagation allows exact determination of the wet mass required.

8.2.3 STK modelling

As outlined above, the Satellite Tool Kit (STK), provided by AGI (Analytical Graphics, Inc.), was chosen to model the trajectory. STK is widely used in industry for defence and space simulation, and has developed an extensive collection of features. Recent developments have even included an optimiser for interplanetary trajectories. Unfortunately, the native optimiser still only supports a very limited number of optimisable parameters, for example the direction and magnitude of an impulsive burn to perform a trans-lunar injection. The high number of parameters resulting from discretisation of a continuous trajectory is, for the moment, beyond the capabilities of STK, even to the extent of solving the 2-point boundary value problem (in other words, STK cannot find a feasible solution to the problem let alone optimise it).

Therefore STK cannot target a specific orbit, such as the correct inclination and eccentricity of the GTO (after backwards propagating from LLO). However, as stated above, the fact that any ascent from the Moon passes through Earth orbit, with an inclination of approximately 19° means that it can be a very useful tool to study lunar capture. A number of backwards propagations were performed, mostly resulting in escape orbits. However, by manipulating the start date and anomaly, it was found that some “ascents” would put the spacecraft into a stable Earth orbit

(provided the thrust stops once lunar escape is achieved). From this point a geocentric frame of reference could be implemented and the PPTs could lower the orbital radius of the spacecraft relative to the Earth. Once the PPT “descent” reaches the van Allen belts for the first time, this is equivalent to the last time the spacecraft would be within the van Allen belts in the chronologically correct simulation, and consequently defines the phase boundary perfectly.

Due to the limited number of optimisable parameters, the thrust vector must be easily defined relative to one of the STK frames. For the purposes of this simulation, the thrust vector was defined to be negative velocity for the lunar phases, and positive velocity for the geocentric phases. One of the resulting trajectories is shown in Figure 8.1. The trajectory smoothly “ascends” from LLO by thrusting along the negative velocity vector, transitions cleanly into Earth orbit, and then “descends” by thrusting along the velocity vector. Because of STK’s inability to target specific orbits, the “descent” leaves the spacecraft in the same inclination orbit it ended up in after finally escaping the Moon’s gravity. The limited, predefined thrust angles mean that orbital eccentricity cannot be controlled either. Consequently the final arcjet phase was not propagated through to GTO.

Thus the STK simulation solves the problem of lunar capture, but further work was required to determine a feasible end-to-end orbit even before any optimisation could take place. In order to manipulate the thrust profile during the forwards ascent and cruise phases such that the initial GTO could connect with the lunar capture, it was necessary to reproduce this trajectory in GESOP.

8.2.4 Further GESOP modelling

The ascent phase was modelled in GESOP subject to the initial boundary conditions outlined in Table 6.1 and final boundary conditions outlined in Table 6.2. An initial guess was taken for the thrust profile perpendicular to the orbital radius at all times throughout ascent, in order to raise the periapsis as quickly as possible beyond the van Allen belts.

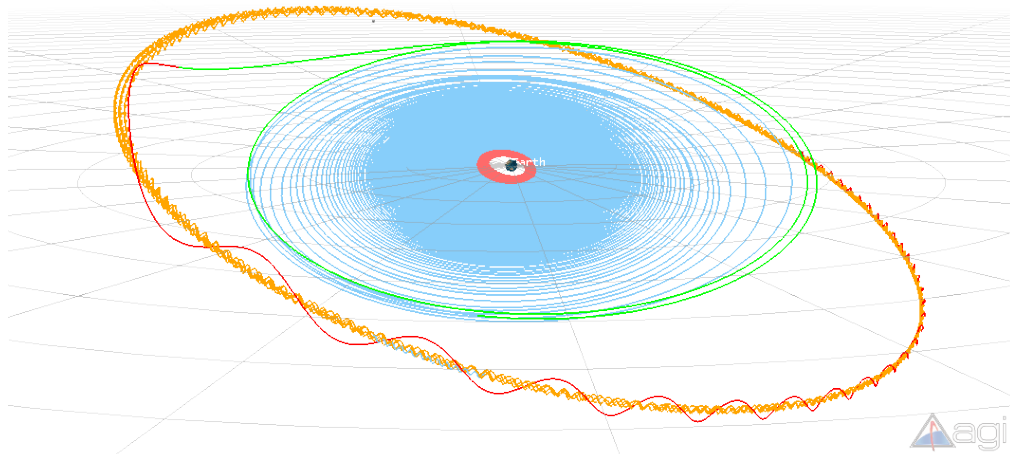


Figure 8.1: Continuous trajectory modelled in STK.

The initial guesses for starting time and mass were taken from the STK simulation described in Section 8.2.3. End conditions were imposed to connect this phase to the starting conditions of the cruise phase. This implementation of continuity is not ideal as it enforces an arbitrary position and velocity at the phase transitions, thus reducing the flexibility during optimisation. A long-term goal remains to optimise all phases simultaneously, enforcing continuity between phases but not specifying what those conditions are. However at this stage this is not possible due to computational complexity, and remains an improvement for the future, perhaps exploiting parallel processing and supercomputer hardware.

Given the arbitrary nature of these continuity conditions, they were used for the initial guess but not enforced during optimisation. As the actual parameters diverged from their initial values during the optimisation, discontinuities emerged between phases. This was permitted for a number of reasons. Firstly, the launch conditions are not known, so the procedure used in this optimisation is more important than the actual result. Secondly, at every phase transition the terminating and commencing orbits are very similar, thus the variation in orbital energy was very small. In other

words, the main difference between the orbits was simply timing, and at any of the phase transitions the spacecraft can sit in a parking orbit until the correct alignment occurs. Finally, due to the computational limitation of optimising each phase independently, any small change would then require all other phases to be recalculated. Treating each separately, with an implicit parking orbit in between, allows these small changes without any significant effect to the remaining phases.

As mentioned in Section 7.3, throughout the modelling and optimisation of the cruise phase, multiple different initial guesses were trialled. Ultimately it was decided that the initial specification for vehicle performance provided the best trajectory conditions, and consequently those same parameters were used in the STK simulation mentioned in Section 8.2.3. The STK trajectory was then used as an initial guess for the cruise phase, subject to boundary conditions as outlined in Section 6.5. Once again, the cruise phase is not continuous with preceding or succeeding phases, but the orbital energy at the phase boundaries is very similar allowing some design flexibility.

The 1.2×10^6 variables required to compute the cruise phase, as outlined in Section 7.4.2, resulted in 2×10^8 64-bit doubles for floating point operations and 8×10^7 32-bit words for integer operations. The desktop PC kindly provided by the Institute of Space Systems in Stuttgart, an AMD 2.8GHz X6 with 2GB RAM, was unable to handle a problem of this order. Despite an upgrade to 4GB, the cruise phase optimisation was still sluggish, resulting in the program terminating before it could achieve an optimal solution. The processing was severely restricted by not being distributed across the multiple cores available. To enable this, both GESOP and SOCS would have to be modified to support parallel processing. This would not only improve performance on desktop PCs given the market trend for multiple cores, but would allow large optimisation problems to be solved on clustered PCs, or even supercomputers. Unfortunately this development was beyond the scope of the project, so modelling proceeded to the remaining phases.

The initial mission architecture did not include a propagate phase, but

during the STK simulation it was empirically found that the spacecraft achieves an appropriate orbit for lunar capture well before the Moon is in position for rendezvous. Consequently a coasting phase was inserted, when the spacecraft's trajectory was propagated forward in time without any thrusting. Given sufficient computational power, this phase could be shortened or removed entirely, much like the discontinuities between other phases, once the launch conditions are known. Whether this phase should be removed remains open to debate: it provides the spacecraft with an opportunity to recharge its batteries if the electrical system is not performing nominally, and allows time for critical adjustments if the spacecraft is drifting off course. The lunar approach is particularly important to ensure the final science phase orbit can be achieved without requiring too much propellant.

Throughout the propagate phase the spacecraft transitions from the Earth's sphere of influence to the Moon's. Consequently longitude was discarded in favour of time as the independent parameter for modelling this phase, as all the benefits outlined in Section 6.3 are not applicable to this phase.

The various considerations in each of the phases introduced in Table 1.2 are outlined in Table 8.1.

8.2.5 Data analysis

During development, data was reviewed using the GESOP graphical interface. At the conclusion of work, the data files were imported into Matlab to produce the plots shown in this thesis. As explained in more detail in Section 9.9, the control and time vectors were post-processed in Matlab to fit the STK interface, to verify the orbital mechanics modelling.

8.3 Final trajectory determination

The primary objective of this study was to determine a procedure for finding a suitable trajectory once the launch details are known. Launch

Table 8.1: Operational differences between phases when modelling Lunar Mission BW-1

Phase	Requirement
Ascent	
Frame	ECI
Thruster	Arcjet
Independent parameter	Longitude
Notes	Earth eclipse very important Radiation dose very important
Cruise	
Frame	ECI
Thruster	PPT
Independent parameter	Longitude
Propagate	
Frame	ECI
Thruster	Unpowered
Independent parameter	Time
Capture	
Frame	LCI
Thruster	Arcjet
Independent parameter	Time
Descent	
Frame	LCI
Thruster	PPT
Independent parameter	Longitude
Notes	Lunar eclipse very important
Science	
Frame	LCI
Thruster	Unpowered
Independent parameter	Longitude
Notes	Lunar eclipse very important Increased payload and communications power requirements

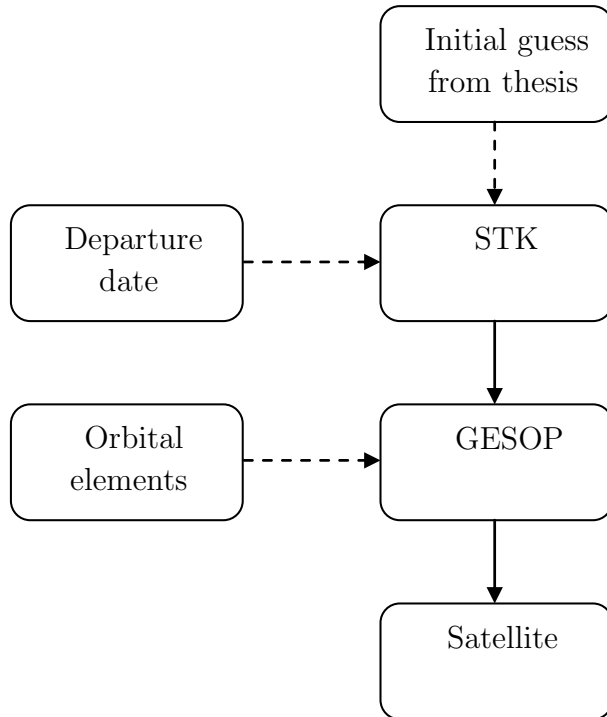


Figure 8.2: Flowchart demonstrating the trajectory development process for Lunar Mission BW-1.

configuration can be finalised before launch, but any launch can be postponed or scrubbed due to technical faults or even adverse weather. Therefore the trajectory can be approximated, but not finalised before launch. Once the spacecraft is safely in GTO, the orbital elements must be fed in to the optimisation process, and the resulting thrust profile uploaded to the spacecraft on-orbit. This procedure is graphically represented in Figure 8.2.

First of all, the indicative results presented here may be used to estimate flight time, to produce a backward propagated trajectory in STK that departs GTO on a suitable date after launch. The capture and propagate phase durations may be adjusted to determine a lunar capture. Once a capture scenario is achieved, the state vector at each phase boundary must be inserted into GESOP as an initial guess prior to the optimisation process.

The optimisation process within GESOP then commences. Given the present computational limitations, each phase must be optimised, then continuity conditions must be adjusted between phases. This iterative process is repeated until a smooth, continuous trajectory is achieved. Obviously, this process is not ideal. Assuming SOCS and GESOP have been adapted to support parallel processing, the phases may be appended into one large optimisation problem with many million parameters, which may then be optimised in one run.

Data files containing the control profile are output by GESOP. These may be post-processed, within GESOP or another application, to a format appropriate for the satellite ACS, before being uploaded to the satellite. During the transfer the anticipated trajectory should be matched against the observed trajectory, and recalculated as required (this will be particularly important early in the trajectory, as thruster performance is evaluated).

8.4 Summary

This chapter clarified the software packages used throughout this project, and some of the problems inherent with each. A brief roadmap was then given to apply this procedure, after launch, to determine the final trajectory.

Chapter 9

Discussion of results

9.1 Introduction

This chapter presents the results obtained through GESOP simulation and optimisation of each of the phases as introduced in Table 1.2, as well as the reduced complexity ascent phase and propagate phase introduced in Chapter 8.

9.2 Reduced complexity optimisation

As explained in Section 8.2, a reduced complexity ascent phase was modelled to gain an initial idea of the thrust profile and optimisation procedure. Many useful conclusions can still be drawn from the results of this simulation. The thrust profile shown in Figure 9.1 demonstrates oscillations in the thrust direction between radial and tangential thrust components. This is similar to a result found by Betts and Erb (2003). However, unlike Betts and Erb (2003), this is accompanied by a varying thrust magnitude, as shown in Figure 9.2. It is interesting to note that the variations in thrust magnitude are synchronous with the orbit; during the apoapsis, when thrusting is most effective in raising the periapsis, the thrust magnitude is very near to 100%. Towards the end of the phase however, near periapsis the spacecraft often ceases thrusting altogether. The fact that

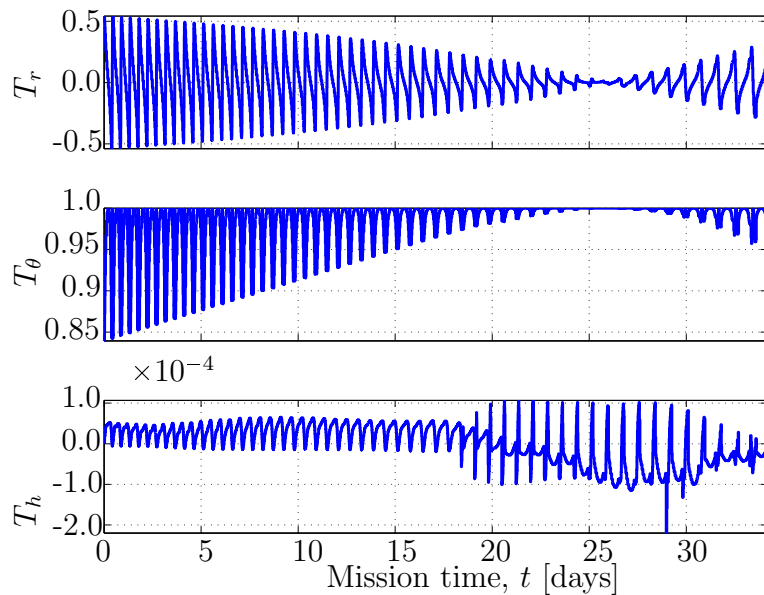


Figure 9.1: Direction of thrust vector during reduced complexity ascent phase. T_r is the radial component, T_θ is the tangential component within the orbital plane, and T_h is the out-of-plane component.

thrust is continuous at the start of the phase is a result of the Oberth effect: it is most efficient to thrust when close to the central body. However, once sufficient orbital energy is attained for the periapsis to be raised beyond the van Allen belts, thrusting near periapsis contributes nothing more to achieve the objective. Thus a major objective of this study is achieved: to discover an optimal thrust profile given the thrust constraints.

The resulting trajectory presents some interesting artefacts in the 3D plot in Figure 9.3. Once thrusting at periapsis ceases, the apoapsis stops increasing significantly. Thus the orbits are much closer together in the plot, appearing as though an inclination change has occurred.

The terminal condition of this phase optimisation, raising the periapsis above the van Allen belts, is shown in Figure 9.4. The cyclical nature of periapsis growth is due to the orbit: the periapsis height cannot be raised while the spacecraft is at periapsis, regardless of the amount of thrust applied. As a result of this effect, the optimised profile reduces thrust

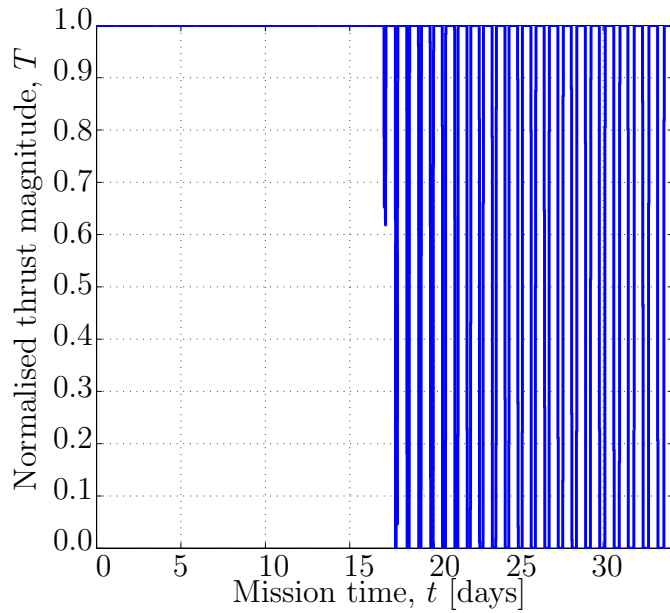


Figure 9.2: Magnitude of thrust vector shown in Figure 9.1 during reduced complexity ascent phase.

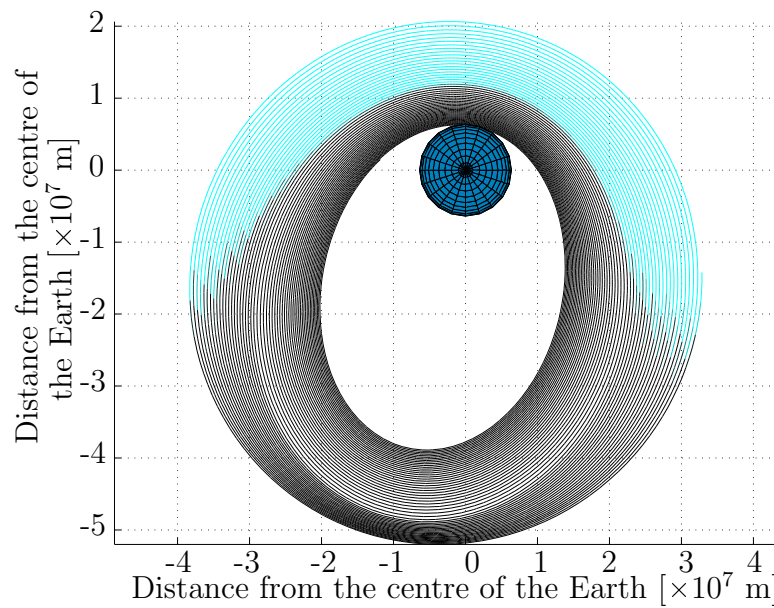


Figure 9.3: Reduced complexity ascent trajectory of the satellite in ECI frame viewed from north pole. Black represents full thrust magnitude, cyan represents zero thrust magnitude.

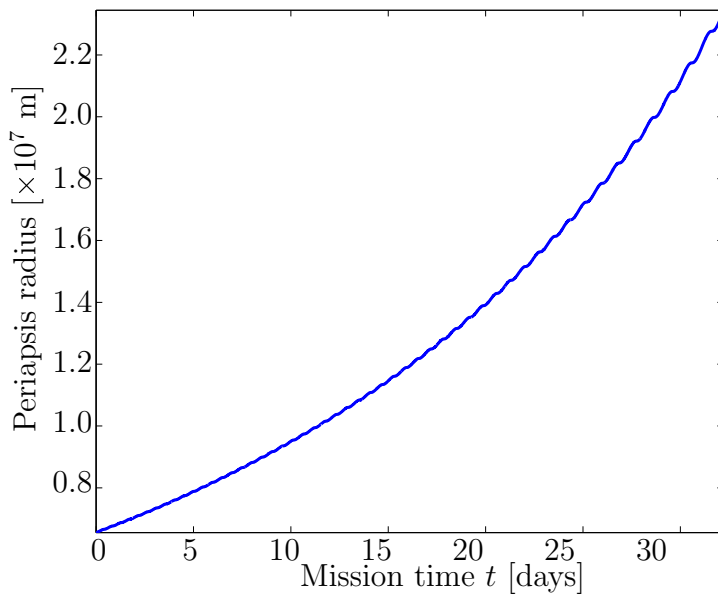


Figure 9.4: *Periapsis of spacecraft during reduced complexity ascent phase.*

during apoapsis, thus conserving fuel when it is inefficient to thrust. Each of the sharp increases in periapsis corresponds to an apoapsis pass. The spacecraft's mass, seen in Figure 9.5, shows a steady decrease during the period of constant thrust. Then the latter half of the phase shows the results of the variable thrusting magnitude, as fuel mass is conserved at the expense of time. Consequently, this simulation used a total of 53.63 kg of ammonia, over 34.17 days. This is very close to the original mission architecture's estimation of time spent in the van Allen belts, and thus corresponds to acceptable levels of radiation damage.

The Δv expenditure in Figure 9.6 shows a very similar profile to mass flow, albeit inverted, adding up to a total of about 1.15 km s^{-1} . This is very close to the expenditure estimated in the original mission architecture of 1.1 km s^{-1} .

Finally, Figure 9.7 shows the power levels throughout this phase. The energy used by the thrusters very closely maps the energy generated by the solar panels, until the later stages whereupon the intermittent thrust-

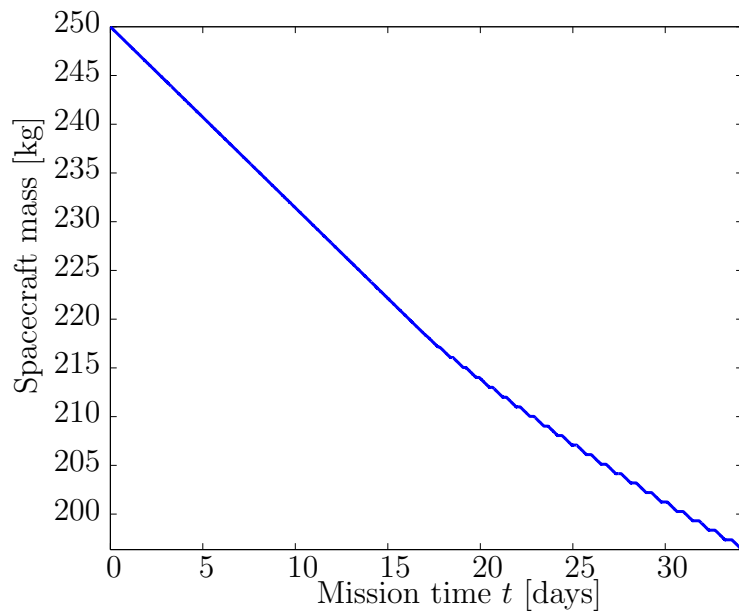


Figure 9.5: Mass of spacecraft during reduced complexity ascent phase.

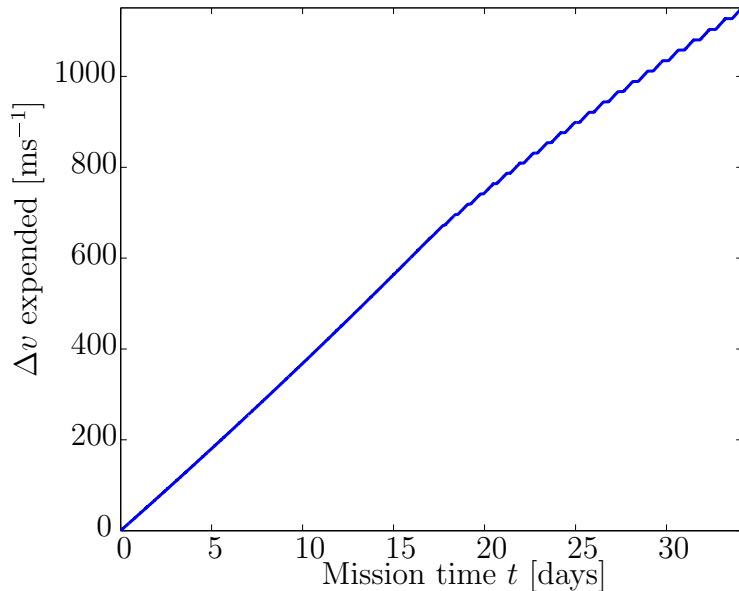


Figure 9.6: Delta- V generated by spacecraft during reduced complexity ascent phase.

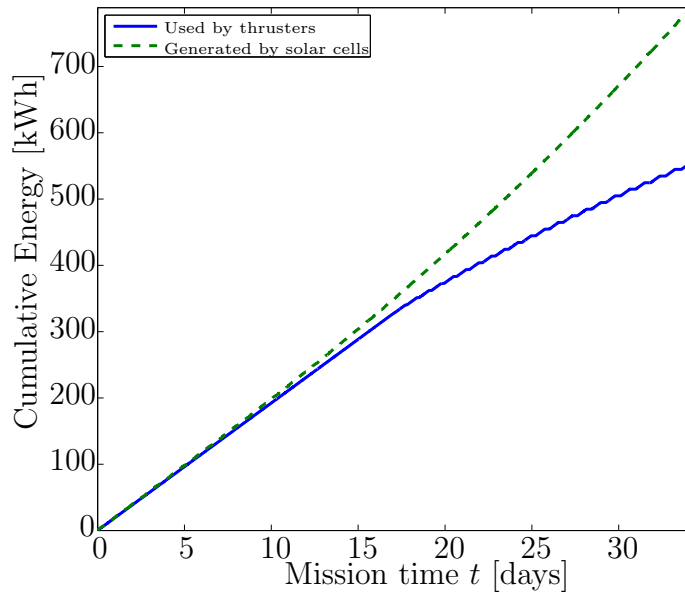


Figure 9.7: Power budget of spacecraft during reduced complexity ascent phase.

ing occurs, lowering the energy requirements. Thus the constraint that the energy use does not exceed the energy generation by more than the batteries' capacity is fulfilled.

9.3 Ascent phase

Figure 9.8 shows the 3-dimensional trajectory that resulted from the ascent phase. This optimisation was able to reach a feasible solution in the computational time available, but was not allowed to continue on to find an optimal solution. Consequently the ascending orbit does not show the Oberth effect to the same degree as in the reduced complexity optimisation.

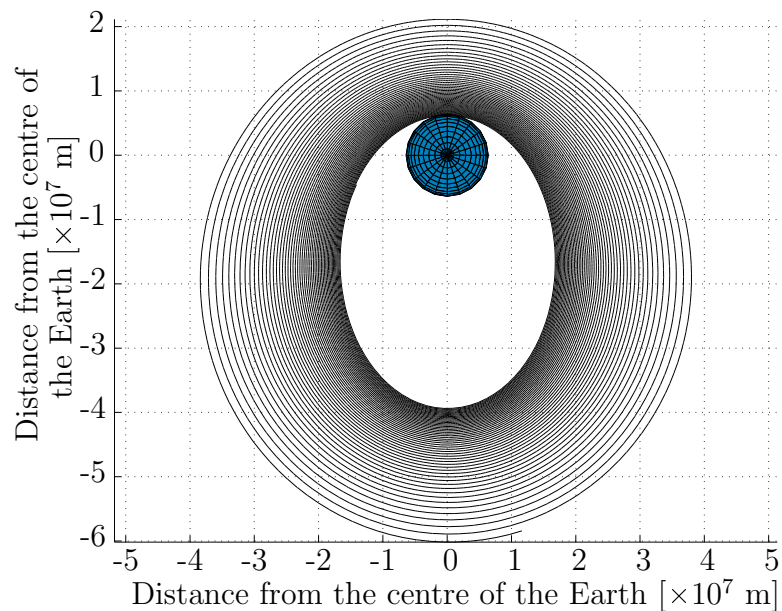


Figure 9.8: Ascent trajectory of the satellite in ECI frame viewed from north pole.

Figure 9.9 shows the distance of the spacecraft from the Earth and Moon throughout the phase. The oscillations about the Earth are seen to slowly increase in duration and altitude, as you would expect for a slowly ascending orbit. For this scenario, the geometry permitted the spacecraft's apoapsis (furthest point from the Earth) to pass near the Moon's periapsis (closest point to Earth). This is an optimal scenario, as it leads to much greater gravitational assistance earlier on in the transfer, but is unfortunately not a scenario that can be planned for, as the initial argument of periapsis is defined by the launch. The optimisation is able to implicitly

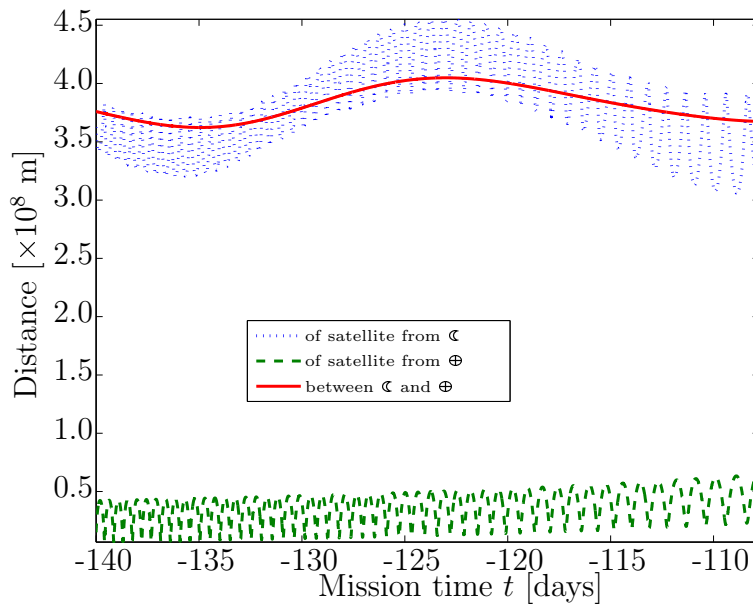


Figure 9.9: Satellite's distance from Earth and Moon during ascent phase.

adjust the argument of periapsis during the transfer by controlling the thrust angle, but this technique requires a lot of delta-v and therefore can only compensate for a few degrees.

The thrust profile calculated by the optimisation is shown in Figure 9.10, along with the corresponding thrust magnitude in Figure 9.11. While the scale of these results seems trivial, they are indicative of the direction the optimisation was pushing the solution, and suggest that the reduced complexity results constitute a good approximation.

Figure 9.12 shows the changing equinoctial elements of the orbit throughout the transfer, accompanied by the rather more intuitive Keplerian elements in Figure 9.13. Unsurprisingly, the semimajor axis a and the semilatus rectum p grow smoothly throughout the transfer, and their rate of growth increases as the spacecraft gets further from Earth's gravity well. The anomaly ν slows its growth as the orbital radius, and consequently the orbital period, increases. The spacecraft's eccentricity e slowly decreases as the continual tangential thrust raises the perigee faster than the apogee, but again, this is exactly as required during this phase. The

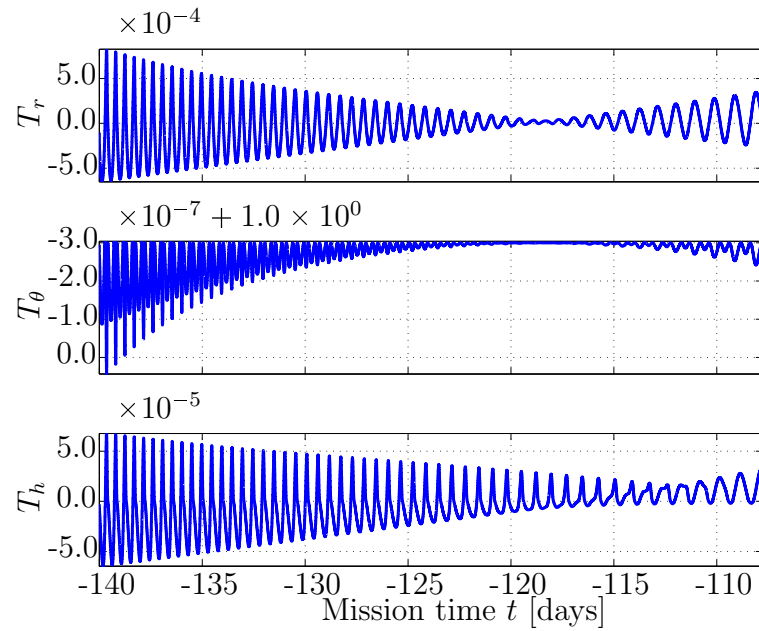


Figure 9.10: Direction of thrust vector during ascent phase.

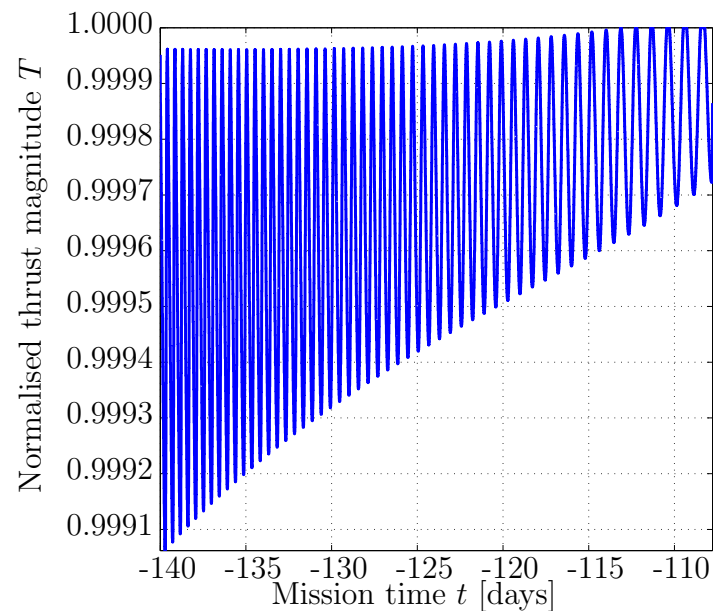


Figure 9.11: Magnitude of thrust vector during ascent phase.

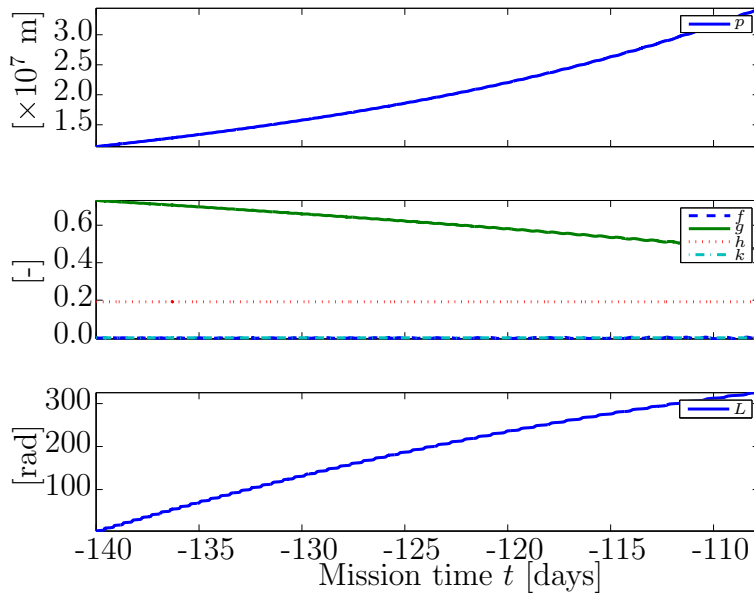


Figure 9.12: Equinoctial elements of satellite within ECI frame during ascent phase.

continual thrust in this phase, when compared with the optimised thrust of the reduced complexity phase, results in a higher final semimajor axis accompanied by a higher eccentricity.

The stronger forces acting on the spacecraft during the ascent phase are shown in Figure 9.14a, and the weaker forces in Figure 9.14b. It is immediately apparent that only the Earth's oblateness plays a significant role in defining the spacecraft trajectory from such a low orbit. However, as outlined in Section 5.5.2 this only affects the argument of periapsis and right ascension of the ascending node, and therefore cannot be exploited to raise the orbit faster. As outlined above, adjusting the argument of periapsis may assist with lining up gravitational assists from the Moon later in the transfer, but due to the limitation of modelling phases separately this assist could not be included. Consequently, the thrust profile was optimised purely for a fast ascent. Interestingly, the optimiser did adjust the trajectory starting date from the initial guess derived from STK, which has the effect of adjusting the phase between the spacecraft and the Moon.

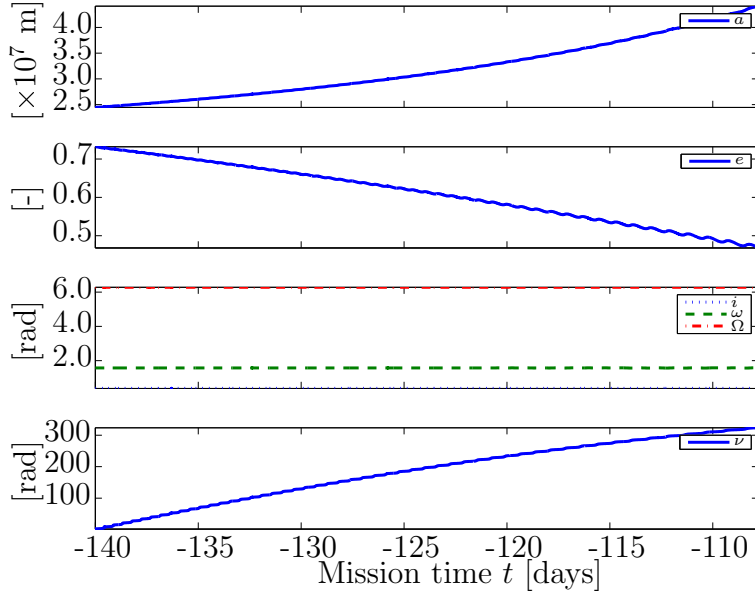


Figure 9.13: Keplerian elements of satellite within ECI frame during ascent phase.

This shows that even the relatively weak lunar gravity present during this phase may still be exploited. The orders of magnitude between the forces shown in Figure 9.14a and the gravitational forces due to Jupiter, Venus and Mars in Figure 9.14b highlight the reason why so many earlier studies neglect these forces.

The spacecraft periapsis is shown again in Figure 9.15. The profile is very similar to that observed in the reduced complexity ascent, although by thrusting through the periapsis the growth is smoothed somewhat. As this is the termination condition for the phase, the final periapsis is the same between the fully optimised reduced complexity version and this one. However, the optimised phase traded off semimajor axis (and thus orbital energy) to reduce the eccentricity faster.

The nearly constant thrust results in fuel consumption being almost linear with time. This can be seen in Figure 9.16, which plots the wet mass of the spacecraft over the phase. From the plot, this simulation suggested 59.82 kg worth of ammonia would be required for the ascent

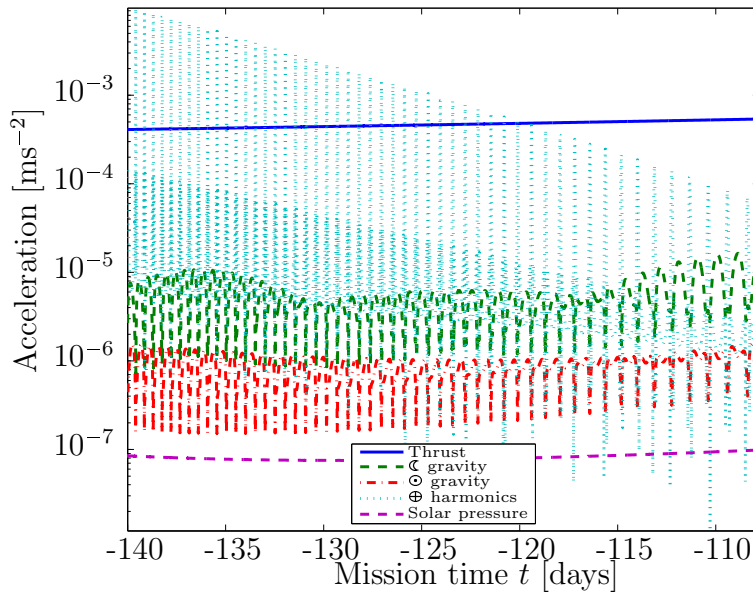


Figure 9.14a: Perturbing accelerations acting on spacecraft during ascent phase.

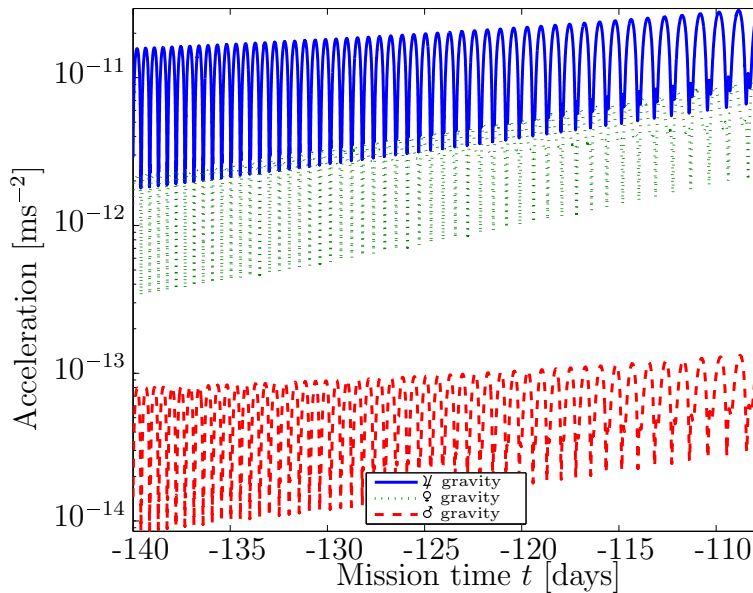


Figure 9.14b: Smaller magnitude perturbing accelerations acting on spacecraft during ascent phase.

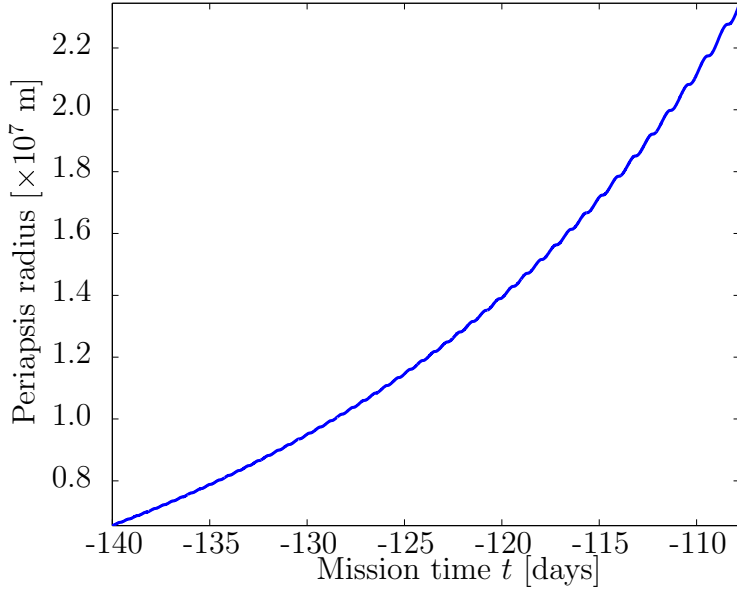


Figure 9.15: *Periapsis of spacecraft during ascent phase.*

phase. Since the reduced complexity ascent, which was allowed to reach an optimal solution, took 2 days longer but saved 6 kg of ammonia propellant, a similar solution may be expected from this higher fidelity model given adequate computational power. Whether this trade off is desired is an operational decision, requiring a detailed model of solar panel degradation within the van Allen belts.

Figure 9.17 shows the power generated and consumed during the ascent phase. The energy required for the thruster demonstrates the same linear behaviour as the first half of the reduced complexity simulation, continued for the whole phase as the optimisation was not allowed to proceed to the intermittent thrust profile as the reduced complexity simulation. However, the solar panels show a much higher power generation: 1140 kWh in 32.22 days, compared to 787 kWh in 34.17 days for the reduced complexity model. Given that the inclination, argument of periapsis and right ascension of the ascending node are identical to the reduced complexity ascent, and the trajectory is also very similar, there are few factors that could account for this difference. The biggest difference between the two

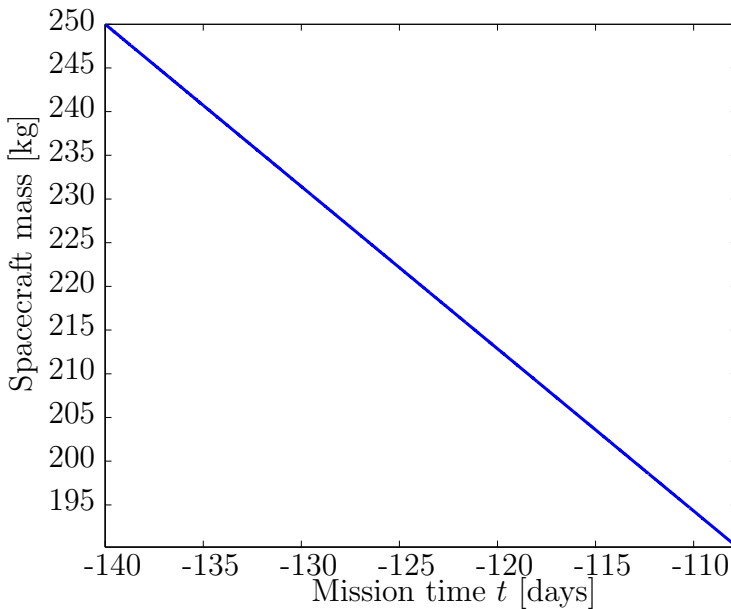


Figure 9.16: Mass of spacecraft during ascent phase.

simulations is the starting date: the reduced complexity phase started at the mission epoch, 1 January 2014. This simulation, based on the backwards propagated STK simulation, starts at epoch minus 140 days. In other words, due to the dependency on later phases in the STK simulation this GESOP simulation starts about 4.6 months earlier than the reduced complexity one, resulting in the sun subtending a very different angle on the Earth relative to the vernal equinox. Given the constraints on pointing the solar panels towards the sun (see Section 7.3) this must have an affect on power generation. Since power generation has been greater than power consumption in both GEOSP simulations, it does not affect the optimal trajectory, but is a factor worth investigating if more power is directed to the thrusters for a quicker ascent, as recommended in Section 10.2.

A total Δv of 1304 ms^{-1} was expended over the ascent phase, at an almost constant rate due to the linear thrust profile. This is rather more than the reduced complexity phase, and the Δv estimation in the original mission architecture. However, as mentioned previously this sub-optimal trajectory results in a higher orbital energy than the optimised reduced

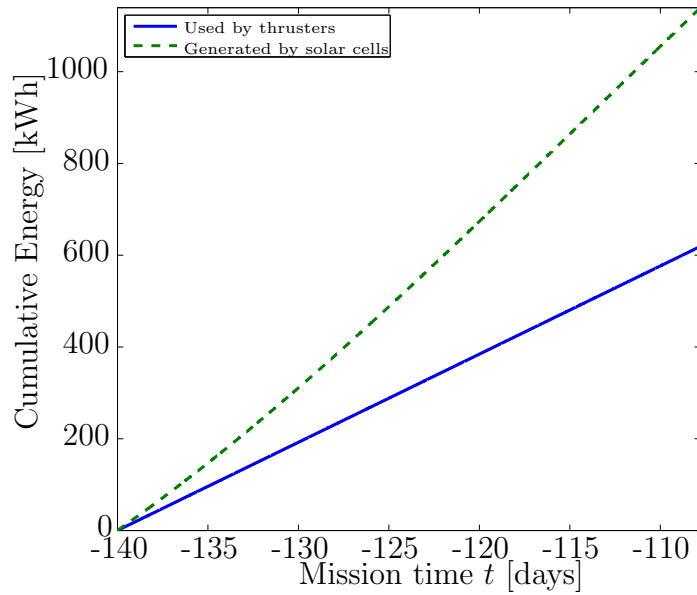


Figure 9.17: Power budget of spacecraft during ascent phase.

complexity phase, which would decrease time and propellant needed for the subsequent cruise phase.

9.4 Cruise phase

As seen in the 3 dimensional trajectory plotted in Figure 9.18, continual thrust during the cruise phase leads to a circular orbit, even from the fairly elliptical starting orbit. Consequently a rendezvous with the Moon cannot really be scheduled as in previous studies involving short, higher thrust periods interspersed with coasting. Rather, lunar resonances will happen inevitably, as the spacecraft passes the Moon in its lower, faster orbit. The purpose of the optimisation therefore is to schedule the effects of these resonances, by changing the inclination or eccentricity of the spacecraft's orbit. Little manipulation is required to achieve this, because all orbital changes are implicitly included in the optimisation. Of particular interest are the outermost orbits seen in the figure, whereupon the perigee is lowered (the eccentricity is increased) by a lunar assist.

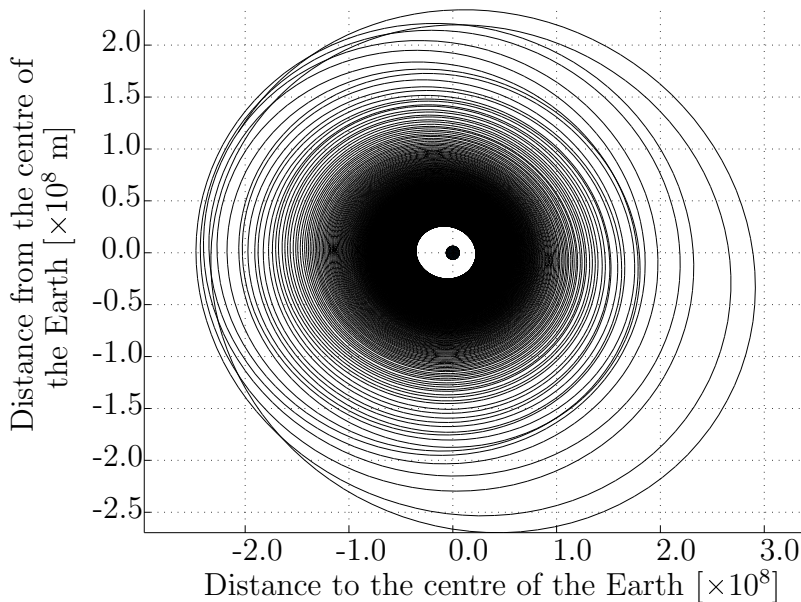


Figure 9.18: *Cruise trajectory of the satellite in ECI frame viewed from north pole.*

Figure 9.19 shows the distance of the spacecraft from the Earth and the Moon over the course of the cruise phase. In comparison to the ascent

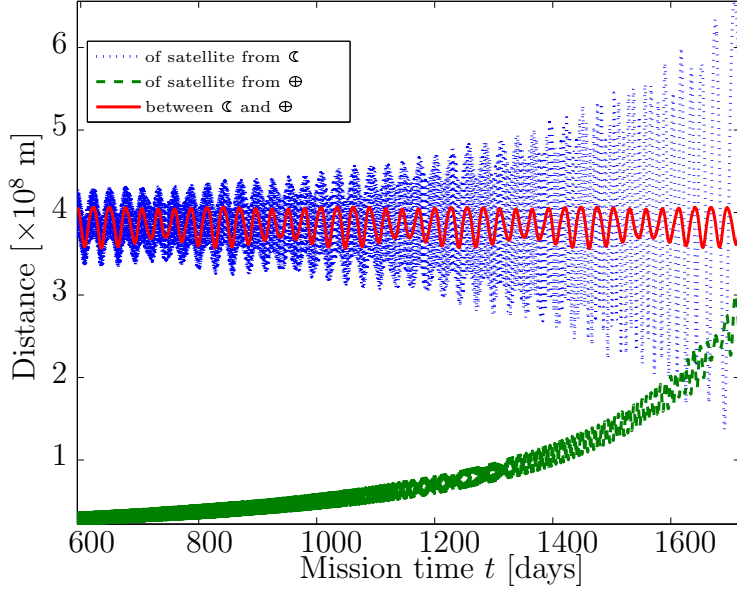


Figure 9.19: Satellite's distance from Earth and Moon during cruise phase.

phase, the spacecraft's greater distance from the Earth is apparent, resulting in greater oscillations in its distance from the Moon. The corresponding plot of orbital energies in Figure 9.20a, however, displays a decreasing oscillation in the spacecraft's orbital energy relative to the Moon, even as the minimum within the oscillation slowly approaches capture ($\epsilon_{\mathfrak{C}} \leq 0$). Meanwhile the orbital energy relative to the Earth approaches escape ($\epsilon_{\Theta} \geq 0$).

A closer inspection of the orbital energy relative to the Earth towards the end of the cruise phase, shown in Figure 9.20b, reveals a number of small gravitational assists, as the spacecraft approaches the lunar anomaly each orbit. This is then followed by a small gravitational penalty as the spacecraft continues away from the Moon. A similar, albeit smaller, assist is demonstrated every time the spacecraft is exactly opposite the Moon.

The thrust profile shown in Figure 9.21 resulted from the incomplete optimisation attempted on this phase. The noise in the out-of-plane component results from truncation error when evaluating the unit thrust vector constraint. Despite the optimisation not having been allowed to reach an

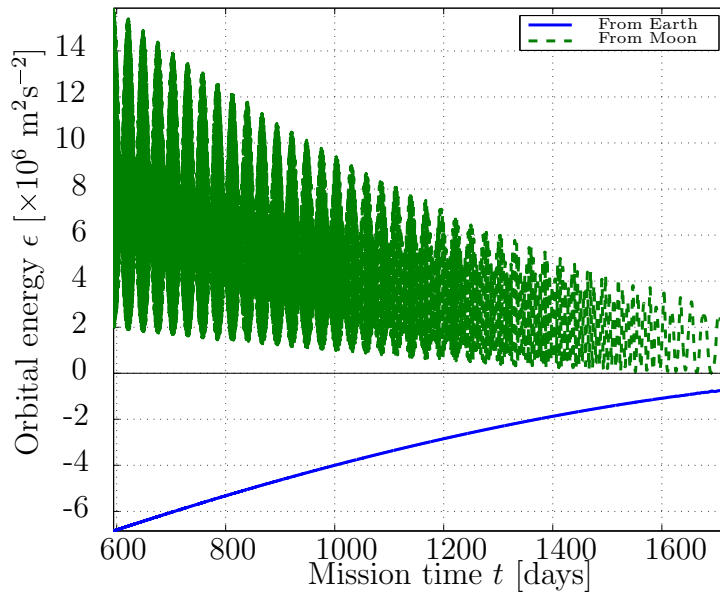


Figure 9.20a: Orbital energy of the satellite relative to Earth and Moon during cruise phase.

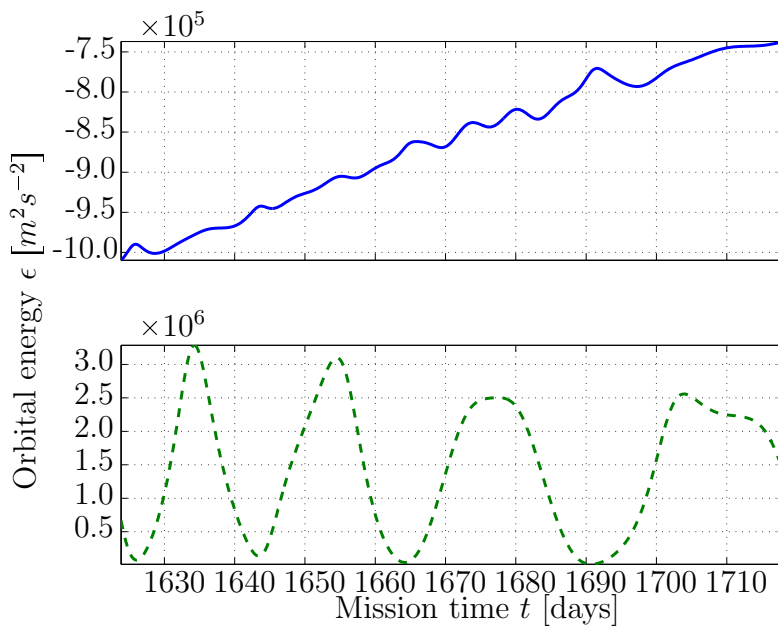


Figure 9.20b: Orbital energy of the satellite relative to Earth and Moon during cruise phase (zoomed in).

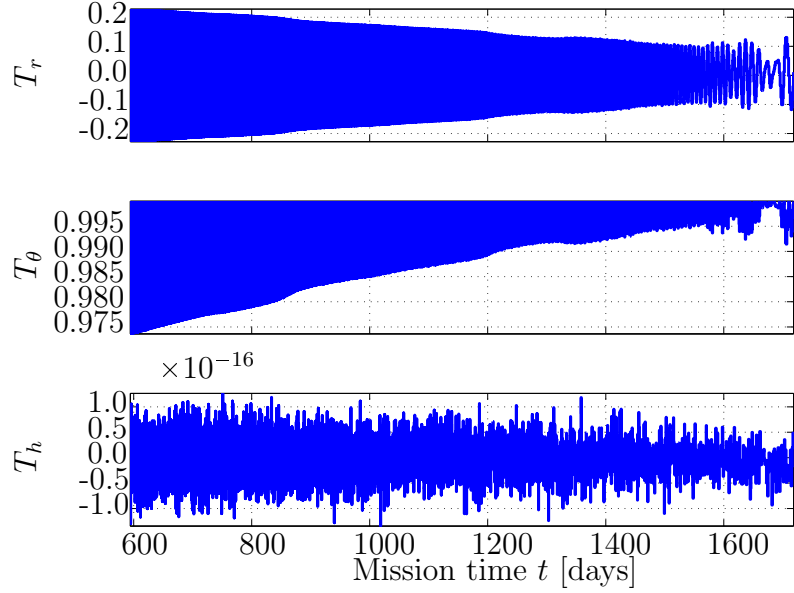


Figure 9.21: Direction of thrust vector during cruise phase.

optimal solution, it is apparent that the thrust profile is once again displaying the characteristics outlined in Section 9.2, by oscillating the thrust vector over the orbital period. It is interesting to note that the deviations from purely tangential thrust seem to be directly proportional to the eccentricity, shown in Figure 9.22, suggesting that the thrust profile is trying to circularise the orbit. Otherwise, the semimajor axis and anomaly are increasing similarly to the ascent phase. Figure 9.23 shows the corresponding equinoctial elements.

The perturbations shown in Figure 9.24a show the spacecraft thrust has dropped by two orders of magnitude, since it is now using the PPTs rather than the arcjet from the ascent phase. At the start of the cruise phase, the Earth's oblateness is still the strongest secondary force acting on the spacecraft, but this rapidly drops off as the spacecraft raises its orbit. The Moon's gravity becomes more dominant towards the end of the phase, with spikes starting to occur indicating gravitational assists caused by close passes to the Moon in the last few orbits. The sun's gravity also has a more significant effect on the spacecraft as its orbit is raised,

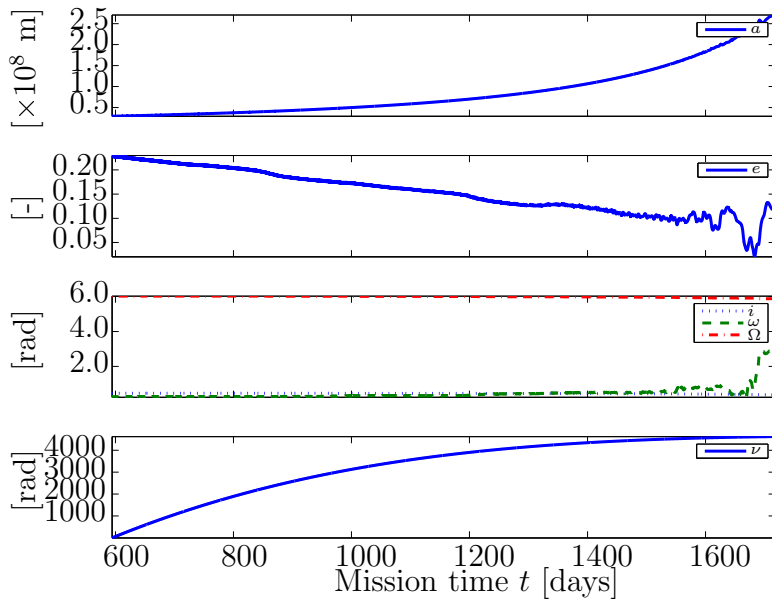


Figure 9.22: Keplerian elements of satellite within ECI frame during cruise phase.

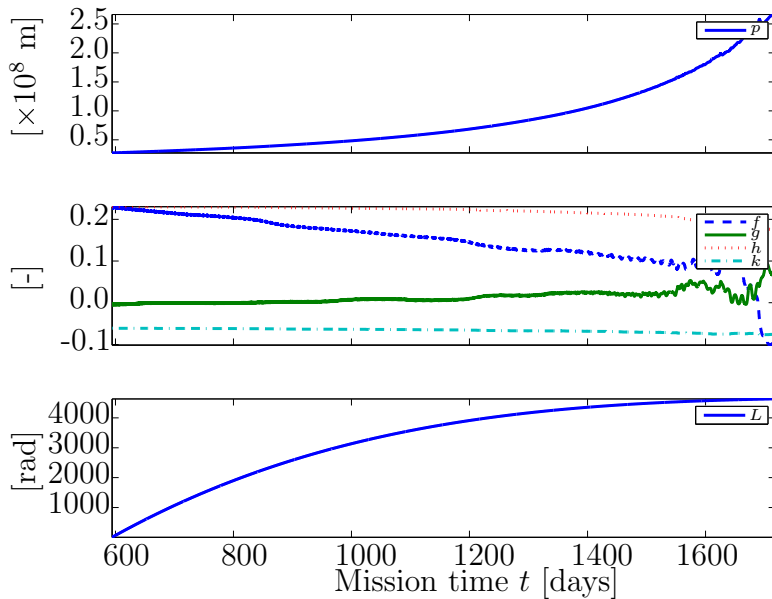


Figure 9.23: Equinoctial elements of satellite within ECI frame during cruise phase.

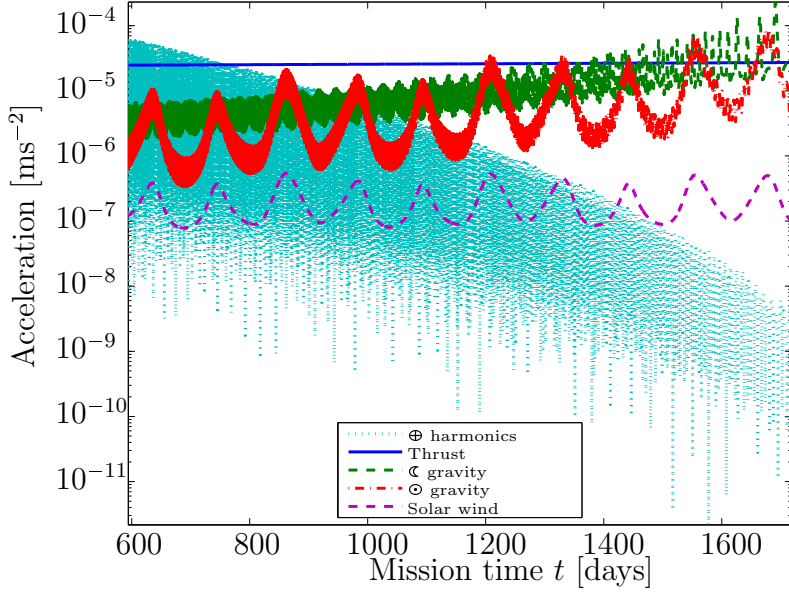


Figure 9.24a: Perturbing accelerations acting on spacecraft during cruise phase.

exhibiting high frequency oscillations due to the spacecraft's orbit around the Earth, and lower frequency oscillations closely following the averaged force due to solar wind, both due to the Earth's elliptical orbit around the sun. Similar cyclical behaviour is visible in Figure 9.24b, showing the resonances of Earth's orbit with Jupiter, Venus and Mars' orbits.

Throughout the cruise phase, 17.55 kg of PTFE was consumed, generating 2519 ms^{-1} of Δv . While this comprehensively demonstrates the efficacy of the PPTs compared to the arcjet used in the previous phase, the Δv requirement was still much higher than that anticipated in the original mission architecture of 1.6 kms^{-1} . Given the theoretical optimality of tangential thrust, and how closely the other phases lined up with anticipated delta-v expenditure, such a large discrepancy may be due to a calculation error or invalid assumption during mission planning.

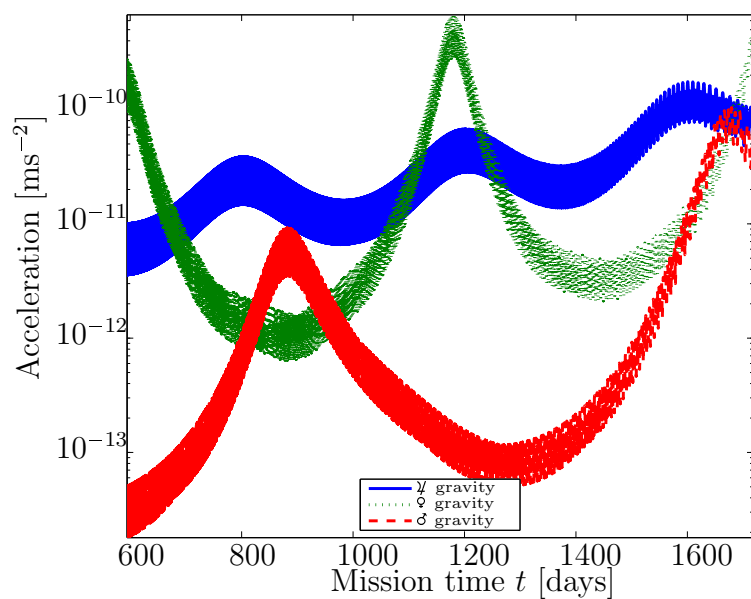


Figure 9.24b: Smaller magnitude perturbing accelerations acting on spacecraft during cruise phase.

9.5 Propagate phase

Figure 9.25 shows the simulated coasting trajectory during the propagate phase. This consists of 1.5 orbits around the Earth followed by an lunar rendezvous that pulls the spacecraft into the desired lunar orbit. This orbit is apparent in Figure 9.26 which plots the same trajectory but from a lunar centred frame. Since the spacecraft enters a polar orbit about the Moon, it appears to intersect the Moon given the camera is positioned above the Moon's pole. Figure 9.27 shows the trajectory from the selenocentric frame, fixed relative to the Moon's surface. Because the Moon is tidally locked to the Earth, the Earth appears to be in a halo orbit in this frame.

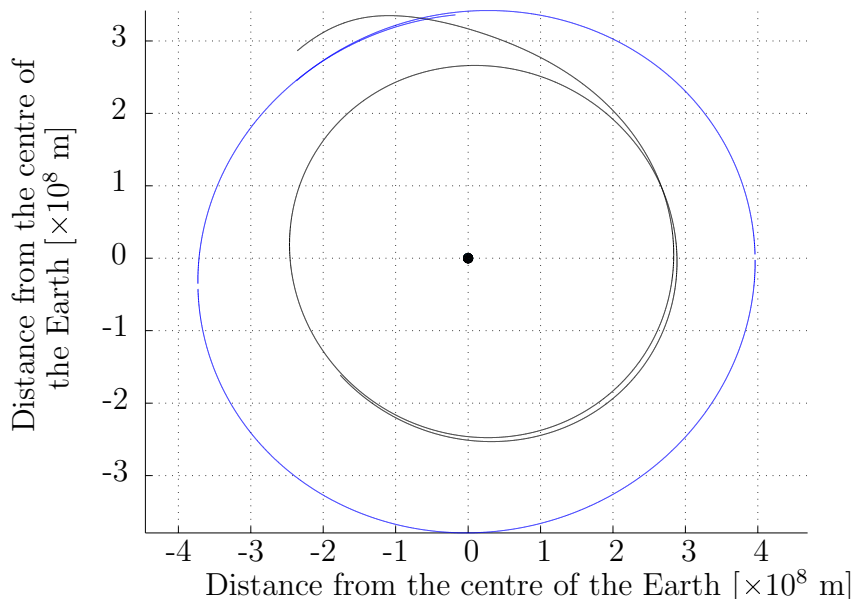


Figure 9.25: *Propagated trajectory of the satellite in ECI frame viewed from north pole. The Moon's orbit is shown in blue.*

The spacecraft's distances from the Earth and the Moon are shown in Figure 9.28. It starts on the opposite side of the Earth from the Moon, then gets pulled into lunar orbit as it swings around the Earth. Figure 9.29 shows the corresponding orbital energies. The spacecraft has a very high orbital energy relative to the Moon whilst it is on the far side of the Earth,

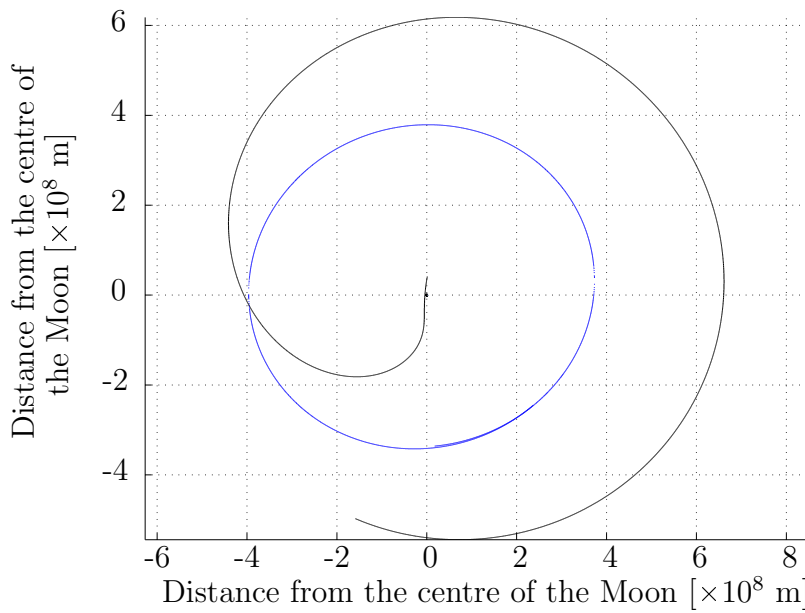


Figure 9.26: Propagated trajectory of the satellite in LCI frame viewed from north pole. The Earth's orbit is shown in blue.

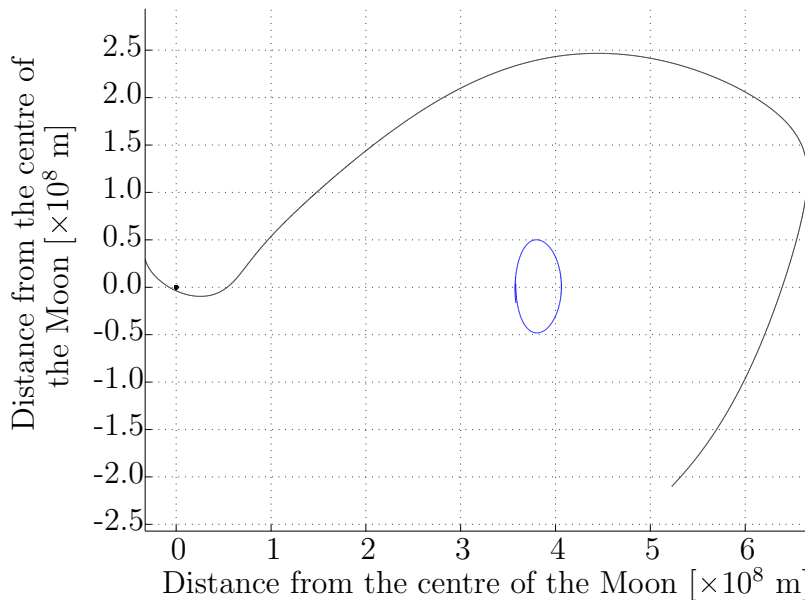


Figure 9.27: Propagated trajectory of the satellite in SEL frame viewed from north pole. The Earth's orbit is shown in blue.

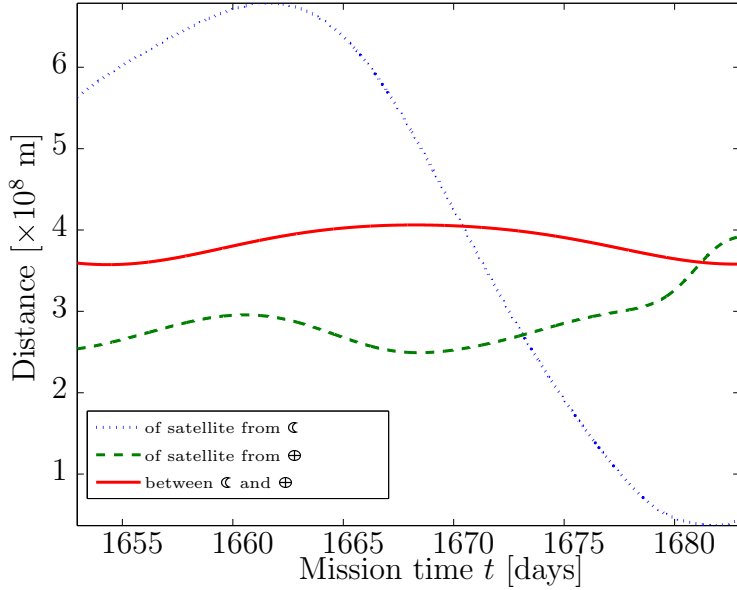


Figure 9.28: Satellite's distance from Earth and Moon during propagate phase.

before being captured (dropping below $\epsilon_{\mathbb{C}} = 0$) towards the end of the phase. Throughout the phase the orbital energy relative to the Earth is very close to that of the Moon.

The Keplerian elements shown in Figure 9.30 show a sudden jump in semimajor axis and eccentricity as the spacecraft gets pulled towards the Moon, then another increase in semimajor axis accompanied by a drop in eccentricity as the spacecraft gets pulled into lunar orbit. The spacecraft remains at the same inclination as the Moon, but the right ascension of the ascending node (Ω) is changed as the orbital plane is rotated around Earth's pole to match that of the Moon. As the spacecraft is pulled into lunar orbit, the anomaly becomes cyclical with respect to the Earth, highlighting why a lunar-centric frame is necessary for the subsequent phases, and why this phase was modelled with time as the independent parameter instead of longitude, as outlined in Section 8.2.4. Figure 9.31 again shows the corresponding equinoctial elements.

Seen relative to the lunar frame in Figure 9.32, the semimajor axis

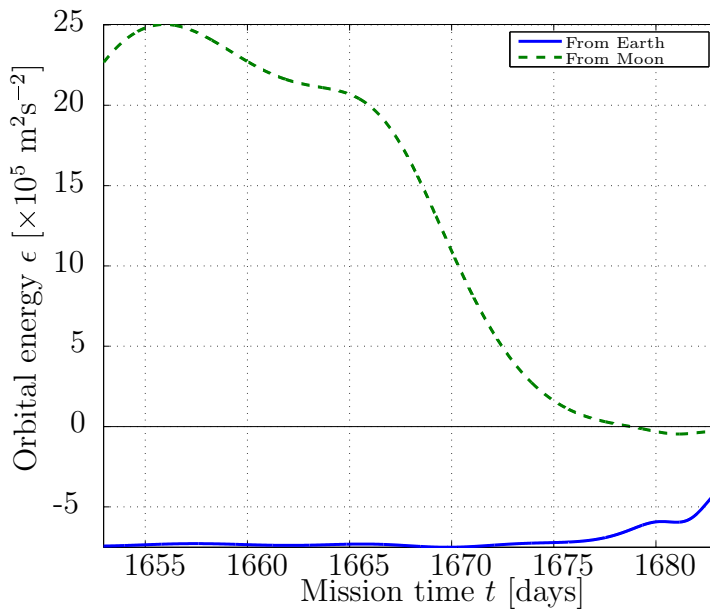


Figure 9.29: Orbital energy of the satellite relative to Earth and Moon during propagate phase.

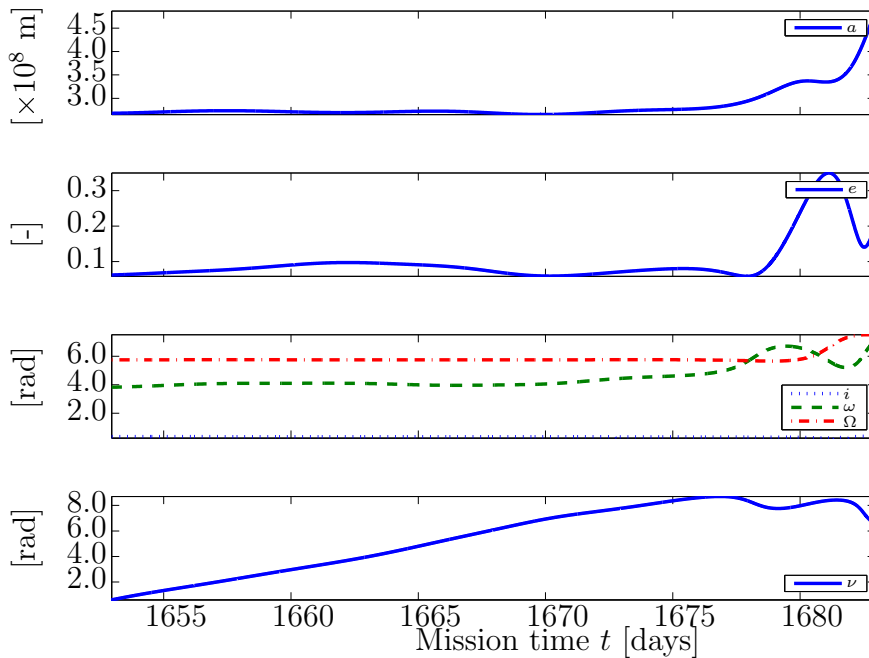


Figure 9.30: Keplerian elements of satellite within ECI frame during propagate phase.

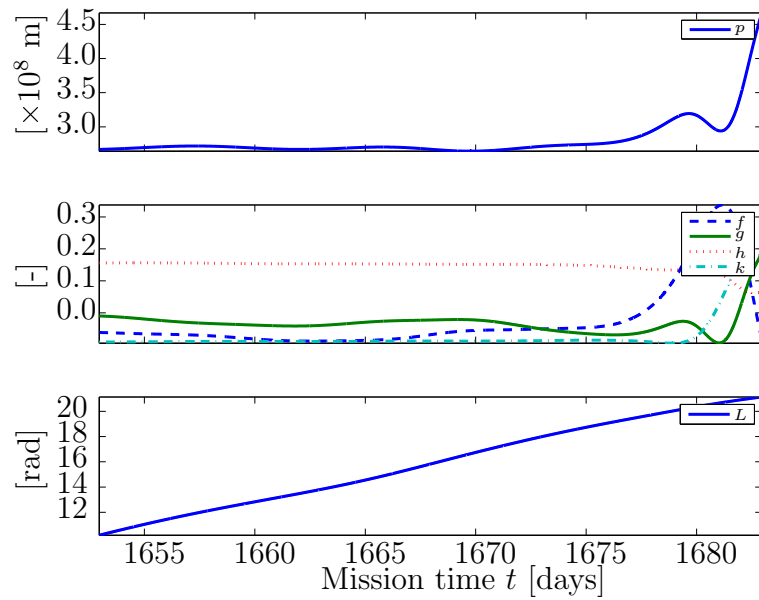


Figure 9.31: Equinoctial elements of satellite within ECI frame during propagate phase.

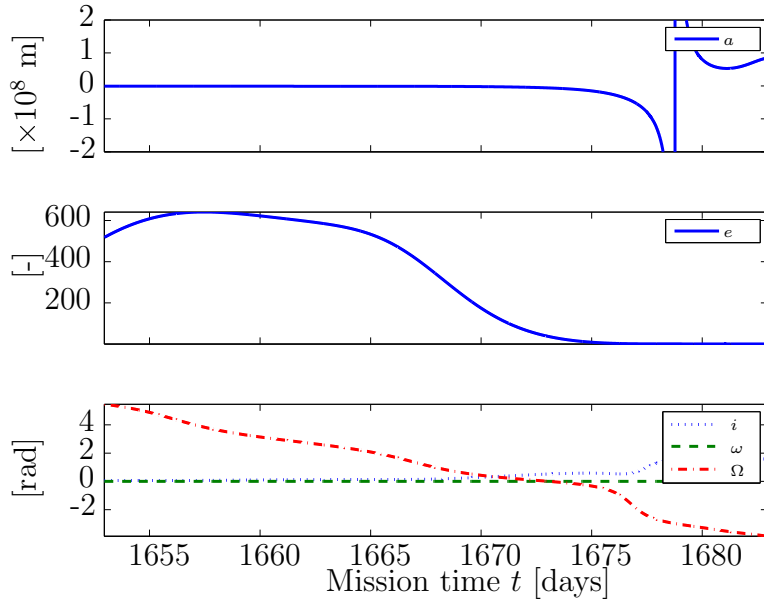


Figure 9.32: Keplerian elements of satellite within LCI frame during propagate phase.

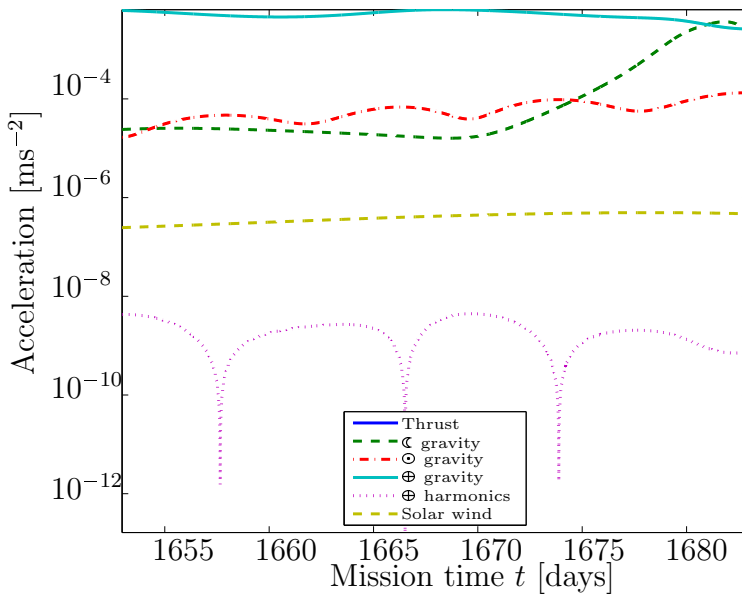


Figure 9.33: Perturbing accelerations acting on spacecraft during propagate phase.

approaches negative infinity as the spacecraft approaches capture, while the eccentricity approaches 1. At the point of capture, the spacecraft is in a parabolic orbit and the semimajor axis is undefined. As the spacecraft then descends into lunar orbit, the semimajor axis drops down from positive infinity.

The perturbing forces in Figure 9.33 continue on from the previous phase (Figure 9.24a), with solar and lunar gravity dominant, although there is no thrust present during this phase. As the spacecraft descends into lunar orbit, unsurprisingly the lunar gravity becomes the dominant force. Another interesting point is the cyclical nature of the force due to Earth's oblateness that is highlighted in this plot. The sudden drops are caused when the spacecraft passes the Earth's equator, and the J_2 harmonic no longer has any effect on the vehicle. Furthermore, the alternating short-long-short duration between these drops is caused by the short periapsis half of the orbit, followed by the lengthy apoapsis.

A factor that becomes important as the spacecraft approaches capture

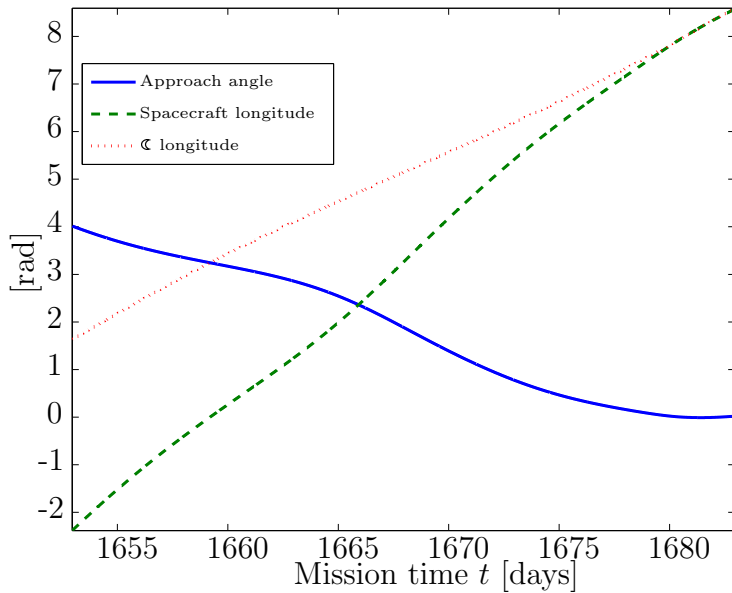


Figure 9.34: Longitude of spacecraft and Moon during propagate phase. The approach angle is the difference between spacecraft longitude and the Moon's longitude.

is the angle subtended between the craft and the Moon, relative to the Earth. This is shown in Figure 9.34. At the start of the phase, the Moon is close to its ascending node, with the spacecraft leading it by about 2 radians. As the spacecraft is in a lower, faster orbit, this angle widens until 1660 days at which point the spacecraft and the Moon are on opposite sides of the Earth. The subtended angle then approaches zero as the spacecraft approaches lunar orbit.

9.6 Capture phase

Following the weak capture during the coasting phase propagated by the simulator the arcjet is again used, this time to lower the orbit as quickly as possible to avoid being recaptured by the Earth. This results in the spacecraft mapping increasingly small and fast circles around the Moon, as shown from the Earth's perspective in Figure 9.35.

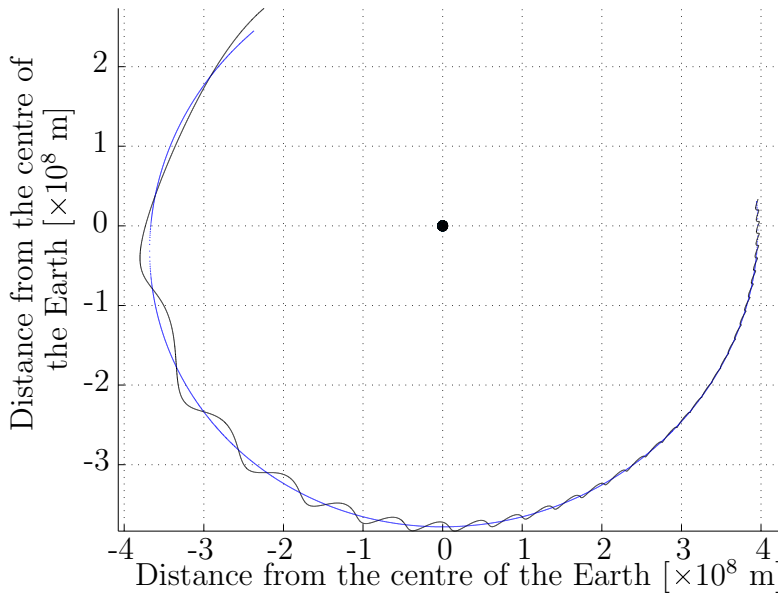


Figure 9.35: Capture trajectory of the satellite in ECI frame viewed from north pole. The Moon's orbit is shown in blue.

The descending spiral trajectory is far more apparent from the lunar centred frame in Figure 9.36. When this frame is rotated in Figure 9.37 the lunar surface coverage can be seen, indicating that the science payload could be activated during this phase subject to sufficient power.

The satellite's distance from the respective bodies in Figure 9.38 is unsurprising; it gets closer to the Moon, while its orbit about the Moon causes oscillations in the distance to Earth that approach the Earth-Moon distance as the orbit descends. The orbital energy plot in Figure 9.39 is more interesting, showing the spacecraft's precariously captured lunar

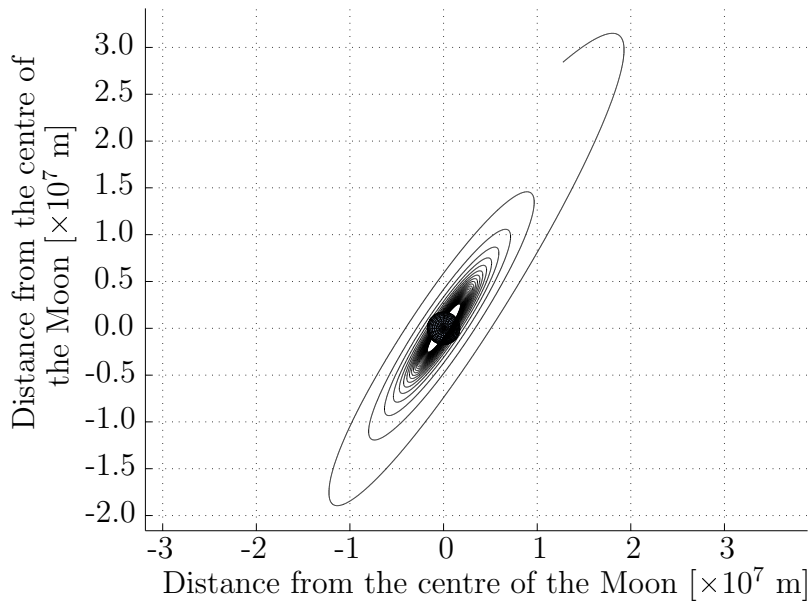


Figure 9.36: Capture trajectory of the satellite in LCI frame viewed from north pole.

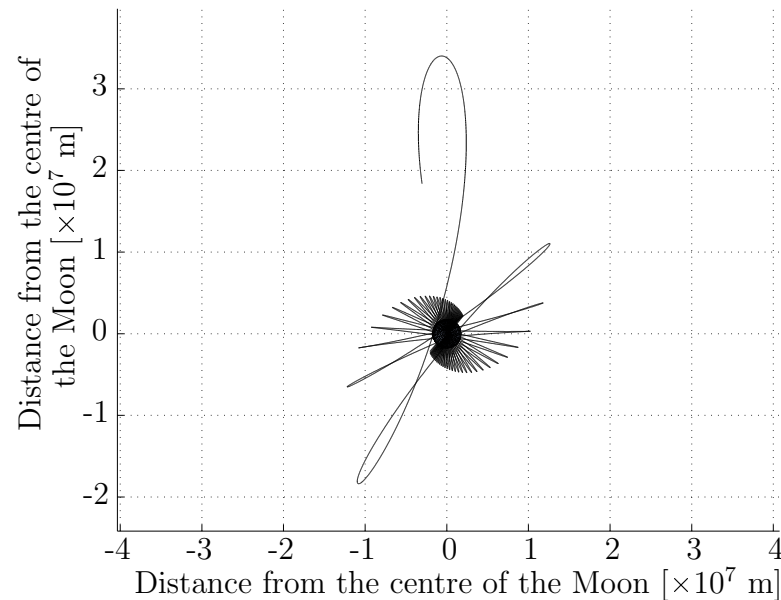


Figure 9.37: Capture trajectory of the satellite in SEL frame viewed from north pole.

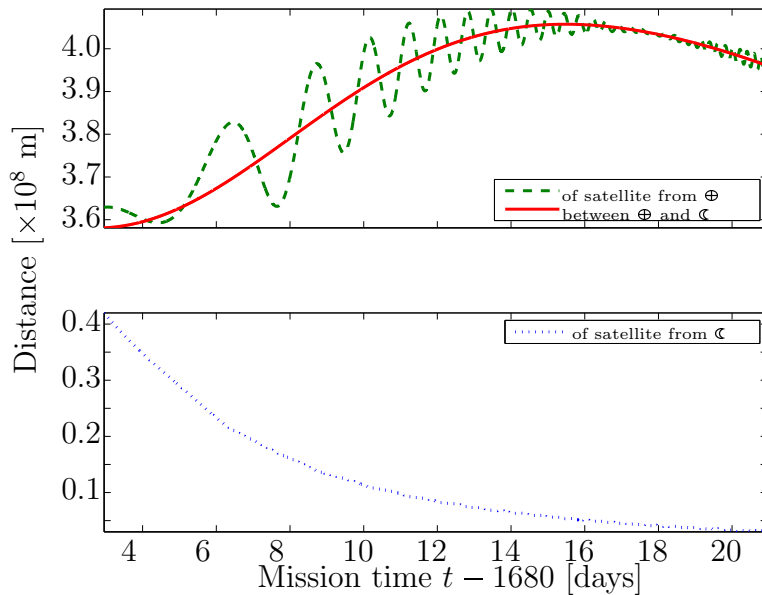


Figure 9.38: Satellite's distance from Earth and Moon during capture phase.

orbit becoming more stable. Meanwhile, the orbital energy with respect to the Earth starts oscillating wildly. The spacecraft's gravitational potential with respect to the Earth is more or less constant, so the oscillations are caused by the velocity vector oscillating towards and then away from the Earth. A consequence of this is that when the spacecraft's velocity is directed away from the Earth, it exceeds escape velocity, so the orbital energy is positive. If not for the Moon repeatedly pulling the spacecraft back again, it would escape the Earth's gravity field.

During the capture phase, the semimajor axis shown in Figure 9.40 steadily decreases very similar to the ascent phase in reverse. Similarly, the anomaly increases at an increasing rate, and the lower orbit results in higher orbital speed. Unlike a reversed descent phase, the eccentricity continues to decrease until it reaches a very nearly circular orbit, as required for the science phase. For the first half of the phase, the argument of periapsis is increasing while the anomaly is almost steady. This has essentially the same effect as the anomaly increasing, since the orbit is al-

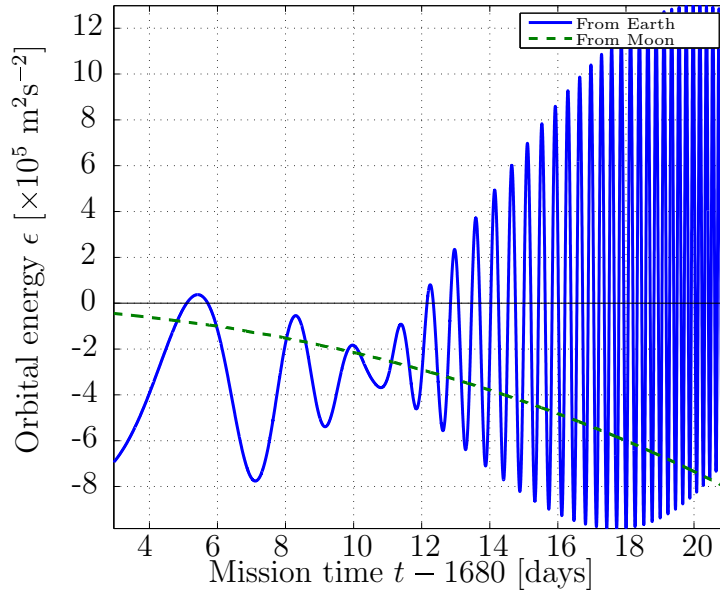


Figure 9.39: Orbital energy of the satellite relative to Earth and Moon during capture phase.

most circular. The right ascension of the ascending node precesses steadily as a result of the Earth's gravity, a well known phenomenon of polar lunar orbits (Gupta and Sharma 2011). The corresponding equinoctial elements are shown in Figure 9.41.

In the plot of perturbations acting on the spacecraft over the capture phase, shown in Figure 9.42a, the acceleration due to spacecraft thrust is observed to slowly increase. This is because propellant is expelled as the spacecraft thrusts, thereby reducing the mass being accelerated. This phenomenon is present in every powered phase, but is most apparent during the capture phase because the arcjet is in use, resulting in a higher mass flux than the descent phase, combined with the lighter load than previous phases because much of the fuel has already been used. The Earth's gravity continues to decrease in effect as the spacecraft settles to a steady distance from the Earth, but the perturbations due to the Moon's oblateness rapidly increase in magnitude. For completeness, the smaller perturbing forces are shown in Figure 9.42b.

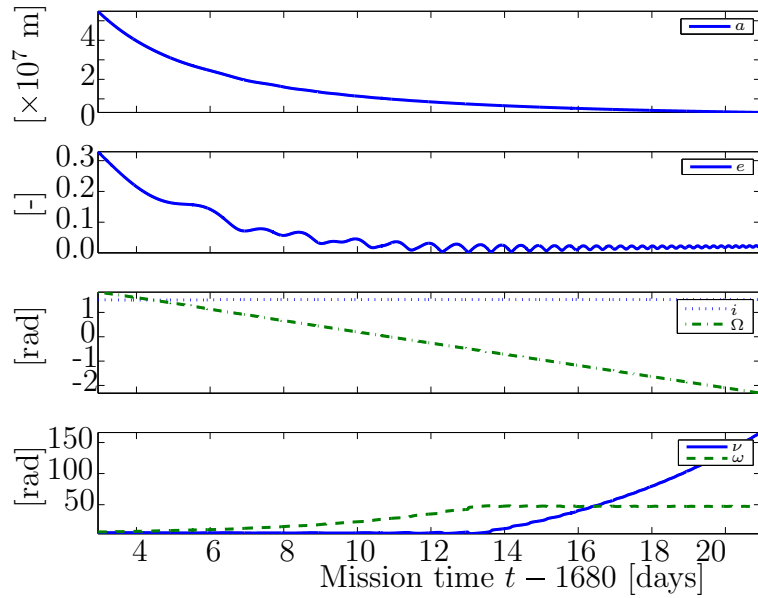


Figure 9.40: Keplerian elements of satellite within LCI frame during capture phase.

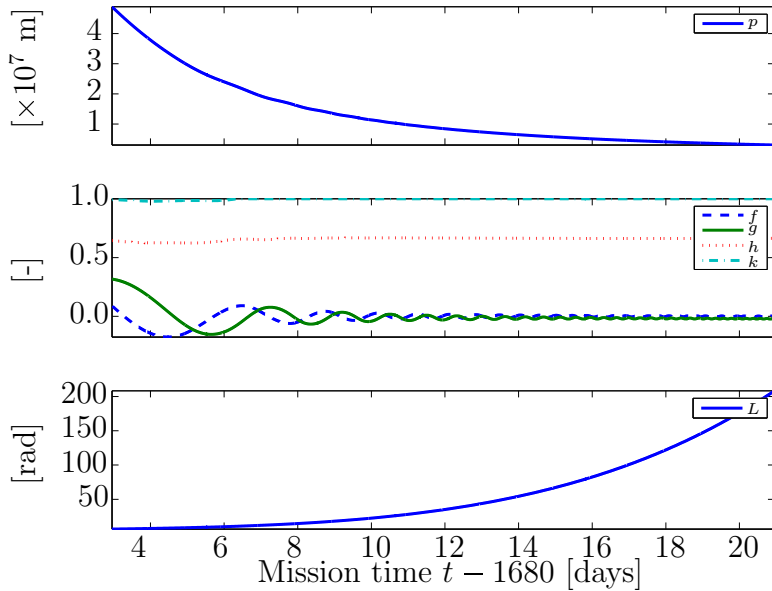


Figure 9.41: Equinoctial elements of satellite within LCI frame during capture phase.

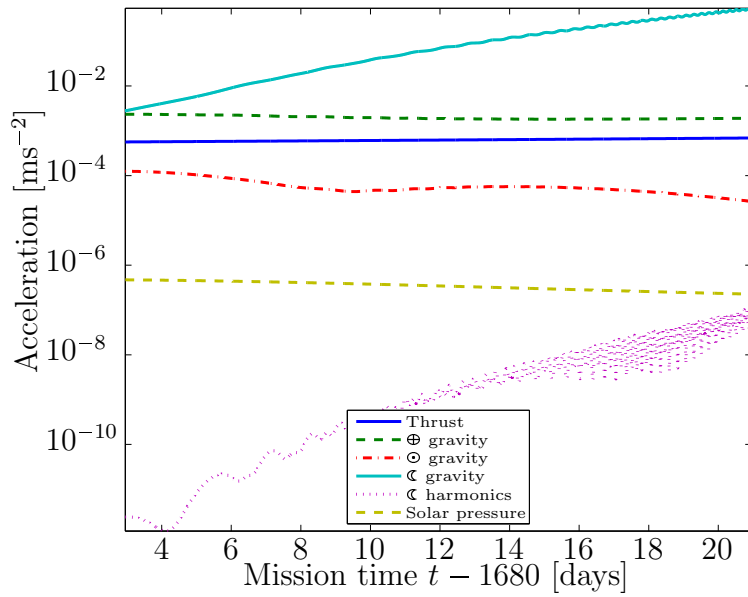


Figure 9.42a: Perturbing accelerations acting on spacecraft during capture phase.

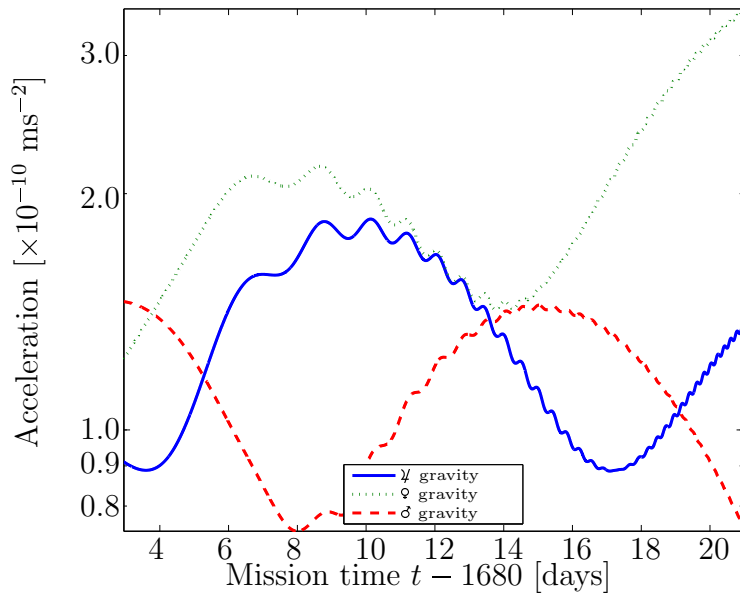


Figure 9.42b: Smaller magnitude perturbing accelerations acting on spacecraft during capture phase.

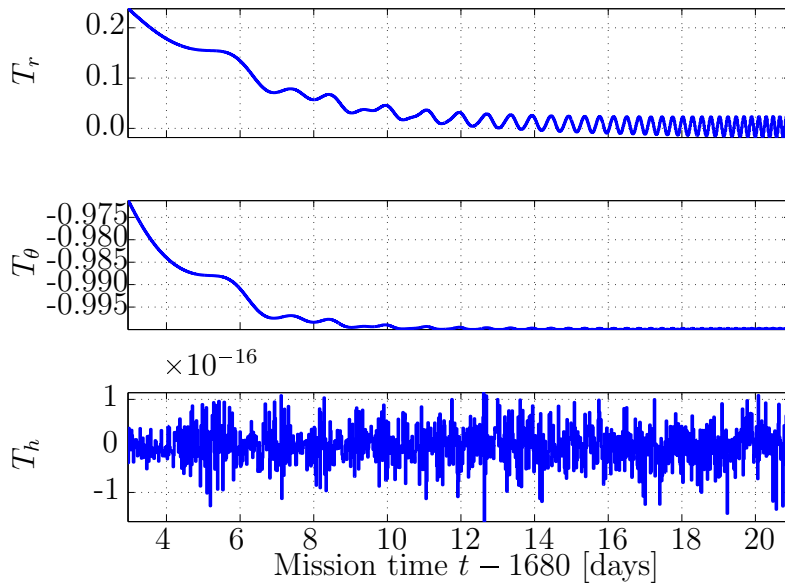


Figure 9.43: Direction of thrust vector during capture phase.

Figure 9.43 shows the thrust profile resulting from the capture phase simulation. This profile results from the initial guess, of continual thrust backwards along the velocity vector. Consequently the thrust initially has a substantial radial component due to the eccentricity of the orbit, but rapidly settles into almost purely tangential thrust. The noise in the out-of-plane component again results from truncation error when evaluating the unit thrust vector constraint.

Over the course of the capture phase, 33.43 kg of ammonia propellant was used. This generated almost 968 ms^{-1} of Δv , compared to the original mission architecture guess of 500 ms^{-1} . Once again this is a substantial difference that is unlikely to be accounted for by allowing the phase optimisation to reach an optimal solution. It is more likely that if the entire multiple-phase trajectory were optimised together, a substantial saving in Δv could be achieved (and correspondingly fuel consumption) particularly in the troublesome area of lunar capture, as the optimiser would be able to evaluate different capture scenarios. However, the original mission architecture estimates were based on a low-fidelity STK simulation, and did

not investigate complex lunar capture techniques. Consequently it must be concluded that the initial estimates were optimistic.

9.7 Descent phase

Figure 9.44 shows the descent phase trajectory in an inertial lunar centred frame. The terminal conditions of the capture phase are propagated to the science orbit using the PPTs. This results in the very tight, very nearly circular spiral seen in the figure. In the rotating surface-fixed frame of Figure 9.45, the slow decrease in orbital altitude can be seen.

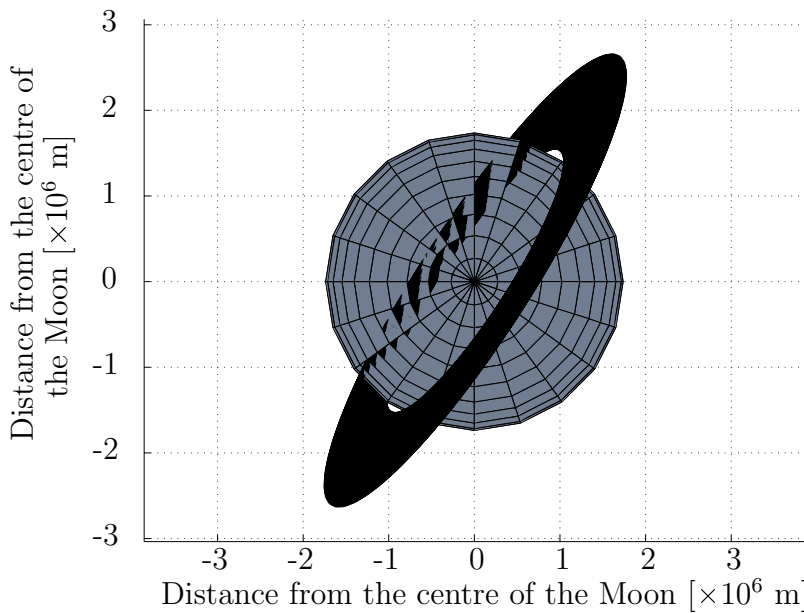


Figure 9.44: Descent trajectory of the satellite in LCI frame viewed from north pole. The orbits behind the Moon partly show through due to a flaw in the vector graphics renderer.

The spacecraft's distance from the Moon, shown in Figure 9.46, is almost trivial during this phase; the distance from the Moon decreases gradually, with a higher frequency oscillation due to the slightly eccentric orbit, while the distance from the Earth closely maps the distance of the Earth from the Moon.

The plot of orbital energy seen in Figure 9.47 shows a similar characteristic: the spacecraft's orbital energy relative to the Moon slowly decreases without any oscillation.

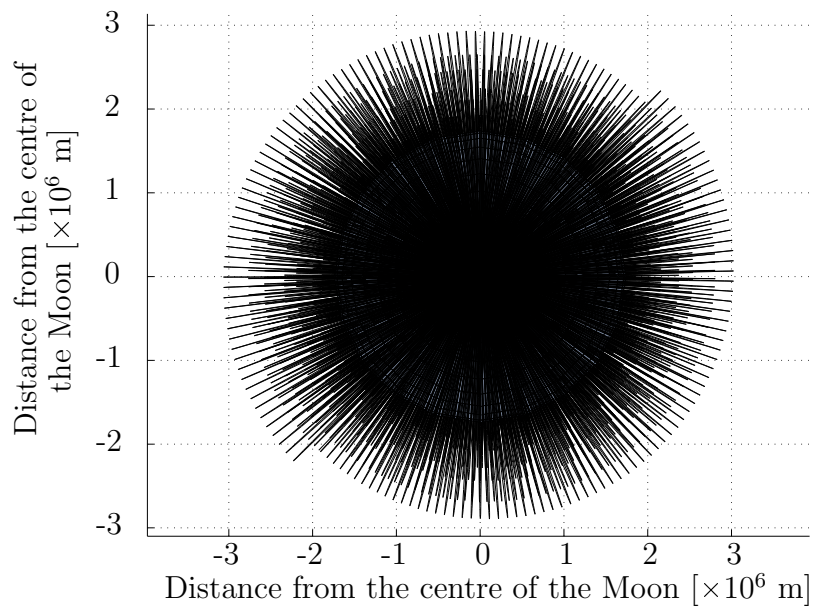


Figure 9.45: Descent trajectory of the satellite in SEL frame viewed from north pole.

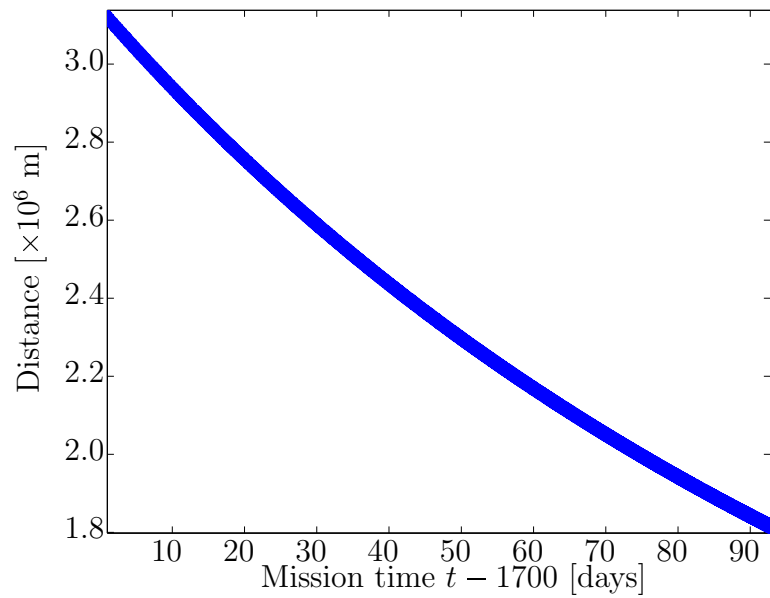


Figure 9.46: Satellite's distance from the Moon during descent phase.

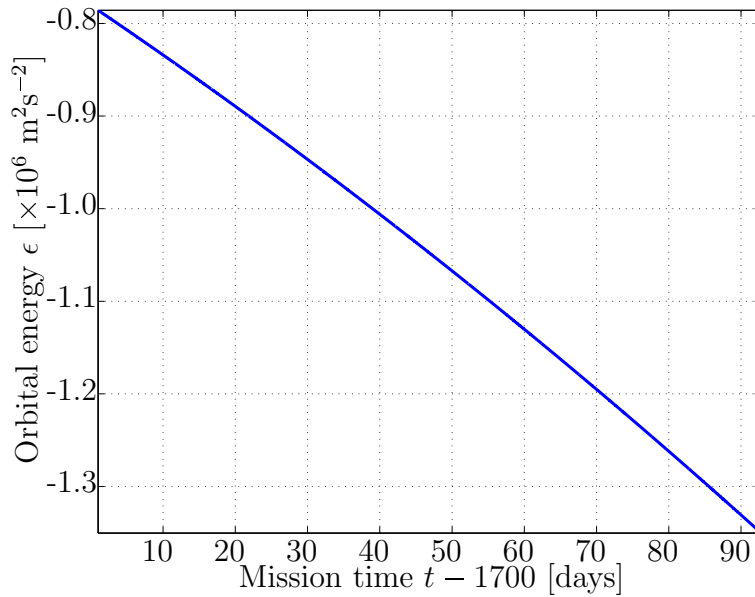


Figure 9.47: Orbital energy of the satellite relative to the Moon during descent phase.

Throughout the phase, the semimajor axis in Figure 9.48 steadily drops as desired, while the eccentricity has already started a small but inexorable increase due to the asymmetric lunar gravity field that will ultimately cause the spacecraft to crash into the surface. The right ascension continues to precess. The corresponding equinoctial elements are shown in Figure 9.49.

In the plots of perturbing forces acting on the spacecraft during the descent phase (Figure 9.50a and Figure 9.50b), the Earth's orbit about the Sun is once again apparent in the solar gravity and solar wind. Forces due to the Moon's gravitational harmonics are increasing in strength as the craft gets closer to the surface, but the dominant secondary force is still Earth's gravity.

The thrust throughout the descent phase is directed backwards along the velocity vector, as seen in Figure 9.51. Since the orbit is very nearly circular, this thrust is primarily tangential to the circle being described, with very small radial components. Once again the out-of-plane thrust is a negligible truncation error.

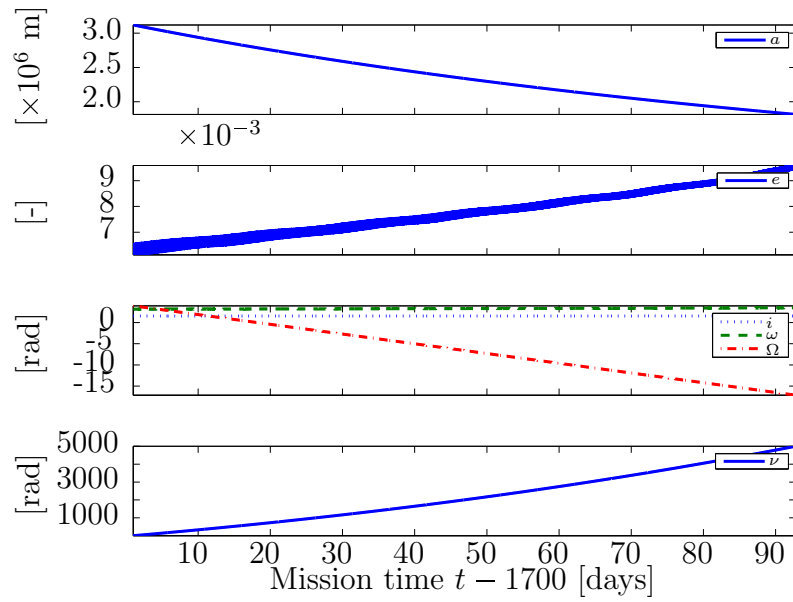


Figure 9.48: Keplerian elements of satellite within LCI frame during descent phase.

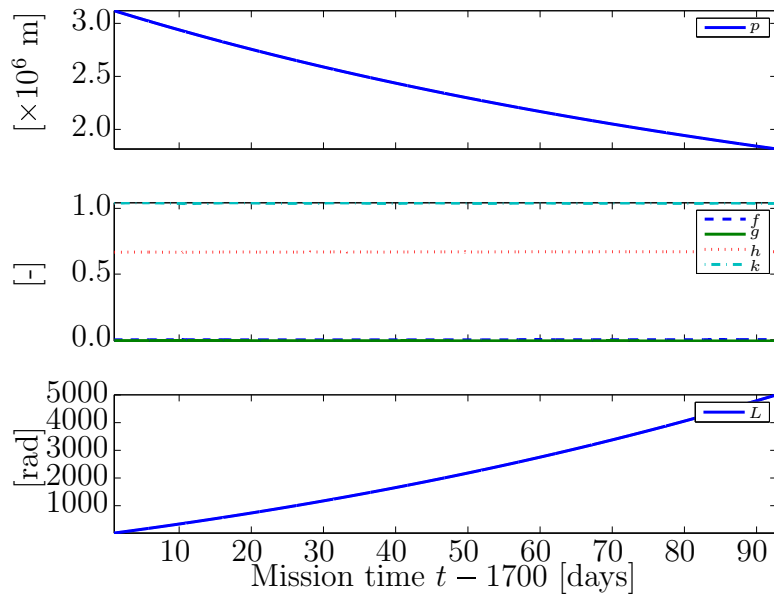


Figure 9.49: Equinoctial elements of satellite within LCI frame during descent phase.

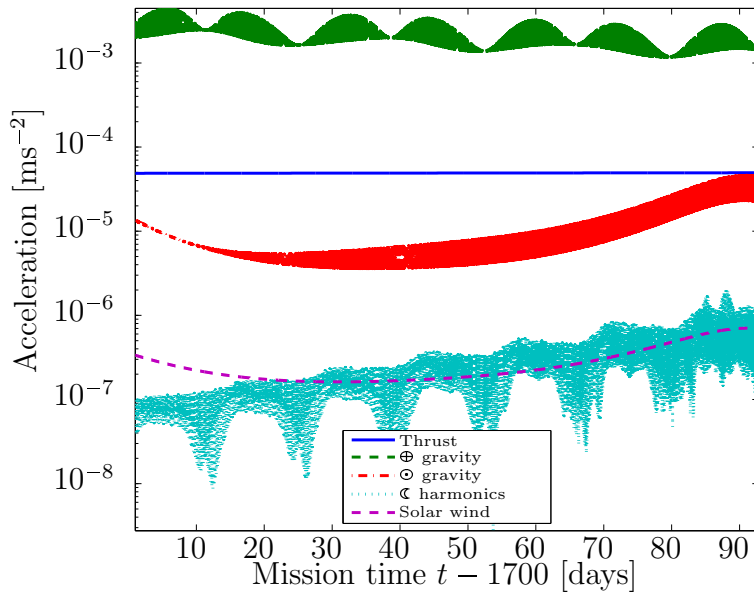


Figure 9.50a: Perturbing accelerations acting on spacecraft during descent phase.

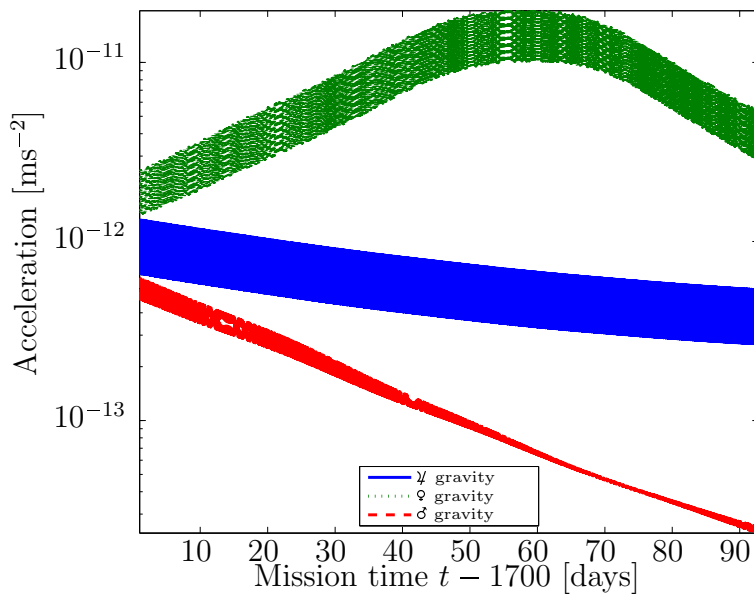


Figure 9.50b: Smaller magnitude perturbing accelerations acting on spacecraft during descent phase.

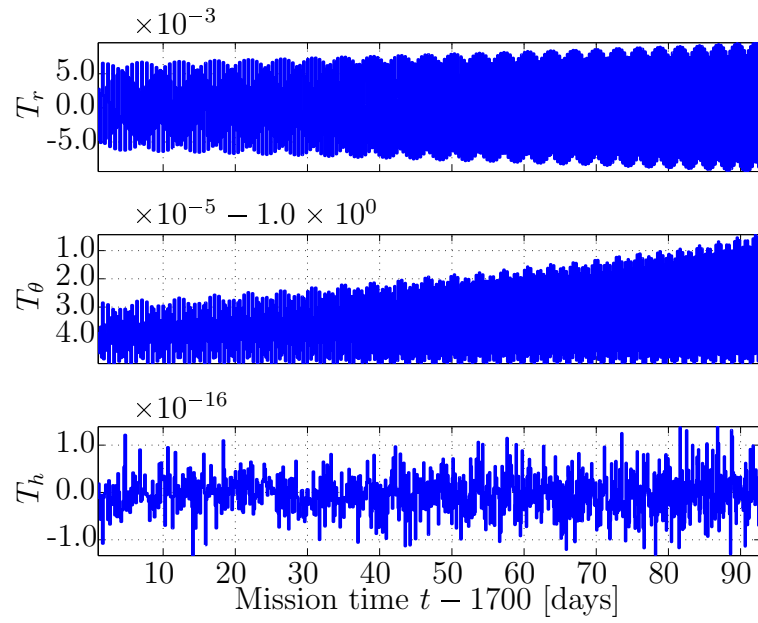


Figure 9.51: Direction of thrust vector during descent phase.

The simulation of this phase estimated 1.43 kg PTFE was consumed, providing almost 390 ms^{-1} . This Δv is almost exactly as estimated in the original mission architecture. Once again the PPTs are remarkably efficient for a phase that lasted 91.79 days. As with the cruise phase, there is a surplus of energy available, although the power generation slows late in the phase as the spacecraft begins transiting through the Moon's shadow.

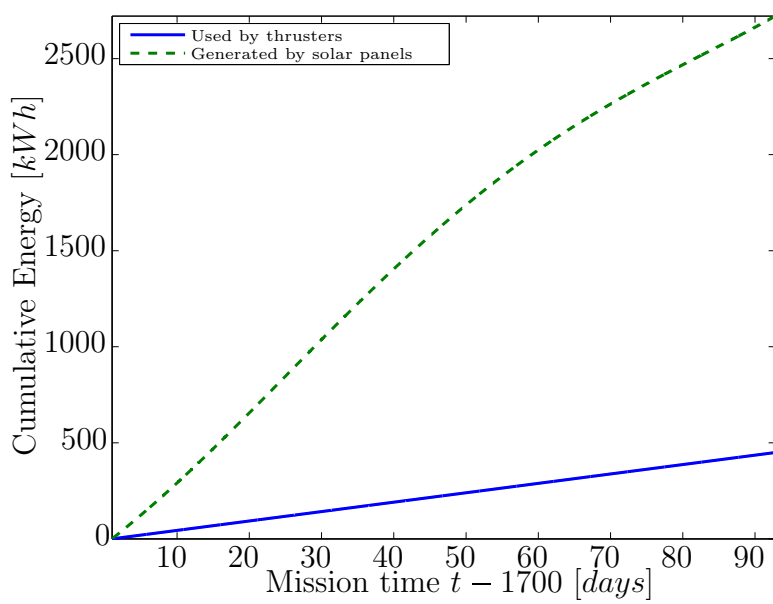


Figure 9.52: Power budget of spacecraft during descent phase.

9.8 Science phase

As there is no propulsive thrust during the science phase, the orbit was propagated forwards for 6 months to determine the spacecraft's behaviour in the absence of stationkeeping manoeuvres. Figure 9.53 shows the final orbit in an inertial frame.

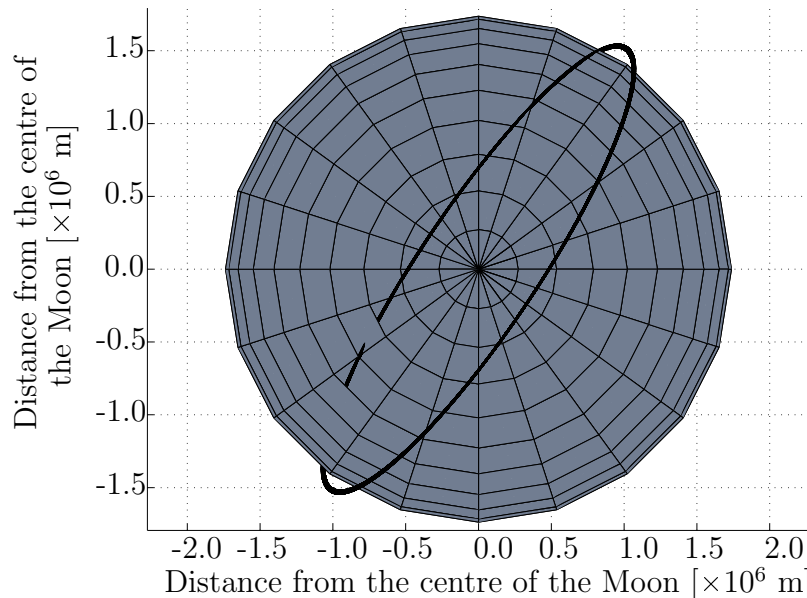


Figure 9.53: *Science trajectory of the satellite in LCI frame viewed from north pole. The orbits behind the Moon partly show through due to a flaw in the vector graphics renderer.*

The Keplerian elements shown in Figure 9.54 shows oscillations in the semimajor axis caused by the asymmetric lunar gravity field. More worryingly, the eccentricity shows a steady increase throughout the phase, indicating an increasingly elliptical orbit that would eventually cause the spacecraft to impact the Moon's surface. This trend is more visibly seen in Figure 9.55, showing the resulting decrease in periapsis radius. On the other hand, the sudden change in argument of periapsis (ω) towards the start of the phase merely represents the periapsis switching sides of the perfectly circular orbit. The right ascension of the ascending node continues to precess. These behaviours all resemble the 130 km lunar orbit modelled

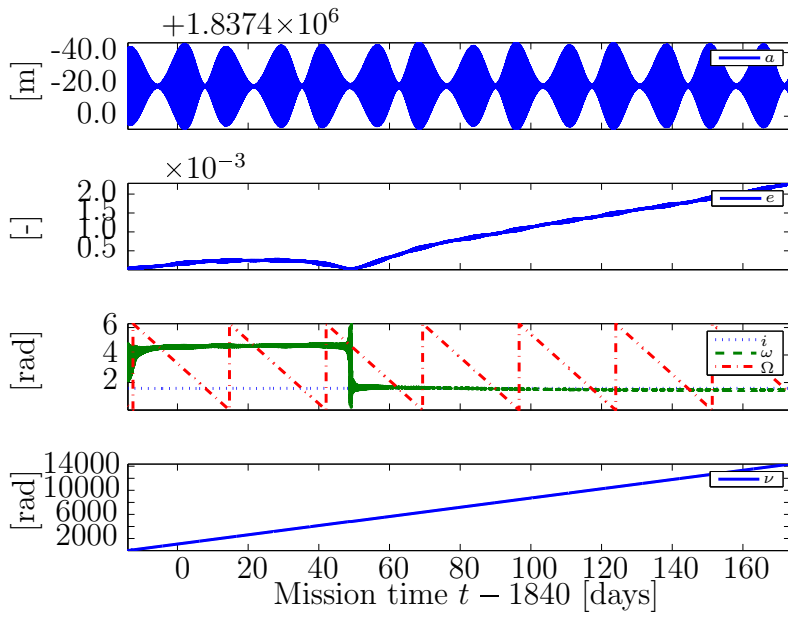


Figure 9.54: Keplerian elements of satellite within LCI frame during science phase.

by Gupta and Sharma (2011) in their analysis of lunar orbital lifetimes very closely. Once again the corresponding equinoctial elements are shown in Figure 9.56. The larger perturbing forces are shown in Figure 9.57.

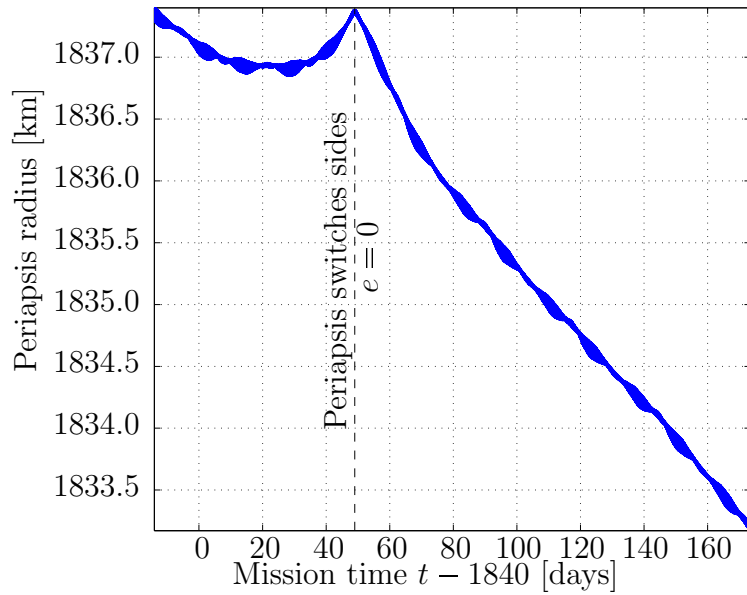


Figure 9.55: Periapsis of spacecraft during science phase. The periapsis switches from one side of the orbit to the other when $e = 0$.

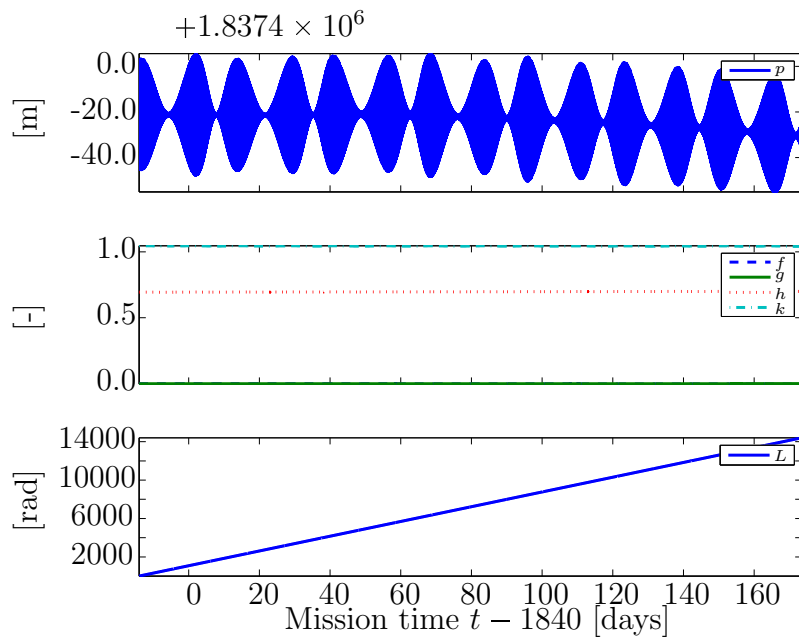


Figure 9.56: Equinoctial elements of satellite within ECI frame during science phase.

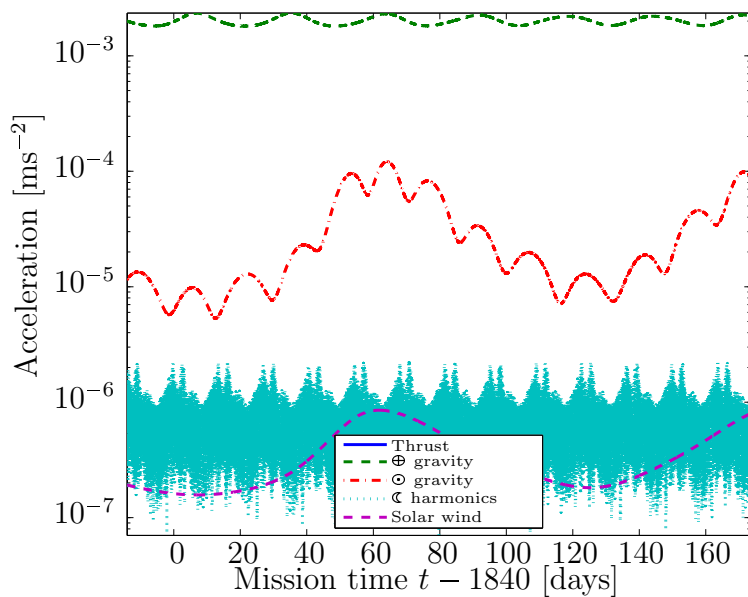


Figure 9.57: Perturbing accelerations acting on spacecraft during science phase.

9.9 Validation

For obvious reasons there have been few experimental flights to validate low-thrust trajectory theory, and no flight testing is possible to verify this particular proposed trajectory prior to final launch. Fortunately, the mechanics outlined in Chapter 5 have been well established for many decades (Kaplan 1976), and this particular implementation of them was further verified in Matlab prior to commencing work with GESOP. The optimisation routines within GESOP, and the flight mechanics of ASTOS, have been numerically verified by ESTEC, Dassault, Astrium, CNES, EADS and JAXA, among other industrial partners. ASTOS is practically validated by ongoing use on real missions launched by ESA and DLR, including Ariane 5 and Vega rocket launches, the ExoMars and Beagle 2 missions, and X38 re-entry scenarios.

The independently computed phases from GESOP are plotted together in Figure 9.58. Note that this is merely conceptual; the temporal discontinuities between phases require parking orbits be inserted, or else the trajectories be revised. Once launch data is known, the complete trajectory may be calculated. Nonetheless, it is worth comparing the trajectory to Figure 8.1 for a qualitative analysis that orbital energy is conserved.

For the purposes of further validation, the control vector profile developed in GESOP was converted into quaternions using Matlab, and then combined with the Ephemeris Time to fit the specifications for STK external attitude files. A generic scenario was then produced in STK using the external attitude files along with thruster specifications and phase lengths identical to those used in GESOP with a high precision propagator, resulting in the trajectories as seen in Figure 9.59, Figure 9.60, Figure 9.61, and Figure 9.62 for the ascent, cruise, capture and descent phases respectively.

There were minor differences between the GESOP and STK results due to different orders of accuracy in Earth oblateness and the algorithms used to calculate third body perturbations, but these differences were negligible in most cases. Figure 9.61 does highlight the importance of updating the trajectory during flight; due to these minor numerical differences, the

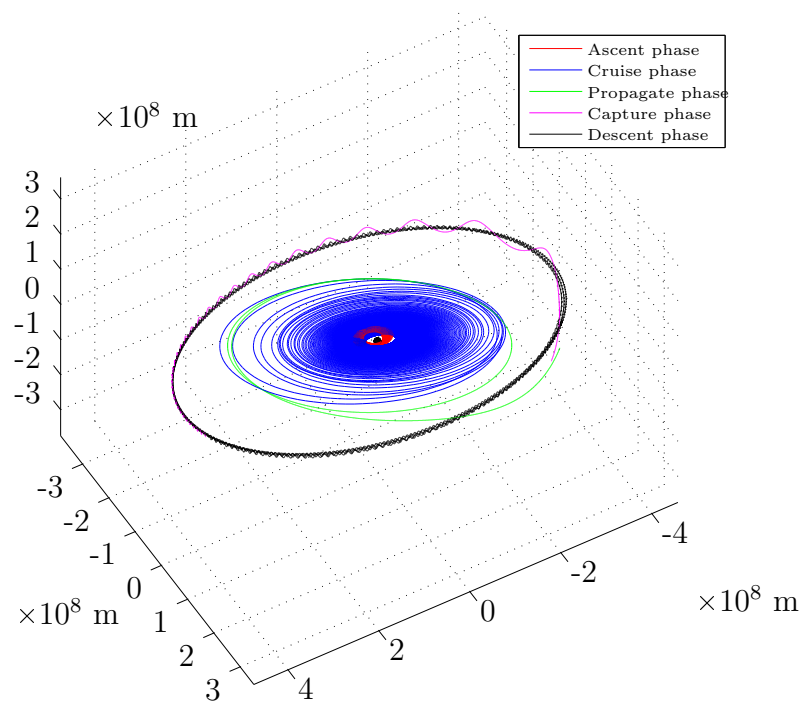


Figure 9.58: The complete GESOP trajectory shown in an ECI frame, with orthographic view.

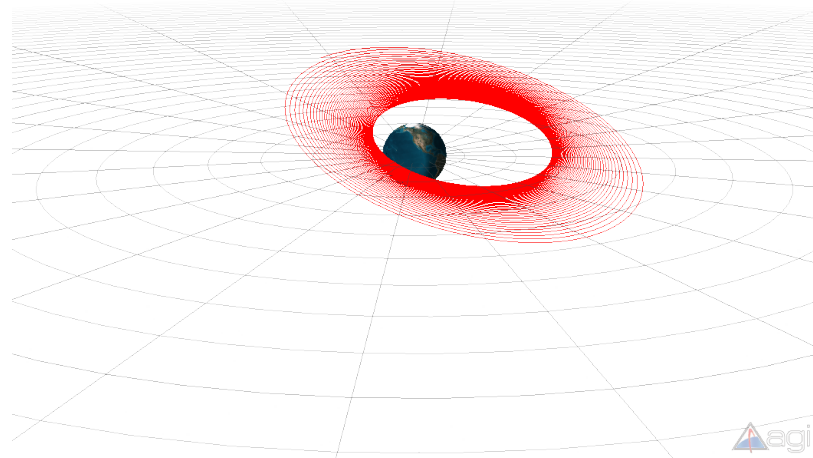


Figure 9.59: STK validation of ascent phase.

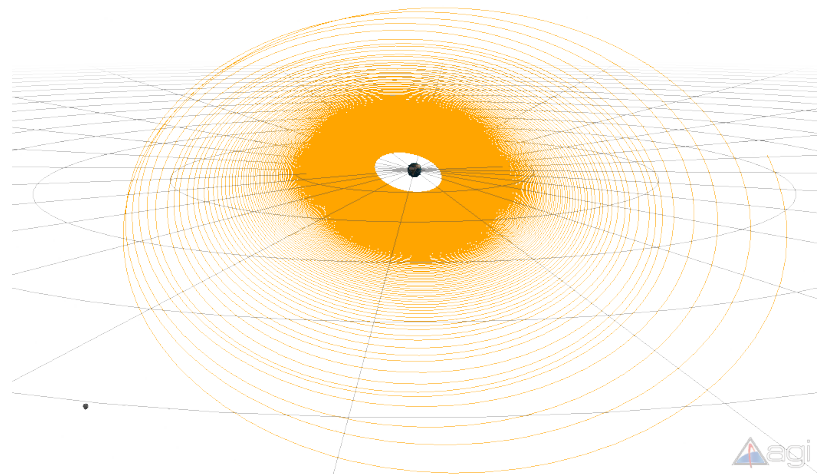


Figure 9.60: STK validation of cruise phase.

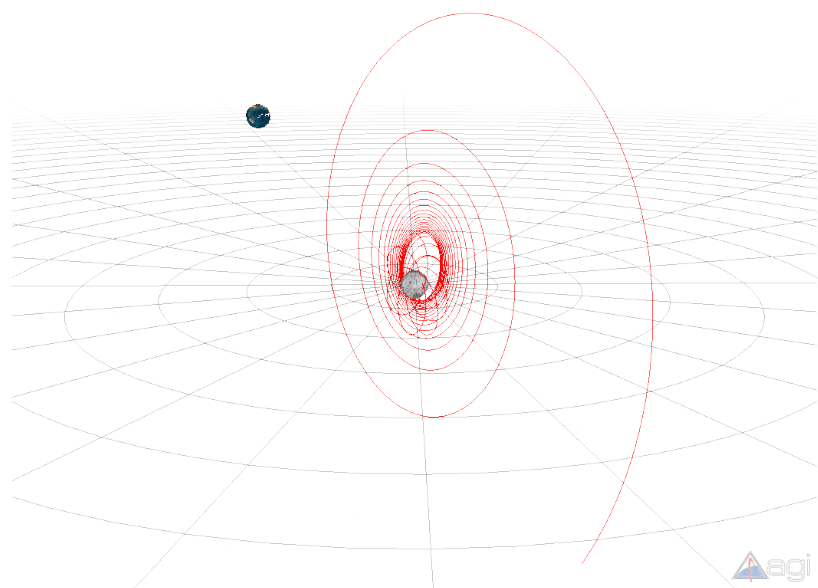


Figure 9.61: STK validation of capture phase.

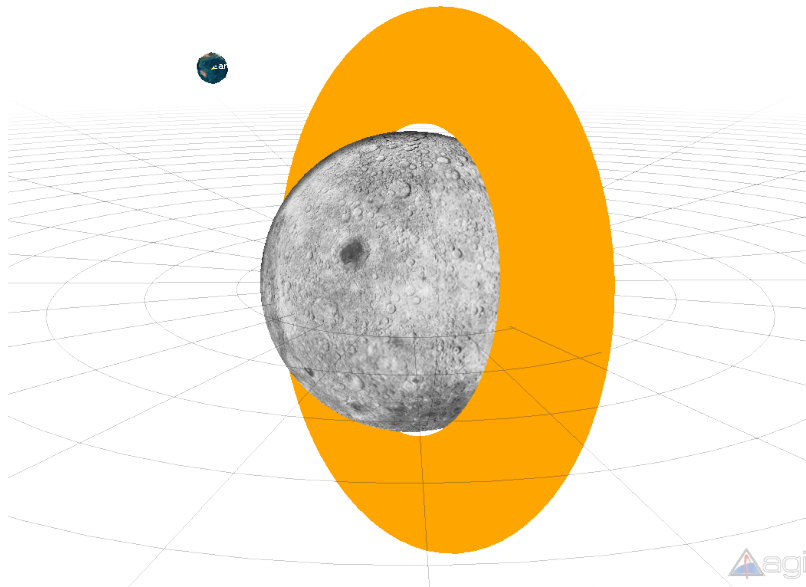


Figure 9.62: STK validation of descent phase.

thrust profile gets slightly out of synchrony with the orbit. Consequently, instead of approaching a low, circular lunar orbit the argument of periapsis starts to precess and the eccentricity increases, until the trajectory intersects the Moon’s surface. This problem could be avoided by monitoring the spacecraft’s position from the ground, and periodically uploading a revised thrust profile to the craft.

While this trajectory simulation cannot verify that the solution is optimal, it does confirm that the solution is feasible, and can be used to compare trajectories on a case-by-case basis. For example, this trajectory required 93.25 kg of ammonia propellant for the arcjet over the ascent and capture phases, and 18.98 kg of PTFE propellant for the PPTs over the cruise and descent phases. In comparison, SMART-1 used 82 kg of xenon propellant to accelerate 1.5 times the mass over a similar trajectory (Estublier et al. 2007). This discrepancy suggests that despite the efficiency of the PPT thrusters, the fuel efficiency and average I_{sp} of *Lunar Mission BW-1* are severely compromised by excessive use of the thermal arcjet. It is assumed that should sufficient computational power allow the entire

trajectory be optimised as a whole, arcjet phases would be reduced and PPT phases extended to reduce the total propellant consumption.

The fully optimised but lower complexity ascent phase verifies that this optimisation process does improve the propellant consumption. When the computational cycle was allowed to finish, the new trajectory required 6 kg less propellant at the expense of 2 days longer phase duration. This represents a 10% improvement over the phase. While the subsequent phases are too varied to assume a similar improvement, further exploitation of lunar gravitational assists and the Oberth effect will improve the fuel efficiency.

Failed optimisation runs demonstrate the robustness of the optimisation process. For example, one optimisation run for the reduced complexity ascent phase inadvertently neglected to constrain the starting mass. The optimiser subsequently maximised the final mass by increasing the starting mass up to the hard limit set by the parameter bounds (see Section 6.6.2). While this optimisation took 6 days to complete due to the chaotic solution space, the fact that the optimiser was able to incrementally adjust the starting mass all the way to the hard limit demonstrates a surprising tolerance for a stiff, chaotic solution space.

Finally, the trajectory will receive ultimate verification when the satellite is launched. Unfortunately at this stage in the design, there is still no launch date scheduled.

9.10 Summary

Results have been presented for a reduced complexity ascent phase that was able to find an optimal solution, followed by a high fidelity ascent phase that was stopped after finding a feasible solution. The cruise phase was then presented with its control profile after several thousand optimisation iterations, followed by the subsequent capture, descent and science phases. The initial guess was derived from an STK backwards propagation model which is also described.

These results do not constitute a complete trajectory due to the absence of important mission data such as launch date and spacecraft payload

mass. However, a robust trajectory design procedure is demonstrated with indicative results to aid in refining the mission architecture.

Chapter 10

Conclusion

In any complex, concave optimisation problem the only way to be certain of an optimal solution is a brute force search. This is of course computationally prohibitive. Luckily, in the context of planetary missions it is not an operational requirement to find the optimal path, merely to find a good path. In this thesis a procedure to find good paths has been outlined for *Lunar Mission BW-1*, and recommendations are made for improving the procedure in the future.

10.1 Summary of major findings

A complete trajectory has been presented for each phase in the mission architecture, with a coasting phase inserted between cruise and capture. To achieve the phase boundaries defined in the mission architecture, the transfer from GTO to LLO requires a total of 4.2 kms^{-1} . Chemically propelled trajectories typically required about 4 kms^{-1} from LEO to LLO, but as most of this impulse is applied deep within the Earth's gravity well it is magnified by the Oberth effect.

The ascent through the van Allen belts uses the higher-thrust, lower efficiency thermal arcjet to minimise the time spent in this damaging environment. Following a simple tangential thrust scheme to raise periapsis as quickly as possible resulted in this phase taking 32.22 days. A fuel optimal

Table 10.1: *Summary of numerical results from trajectory simulation*

Phase	Time (days)	Propellant (kg)	Delta-v (kms ⁻¹)	Energy (MWh)
Ascent	32.22	59.82	1.3	1.14
Cruise	1123.91	17.55	2.5	32.18
Propagate	30.0	0.0	0.0	1.15
Capture	18.0	33.43	1.0	0.475
Descent	91.79	1.43	0.4	2.72
Science	180.0	0.0	0.0	5.50

trajectory required 34.17 days but saved over 6 kg of propellant, which is 10% of the fuel required for the phase. The remaining numerical results are summarised in Table 10.1.

Based on this simulation the arcjet requires a total of 1205.28 hours of operation, and the PPTs require 29176.82 hours of operation. For comparison, the Hall-effect thrusters used for 4958 hours during the SMART-1 mission had a total of 9200 hours of ground qualification testing before flight. Maintaining the same ratio of testing to flight time requires 54140 hours of PPT ground testing before flight. This is equivalent to over 6 years of continuous thrusting in a thermal vacuum chamber.

10.2 Additions to *Lunar Mission BW-1* program

It is important to note that this project does not intend to give a complete, final trajectory for *Lunar Mission BW-1*. In fact, this would be impossible given unknowns such as launch date and payload. Rather, this project developed a procedure for determining a good trajectory once those parameters are known as well as identifying issues that need to be considered when developing the trajectory. Perhaps more importantly for mission planning, the work described in this thesis provides an estimate for the transfer duration and fuel requirements, as presented in Table 10.1. This

data should inform future revision of the mission architecture. In particular, the radiation modelling suggests that the selected boundary of the van Allen belts is too conservative; the cruise phase could start at a much lower altitude, using the much more fuel-efficient PPTs. Additionally, repeated simulations suggested the spacecraft is only susceptible to being recaptured for the first two or three orbits of the Moon during the capture phase. Consequently the descent phase could also begin much earlier, once again saving many kilograms of ammonia propellant by using the more efficient PPTs. Of course, these two strategies would both increase the total mission time. That is a decision for the project management team.

The power modelling undertaken during this project revealed that *Lunar Mission BW-1* experiences a power surplus for most of the lunar transfer. While payload standby and communications power requirements are unknown, they are not expected to exceed this surplus. Consequently, the vehicle configuration could be modified based on these results.

The excess power may be exploited by increasing the PPT pulse frequency or installing additional thruster units. Simulation of the higher thrust resulting from these modifications indicates a higher lunar approach velocity complicating rendezvous and strong capture. These simulations did perhaps suffer from implementing orbital energy as the termination condition, thus sacrificing approach velocity for low altitude. If *Lunar Mission BW-1* is to be modified to exploit the surplus power available, future trajectory modelling would be well advised to implement velocity relative to the Moon as a termination constraint. Alternatively, removing extraneous solar panels would significantly decrease the launch mass of the vehicle, and also simplify thermal control.

Furthermore, the power surplus suggests that the developmental focus of thruster research at Stuttgart on power efficiency is perhaps misplaced. Rather, fuel efficiency could be improved by focussing research on I_{sp} (by improving exhaust velocity). More practically useful would be improving the thrust; this would not only simplify complicated manoeuvres such as the lunar capture and course corrections, but it would also decrease total transfer time, currently about 3.5 years. Of course, power efficiency may be

important for other mission profiles, but to date the TALOS and SIMPLEX thrusters are only intended for use on *Lunar Mission BW-1*.

10.3 Additions to low thrust trajectory optimisation

This project has undertaken one of the highest fidelity low-thrust trajectory optimisations present in literature. It has demonstrated the feasibility of such high fidelity optimisation using SOCS, subject to the advent of faster processing and greater computer storage. While computer hardware will eventually cover this gap, in the short term SOCS suffers from its direct shooting limitation. The field of trajectory optimisation would benefit greatly from modification of the SOCS algorithm to support multiple shooting that could be distributed over multiple processor cores.

10.4 Conclusions of the research

As repeatedly highlighted in literature, making an initial guess remains one of the biggest problems to trajectory optimisation. This is in part because low thrust trajectories are extremely sensitive to small changes, resulting in narrow basins of convergence surrounded by trajectories that do not achieve lunar capture. Thus finding lunar capture scenarios is an important step in optimising the trajectory of *Lunar Mission BW-1*.

Furthermore, some conclusions can be made about the thrust profile in these initial guesses. At the start of this project a thrust profile was implemented tangential to the spacecraft's position. This circularises the orbit as it rises. Based on the limited thrust profiles available in STK a new strategy of thrusting along the velocity vector was modelled. This profile preserves the orbital elements, in particular eccentricity. While this profile loses some delta-v due to gravitational drag, maintaining a low periapsis magnifies the thrust due to the Oberth effect, while raising the apoapsis allows greater exploitation of lunar gravitational assists. The thrust profile

would be further improved under the thrust power constraints by focussing thrust over the periapsis, and coasting over apoapsis.

This strategy was ignored when the reduced complexity ascent phase was allowed to reach a fully optimised solution. In this scenario, the spacecraft uses an intermittent thrust-coast-thrust profile. While there is a possibility that this is due to power limitations, further simulations indicated that the batteries and solar panels are sized well enough to not require coasting phases, even during higher energy arcjet phases. Rather, this profile seems to be an artefact of the phase objective: raising the periapsis while using as little propellant as possible. Thus the optimisation does achieve its objective of escaping the van Allen belts very effectively. However, the overall mission objective of getting to the Moon using as little propellant as possible may benefit from additionally raising the apoapsis during this phase, by exploiting the Oberth effect to maximise the orbital energy obtained per unit of propellant expended.

Regarding the power consumption, it was revealed not to be a limiting factor on the trajectory for the planned satellite configuration. However, the discrepancy between the optimised ascent phase and the higher fidelity ascent phase revealed that power generation does increase significantly as the Earth-Moon system approaches periapsis on its orbit around the Sun. Furthermore, due to the thrust vector constraint the spacecraft attitude only has one degree of freedom (roll). Thus the power generation is also heavily dependent on the right ascension. Unfortunately, both launch date and right ascension are dependent on the launch, which is not under the control of the Institute for Space Systems.

10.5 Future work

There are quite a number of improvements that should be made if the development of *Lunar Mission BW-1* is continued.

First are a number of modelling techniques that the author came across during the project, and would implement if he were starting over. These include the parameterised departure date and thrust duty cycle described

in Section 7.4.1. Additionally, the thrust profile could be modelled using Euler angles instead of the unit vector described in Section 5.5.4. Not only is this expected to further smooth the solution space, it would supercede one of the constraint evaluations; specifically, the repeated calculations to ensure the control vector is a unit vector would no longer be required.

Secondly, subsequent to the mission architecture and vehicle configuration recommendations in Section 10.2 more detail would be required in the power modelling. Payload and communications power budgets would be required, and the power degradation model described in Section 7.3.1 should be implemented in software.

Colleagues working on the project have identified a number of lunar inclinations that reduce station-keeping costs throughout the science phase. Zeile et al. (2010) recommend a final inclination of 70° , having used an argument of periapsis of 43.3° and a right ascension of 285° , corresponding to the orbital elements in Table 10.2. This would be easily achievable using minor course corrections during the arcjet-powered capture phase, or even during the lengthy descent phase with the PPTs. The recent study by Gupta and Sharma (2011, Figure 14a) reinforces this conclusion, showing that the "transition altitude", that is, the altitude above which a sudden increase in orbital life time is observed, is lowest for a 70° inclined orbit and provides a range of right ascensions that could be trialled.

Table 10.2: Revised Keplerian elements for the final orbit of Lunar Mission BW-1 trajectory optimisation (end of descent phase)

Parameter	Value
Semimajor axis, a (m)	1.8371×10^6
Eccentricity, e (-)	0.0
Inclination, i (rad)	1.222
Argument of periapsis, ω (rad)	0.7382
Lunar Longitude of the Ascending Node, Ω (rad)	4.9742

To derive a truly optimal trajectory it would be necessary to optimise

all of the phases simultaneously to determine inter-dependencies. This was attempted early in the project, but abandoned due to hardware and software limitations. Once a completed trajectory is determined, a Monte Carlo analysis should be performed to determine the sensitivity of the trajectory to small changes in thruster performance, imperfections in gravitational modelling, and other parameters.

Finally, the author had an abstract accepted for the 62nd International Astronautical Congress on alternate mission profiles. Unfortunately completion of this thesis took precedence, but this work remains of interest to the *Lunar Mission BW-1* team. Of particular interest is the possibility to pass through, or send a parasitic probe to, the Kordylewski clouds hypothesised to exist at the Earth-Moon Lagrange points L4 and L5. The trajectory model presented herein could easily be adapted to such alternative mission scenarios.

Appendix A

Gravitational potential

Section 5.5.2 introduces potential energy models, to accurately calculate the gravitational field around a central body, and thus the gravitational forces a nearby spacecraft would experience. The rather complicated equation (A.1) is reproduced from National Imagery and Mapping Agency (2000), representing the gravitational component of the potential (compared to the angular momentum component),

$$V = \frac{\mu}{r} \left[1 + \sum_{n=2}^{n_{max}} \sum_{m=0}^n \left(\frac{a}{r} \right)^n \bar{P}_{nm}(\sin \phi') (\bar{C}_{nm} \cos m\lambda + \bar{S}_{nm} \sin m\lambda) \right]. \quad (\text{A.1})$$

The parameters n and m are the degree and order of the normalised gravitational coefficients, r is the distance from the body's centre of mass, ϕ' is the polar latitude and λ is the polar longitude. The gravitational coefficients, \bar{C}_{nm} and \bar{S}_{nm} are published in data tables with the gravitational constant for the central body, μ , and the semimajor axis of the oblate body, a . For $m = 0$, $k = 1$ and for $m \neq 0$, $k = 2$. The remaining term within the two summation series, is described as a normalised associated Legendre polynomial,

$$\bar{P}_{nm}(\sin \phi') = \left[\frac{(n-m)!(2n+1)k}{(n+m)!} \right]^{\frac{1}{2}} P_{nm}(\sin \phi'), \quad (\text{A.2a})$$

where $P_{nm}(\sin \phi')$ is the associated Legendre polynomial,

$$P_{nm}(\sin \phi') = (\cos \phi')^m \frac{d^m}{d(\sin \phi')^m} [P_n(\sin \phi')], \quad (\text{A.2b})$$

and $P_n(\sin \phi')$ is the Legendre polynomial,

$$P_n(\sin \phi') = \frac{d^n}{2^n n! d(\sin \phi')^n} (\sin^2 \phi' - 1)^n. \quad (\text{A.2c})$$

According to National Imagery and Mapping Agency (2000) the series is theoretically valid for $r \geq a$, though it can be used with probably negligible error near or on the body's surface, that is, $r \geq$ body's surface. The series should not be used for $r <$ body's surface.

Due to minor differences in the definitions of gravitational harmonics, the zonal harmonic, J_2 , is equivalent to $-C_{2,0}$.

Appendix B

Thruster characteristics

B.1 Pulsed plasma thrusters

Table B.1 shows laboratory performance data from a variety of pulsed plasma thrusters that were developed at the Institute for Space Systems at the University of Stuttgart, and was provided to the author by Mr. Matthias Lau. All tests were performed at a pulse frequency of 1 Hz. Thrust and energy consumption may be scaled linearly by varying pulse frequency, subject to wear and tear limiting the total number of pulses that the PPTs can deliver, and the thermal equilibrium of the materials attenuating the heat generated by the thruster.

Table B.1: *Performance of the instationary magnetoplasmadynamic (iMPD) thrusters from laboratory tests at IRS, University of Stuttgart*

Model	Power (W)	Mass bit (μg)	Thrust (mN)	Exhaust velocity (m/s)	Specific impulse (s)	Thrust efficiency (%)
TEMP	4.3	50	0.120	2400	245	3.3
SIMPLEX	66.0	49	0.890	18347	1870	12.4
ASL-3C	67.6	53	1.373	25721	2622	26.1
ASL-3D	16.7	16	0.421	25844	2634	32.6

The first entry is from an early test bench model called TEMP. The second entry is the SIMPLEX PPT, operating with a capacitance of $33.59 \mu\text{F}$ to trigger the pulse. The third entry is for the modified ADD-SIMPLEX-3C, operating at $80 \mu\text{F}$. The final entry is ASL-3D, at $60 \mu\text{F}$.

B.2 Thermal arcjet

The laboratory performance data in Table B.2 for a variety of thermal arcjets developed at the Institute for Space Systems at the University of Stuttgart was provided to the author by Mr. Birk Wollenhaupt. Four separate arcjets are represented in this data: VELARC, ATOS 1, ATOS 2 / ARTUR and TALOS. All four were tested using ammonia (NH_3) as the reaction mass. The ATOS 1 thruster was flight tested on board AMSAT-P-3D, launched by DLR in 2000.

Table B.2: *Performance of thermal arcjet models from laboratory tests at IRS, University of Stuttgart*

	Power (W)	Mass flow rate (mg/s)	Thrust (mN)	Exhaust velocity (m/s)	Specific impulse (s)	Thrust efficiency (%)
VELARC	375	12.5	45	3630	370	22.0
	280	9.3	35	3710	378	22.9
	680	20.8	98	4688	478	33.6
	260	6.7	26	3806	388	18.7
	345	10.7	43	3995	407	24.8
ATOS 1	750	24	115	4750	484	36.7
	748	24	114	4709	480	36.2
	750	22.5	95	4222	430	26.7
ATOS 2 / ARTUR	796	22.1	107	4836	493	32.5
	1503	22.1	137	6200	632	28.3
	892	26.8	128	4758	485	34.0
	1512	26.8	161	6004	612	32.0
	868	31	144	4630	472	38.3
	1463	31	183	5915	603	37.1
	983	36	167	4640	473	39.4
	1858	36	221	6131	625	36.4
TALOS	800	21.5	103	4767	486	30.5
	796	21	111	5297	540	37.0
	800	21.9	108	4915	501	33.1
	800	20.0	103	5140	524	32.9
	800	18.0	95	5278	538	31.3
	800	15.9	85	5366	547	28.6
	800	13.8	74	5356	546	24.8

References

- Angelopoulos V (2011) “The ARTEMIS Mission” in *Space Science Reviews* **165**(1–4) pp. 3–25 DOI: [10.1007/s11214-010-9687-2](https://doi.org/10.1007/s11214-010-9687-2) (cited on page 11).
- Bartholomew-Biggs MC, Dixon LCW, Hersom SE, and Maany ZA (1988) “The solution of some difficult problems in low-thrust interplanetary trajectory optimization” in *Optimal Control Applications and Methods* **9**(3) pp. 229–251 DOI: [10.1002/oca.4660090303](https://doi.org/10.1002/oca.4660090303) (cited on page 32).
- Battin RH (1999) *An Introduction to the Mathematics and Methods of Astrodynamics* 2nd Edition, AIAA Education Series (cited on page 68).
- Belbruno E (2004) *Capture Dynamics and Chaotic Motions in Celestial Mechanics*, Princeton University Press, Princeton (cited on page 107).
- Belbruno EA and Miller JK (1993) “Sun-perturbed earth-to-moon transfers with ballistic capture” in *Journal of Guidance, Control, and Dynamics* **16**(4) pp. 770–775 DOI: [10.2514/3.21079](https://doi.org/10.2514/3.21079) (cited on page 107).
- Bellman R (1957) *Dynamic Programming*, Princeton University Press, New Jersey, United States (cited on page 31).
- Betts JT (1994) “Optimal interplanetary orbit transfers by direct transcription” in *Journal of the Astronautical Sciences* **42**(3) pp. 247–268 (cited on pages 40, 66, 67).
- Betts JT (1998) “Survey of numerical methods for trajectory optimization” in *Journal of Guidance, Control, and Dynamics* **21**(2) pp. 193–207 DOI: [10.2514/2.4231](https://doi.org/10.2514/2.4231) (cited on pages 25, 26, 29, 34, 101).

- Betts JT (2000) “Very low-thrust trajectory optimization using a direct SQP method” in *Journal of Computational and Applied Mathematics* **120**(1) pp. 27–40 DOI: 10.1016/S0377-0427(00)00301-0 (cited on pages 10, 40).
- Betts JT (2010) *Practical Methods for Optimal Control and Estimation Using Nonlinear Programming* 2nd Edition, Society for Industrial and Applied Mathematics (cited on page 84).
- Betts JT and Erb SO (2003) *Computing optimal low thrust trajectories to the Moon* Technical Report 516, European Space Agency, Frascati, Italy, pp. 143–146 (cited on pages 40, 41, 76, 119).
- Betts JT and Gablonsky JM (2002) *A Comparison of Interior Point and SQP Methods on Optimal Control Problems* Technical Report M&CT-TECH-02-004, Mathematics and Computing Technology, Phantom Works, The Boeing Company, Seattle (cited on page 33).
- Betts JT and Huffman WP (1993) “Path-constrained trajectory optimization using sparse sequential quadratic programming” in *Journal of Guidance, Control, and Dynamics* **16**(1) pp. 59–68 DOI: 10.2514/3.11428 (cited on page 40).
- Betts J and Huffman W (2002) *SOCS User’s Guide* M&CT-TECH-01-014, Version 7.1, The Boeing Corporation, Seattle, WA (cited on page 33).
- Bock D, Herdrich G, Kurtz H, Röser HP, and Auweter-Kurtz M (2007) “An advanced ammonia propellant feed system for the thermal arcjet TALOS” in *43rd AIAA/ASME/SAE/ASEE Joint Propulsion Conference* Volume 2, Cincinnati, OH, United States, pp. 1759–1764 (cited on page 3).
- Bock HG and Plitt KJ (1984) “A multiple shooting algorithm for direct solution of optimal control problems” in *9th World Congress*, International Federation of Automatic Control, San Diego, California, pp. 1603–1608 (cited on page 32).

- Brauer GL, Cormick DE, and Stevenson R (1977) *Capabilities and Applications of the Program to Optimize Simulated Trajectories* NASA Contractor Report CR-2770, NASA (cited on page 32).
- Breakwell J and Rauch H (1966) “Optimum guidance for low thrust interplanetary vehicle” in *AIAA Journal* **4**(4) pp. 693–704 DOI: 10.2514/3.3510 (cited on page 35).
- Broucke RA and Cefola PJ (1972) “On the equinoctial orbit elements” in *Celestial Mechanics and Dynamical Astronomy* **5**(3) pp. 303–310 DOI: 10.1007/BF01228432 (cited on page 64).
- Bulirsch R (1971) *Die Mehrzielmethode zur numerischen Lösung von nicht-linearen Randwertproblemen und Aufgaben der optimalen Steuerung* Technical Report, Carl-Cranz-Gesellschaft e.V., Oberpfaffenhofen, Germany (cited on page 32).
- Bureau International des Poids et Mesures (1901) *Resolution of the 3rd meeting of the General Conference on Weights and Measures*, Bureau International des Poids et Mesures, Paris (cited on page vi).
- Cabrera PAM (2011) “Pulsed Plasma Thrusters: A Global Review and Long Yearned Classification”, Masters’ thesis, International Space University (cited on page 90).
- Carnelli I, Dachwald B, and Vasile M (2007) “Optimizing low-thrust gravity assist interplanetary trajectories using evolutionary neurocontrollers” in *IEEE Congress on Evolutionary Computation*, Singapore, pp. 965–972 DOI: 10.1109/CEC.2007.4424574 (cited on page 42).
- Carnelli I, Dachwald B, and Vasile M (2009) “Evolutionary neurocontrol: A novel method for low-thrust gravity-assist trajectory optimization” in *Journal of Guidance, Control, and Dynamics* **32**(2) pp. 615–624 DOI: 10.2514/1.32633 (cited on page 42).
- Chobotov V (2002) *Orbital Mechanics* 3rd Edition, AIAA Education Series (cited on pages 55, 64, 72).

- Choueiri E (2004) “A Critical History of Electric Propulsion: The First 50 Years (1906-1956)” in *Journal of Propulsion and Power* **20**(2) pp. 193–203 DOI: 10.2514/1.9245 (cited on page 1).
- Coleman TF and Moré JJ (1983) “Estimation of Sparse Jacobian Matrices and Graph Coloring Problems” in *Journal of Numerical Analysis* **20**(1) pp. 187–209 DOI: 10.1137/0720013 (cited on page 33).
- Coverstone-Carroll V, Hartmann J, and Mason W (2000) “Optimal multi-objective low-thrust spacecraft trajectories” in *Computer Methods in Applied Mechanics and Engineering* **186**(2) pp. 387–402 DOI: 10.1016/S0045-7825(99)00393-X (cited on page 79).
- Curtis AR, Powell MJD, and Reid JK (1974) “On the Estimation of Sparse Jacobian Matrices” in *Journal of Applied Mathematics* **13**(1) pp. 117–119 DOI: 10.1093/imamat/13.1.117 (cited on page 33).
- Dachwald B (2005) “Optimization of very-low-thrust trajectories using evolutionary neurocontrol” in *Acta Astronautica* **57**(2-8) pp. 175–185 DOI: 10.1016/j.actaastro.2005.03.004 (cited on pages 9, 43).
- Dachwald B and Ohndorf A (2007) “1st ACT global trajectory optimisation competition: Results found at DLR” in *Acta Astronautica* **61**(9) pp. 742–752 DOI: 10.1016/j.actaastro.2007.03.011 (cited on pages 42, 105).
- Deutsches GeoForschungsZentrum (2009) *GRACE (Gravity Recovery And Climate Experiment)* URL: <http://www-app2.gfz-potsdam.de/pb1/op/grace/> (visited on [visited on May 13, 2009]) (cited on page 70).
- Dréo J, Siarry P, Pétrowski A, and Taillard E (2006) *Metaheuristics for Hard Optimization*, Springer-Verlag, Berlin & Heidelberg DOI: 10.1007/3-540-30966-7_6 (cited on page 32).
- Edelbaum T (1964) “Optimum low-thrust rendezvous and station keeping” in *AIAA Journal* **2**(7) pp. 1196–1201 DOI: 10.2514/3.2521 (cited on pages 37, 105).

- Enright PJ and Conway BA (1992) “Discrete approximations to optimal trajectories using direct transcription and Nonlinear Programming” in *Journal of Guidance, Control, and Dynamics* **15**(4) pp. 994–1002 DOI: 10.2514/3.20934 (cited on page 39).
- Erb S (2002) “Trajectory Optimization of a Moon Transfer from GTO employing Solar Electric Propulsion”, Masters’ thesis, Mathematics and Computing Technologies, Phantom Works, The Boeing Company, Seattle (cited on pages 40, 64, 66, 67, 96, 97).
- Eshagh M and Najafi Alamdari M (2007) “Perturbations in orbital elements of a low earth orbiting satellite” in *Journal of the Earth & Space Physics* **33**(1) pp. 1–12 (cited on page 71).
- Estublier D, Saccoccia G, and Amo JG del (2007) *Electric Propulsion on SMART-1* ESA Bulletin 129, ESTEC, Noordwijk, The Netherlands (cited on pages 20, 170).
- Euler L (1911) “Investigatio perturbationum quibus planetarum motus ob actionem eorum mutuam afficiuntur” in *Opera Omnia* edited by Rudio F, Krazer A, and Stackel P Volume 26, Societatis Scientiarum Naturalium Helveticae (cited on page 34).
- European Space Agency (2008a) *ESA Science & Technology: LISA Pathfinder* URL: <http://sci.esa.int/lisapathfinder> (visited on [visited on Aug. 13, 2008]) (cited on page 22).
- European Space Agency (2008b) *ESA Science & Technology: SMART-1* URL: <http://sci.esa.int/smart1/> (visited on [visited on Aug. 5, 2008]) (cited on pages 16, 19).
- Falke A, Hartling M, Laufer R, and Röser HP (2004) “Implementation of a simulation environment for software hardware simulation of power management for a lunar small satellite mission” in *55th International Astronautical Congress* Volume 6, International Astronautical Federation, Vancouver, Canada, pp. 3651–3661 (cited on page 99).
- Fermat P de (1891–1912) *Oeuvres de Fermat* Volume 5, Gauthier-Villars et fils, Paris, pp. 120–125 (cited on page 27).

- Fischer D, Markl A, Wiegand A, Gath P, Well K, Paus M, Wiekert S, Cremaschi F, and Schaeff S (2008) *ASTOS User Manual*, Version 7.0.2, ASTOS Solutions GmbH, Unterkirnach, Germany (cited on pages 26, 33, 86, 101).
- Folkner W, Williams J, and Boggs D (2008) *The Planetary and Lunar Ephemeris DE 421* Technical Report 343R-08-003, Jet Propulsion Laboratory, California Institute of Technology (cited on page 66).
- Gao Y (2008) “Low-Thrust Nonlinear Guidance by Tracking Mean Orbital Elements” in *Journal of Guidance, Control, and Dynamics* **31**(4) pp. 1103–1110 DOI: 10.2514/1.31256 (cited on page 105).
- Gauss CF (1827) *Disquisitiones generales circa superficies curvas*, Societati regiae oblatae, Göttingen (cited on page 29).
- Gill P, Murray W, and Saunders M (1997) *SNOPT: An SQP algorithm for large-scale constrained optimization* Technical Report 97-2, Department of Mathematics, University of California, San Diego, La Jolla, CA (cited on page 33).
- Gill PE, Murray W, Saunders MA, and Wright MH (1987) *A Schur-complement Method for Sparse Quadratic Programming* Technical Report SOL 87-12, Department of Operations Research, Stanford University, Stanford, CA (cited on page 33).
- Golan OM and Breakwell JV (1994) “Minimum fuel lunar trajectories for a low-thrust power-limited spacecraft” in *Dynamics and Control* **4**(4) pp. 383–394 DOI: 10.1007/BF01974142 (cited on pages 35, 36).
- Gontier AM, Ma C, Arias EF, Eubanks TM, Fey AL, Jacobs CS, Sovers OJ, Archinal BA, and Charlot P (2002) “Establishment of the ICRF” in *Advances in Space Research* **30**(2) pp. 185–193 DOI: 10.1016/S0273-1177(02)00283-1 (cited on page 59).
- Guelman M (1995) “Earth-to-Moon transfer with a limited power engine” in *Journal of Guidance, Control, and Dynamics* **18**(5) pp. 1133–1138 DOI: 10.2514/3.21515 (cited on page 36).

- Guelman M, Kogan A, and Gipsman A (2000) “Asymptotic optimization of very long, low thrust propelled inter-orbital maneuvers” in *Acta Astronautica* **47**(2) pp. 489–502 DOI: [10.1016/S0094-5765\(00\)00088-6](https://doi.org/10.1016/S0094-5765(00)00088-6) (cited on page 36).
- Gupta S and Sharma RK (2011) “Effect of Altitude, Right Ascension of Ascending Node and Inclination on Lifetime of Circular Lunar Orbits” in *International Journal of Astronomy and Astrophysics* **1**(1) pp. 155–163 DOI: [10.4236/ijaa.2011.13020](https://doi.org/10.4236/ijaa.2011.13020) (cited on pages 151, 164, 178).
- Haeussermann W (1965) “Guidance and Control of Saturn Launch Vehicles” in *AIAA Second Annual Meeting*, 65–304, NASA, American Institute of Aeronautics and Astronautics, San Francisco, California (cited on page 28).
- Hargraves C and Paris S (1987) “Direct Trajectory Optimization Using Nonlinear Programming and Collocation” in *Journal of Guidance, Control, and Dynamics* **10**(4) pp. 338–342 DOI: [10.2514/3.20223](https://doi.org/10.2514/3.20223) (cited on page 32).
- Hechler M (2002) “Power degradation modelling in the SMART-1 mission analysis” in *CNES Seminar on van Allen Radiation Modelization*, TOS-GMA, ESOC, Darmstadt, Germany (cited on page 97).
- Herbiniere S, Martinot V, Geffroy S, and Brousse P (2000) “Low-thrust eccentricity and out-of-plane corrections” in *Advances in the Astronautical Sciences* **105**(I) pp. 595–605 (cited on page 105).
- Herman AL and Conway BA (1998) “Optimal, low-thrust, Earth-Moon orbit transfer” in *Journal of Guidance, Control, and Dynamics* **21**(1) pp. 141–147 DOI: [10.2514/2.4210](https://doi.org/10.2514/2.4210) (cited on page 40).
- Herring TA, Gwinn CR, and Shapiro II (1986) “Geodesy by Radio Interferometry: Studies of the Forced Nutations of the Earth” in *Journal of Geophysical Research* **91**(B5) pp. 4755–65 DOI: [10.1029/JB091iB05p04755](https://doi.org/10.1029/JB091iB05p04755) (cited on page 60).
- Hess WN (1968) *The Radiation Belt and Magnetosphere*, Blaisdell Publishing Co. (cited on page 49).

- Hintz GR (2008) “Survey of orbit element sets” in *Journal of Guidance, Control, and Dynamics* **31**(3) pp. 785–790 DOI: 10.2514/1.32237 (cited on pages 64, 65).
- Ichimura Y and Ichikawa A (2008) “Optimal Impulsive Relative Orbit Transfer Along a Circular Orbit” in *Journal of Guidance, Control, and Dynamics* **31**(4) pp. 1014–1027 DOI: 10.2514/1.32820 (cited on page 79).
- Indian Space Research Organisation Publications and Public Relations (2007) *GSLV-F04*, Launch Vehicle Manual, Indian Space Research Organisation, Bangalore (cited on page 80).
- Institut für Raumfahrtssysteme, Universität Stuttgart (2008) *Stuttgart Small Satellite Program: Lunar Mission BW-1* URL: <http://www.kleinsatelliten.de/bw1/index.en.php> (visited on [visited on Apr. 14, 2008]) (cited on pages 4, 16, 98).
- Jackson K and Coverstone V (2008) “Optimal Lunar Launch Trajectories to the Sun-Earth L1 Vicinity” in *Journal of Guidance, Control and Dynamics* **31**(3) pp. 712–719 DOI: 10.2514/1.30877 (cited on page 43).
- Jänsch C and Paus M (1990) “Aircraft trajectory optimization with direct collocation using movable gridpoints” in *American Control Conference*, San Diego, California, pp. 262–267 (cited on page 32).
- Japanese Aerospace Exploration Agency (2008) *ISAS: Asteroid Exploration Hayabusa (MUSES-C)* URL: <http://www.isas.jaxa.jp/e/enterp/missions/hayabusa/index.shtml> (visited on [visited on Aug. 5, 2008]) (cited on pages 16, 19).
- Jet Propulsion Laboratory (2004) *JPL HORIZONS ephemeris computation service* URL: <http://ssd.jpl.nasa.gov/?horizons> (visited on [visited on Feb. 26, 2009]) (cited on page 66).
- Jet Propulsion Laboratory (2008a) *Dawn: Mission: Ion Propulsion* URL: http://dawn.jpl.nasa.gov/mission/ion_prop.asp (visited on [visited on June 11, 2008]) (cited on pages 16, 21, 22).

- Jet Propulsion Laboratory (2008b) *Deep Space 1* URL: <http://sse.jpl.nasa.gov/missions/profile.cfm> (visited on [visited on May 3, 2008]) (cited on pages 16–18).
- Kaplan M (1976) *Modern Spacecraft Dynamics and Control*, John Wiley & Sons (cited on pages 62, 67, 167).
- Kemble S (2006) *Interplanetary Mission Analysis and Design*, Springer-Verlag, Berlin & Heidelberg (cited on pages 11, 55, 102, 104).
- Keppeler J (2000) “Calculation of Perturbed Keplerian Orbits with Non-Singular Orbit Elements”, Masters’ thesis, Institut für Flugmechanik und Flugregelung, Universität Stuttgart (cited on pages 61, 64, 67).
- Kirkpatrick S, Gelatt CD, and Vecchi MP (1983) “Optimization by Simulated Annealing” in *Science* **220**(4598) pp. 671–680 DOI: [10.1126/science.220.4598.671](https://doi.org/10.1126/science.220.4598.671) (cited on page 31).
- Kluever CA and Chang KR (1996) “Near-optimal low-thrust lunar trajectories” in *Journal of Guidance, Control, and Dynamics* **19**(2) pp. 494–496 DOI: [10.2514/3.21645](https://doi.org/10.2514/3.21645) (cited on page 37).
- Kluever CA and Pierson BL (1995) “Optimal low-thrust three-dimensional Earth-Moon trajectories” in *Journal of Guidance, Control, and Dynamics* **18**(4) pp. 830–837 DOI: [10.2514/3.21466](https://doi.org/10.2514/3.21466) (cited on pages 1, 37, 44, 111).
- Kluever CA and Pierson BL (1997) “Optimal Earth-Moon trajectories using nuclear electric propulsion” in *Journal of Guidance, Control, and Dynamics* **20**(2) pp. 239–245 DOI: [10.2514/2.4058](https://doi.org/10.2514/2.4058) (cited on pages 37, 38).
- Konopliv AS, Asmar SW, Carranza E, Sjogren WL, and Yuan DN (2001) “Recent gravity models as a result of the Lunar Prospector mission” in *Icarus* **150**(1) pp. 1–18 DOI: [10.1006/icar.200.6573](https://doi.org/10.1006/icar.200.6573) (cited on page 71).
- Kraft D (1994) “Algorithm 733: TOMP - Fortran modules for optimal control calculations” in *ACM Transactions on Mathematical Software* **20**(3) pp. 262–281 DOI: [10.1145/192115.192124](https://doi.org/10.1145/192115.192124) (cited on page 32).

- Kreyszig E (1979) *Advanced Engineering Mathematics* 4th Edition, John Wiley & Sons, Inc., New York, United States (cited on page 25).
- Laufer R (2010) “Lunar Mission BW1: Scientific Objectives and Small Satellite Concept”, PhD thesis, Institute of Space Systems (IRS), Universität Stuttgart (cited on pages 98, 99).
- Lee S, Von Allmen P, Fink W, Petropoulos AE, and Terrile RJ (2005a) “Design and optimization of low-thrust orbit transfers” in *IEEE Aerospace Conference Proceedings* Volume 2005, Big Sky, MT, United States DOI: [10.1109/AERO.2005.1559377](https://doi.org/10.1109/AERO.2005.1559377) (cited on page 22).
- Lee S, Fink W, Russell RP, Allmen P von, Petropoulos AE, and Terrile RJ (2005b) “Evolutionary computing for low-thrust navigation” in *Collection of Technical Papers - AIAA Space 2005 Conference and Exposition* Volume 3, Long Beach, CA, United States, pp. 1775–1782 (cited on pages 43, 79).
- LePage AJ (1991) “The Mystery of ZOND 2” in *The Electronic Journal of the Astronomical Society of the Atlantic* **2**(9) (cited on page 15).
- Letterio F (2005) “Optimization of a Satellite Transfer Trajectory with Low Thrust Electric Propulsion From Earth Orbit to an Orbit over the Van Allen Radiation Belt”, Masters’ thesis, Institut für Raumfahrtssysteme, Universität Stuttgart (cited on pages 4, 11, 41, 62, 64, 67, 80).
- Lieske JH, Lederle T, Fricke W, and Morando B (1977) “Expression for the Precession Quantities Based upon the IAU (1976) System of Astronomical Constants” in *Astronomy & Astrophysics* **58**(1–2) pp. 1–16 (cited on page 60).
- Longo CRO and Rickman SL (1995) *Method for the Calculation of Spacecraft Umbra and Penumbra Shadow Terminator Points* Technical Paper 3547, NASA, Houston, Texas (cited on page 91).

- LRO Project and LGCWG White Paper (2008) *A Standardized Lunar Coordinate System for the Lunar Reconnaissance Orbiter and Lunar Datasets* Technical Report Version 5, Goddard Space Flight Center, Maryland (cited on page 60).
- Ma C, Arias EF, Eubanks TM, Fey AL, Gontier AM, Jacobs CS, Sovers OJ, Archinal BA, and Charlot P (1998) “The International Celestial Reference Frame as realized by very long baseline interferometry” in *Astronomical Journal* **116**(1) pp. 516–46 (cited on page 58).
- Manzella D (2008) “Low Cost Electric Propulsion Thruster for Deep Space Robotic Science Missions” in *2007 NASA Science and Technology Conference*, NASA/TM 215067, Glenn Research Center, Cleveland, Ohio, National Aeronautics and Space Administration, College Park, Maryland (cited on page 1).
- Masatoshi M, Takashi K, and Jun’Ichiro K (2003) “MUSES-C (Hayabusa) Trajectory Design” in *Uchu Kagaku Gijutsu Rengo Koenkai Koenshu* **47**(1) pp. 1055–1056 (cited on page 19).
- McKay R, Macdonald M, Biggs J, and McInnes C (2011) “Survey of Highly Non-Keplerian Orbits with Low-Thrust Propulsion” in *Journal of Guidance, Control, and Dynamics* **34**(3) pp. 645–666 DOI: 10.2514/1.52133 (cited on pages 34, 35).
- Miele A (1975) “Recent Advances In Gradient Algorithms For Optimal Control Problems” in *Journal of Optimization Theory and Applications* **17**(5-6) pp. 361–430 DOI: 10.1007/BF00932781 (cited on page 32).
- Milani A and Nobili AM (1987) “Integration error over very long time spans” in *Celestial Mechanics and Dynamical Astronomy* **43**(1) pp. 1–34 DOI: 10.1007/BF01234550 (cited on page 85).
- Möllman C (2005) “Einfluß des Schubmodells auf die Optimierung von Niedrigschub-Mondtransfers mit Gravity Assist”, Masters’ thesis, Institut für Raumfahrtsysteme, Universität Stuttgart (cited on page 4).
- Montenbruck O and Gill E (2000) *Satellite Orbits*, Springer-Verlag, Berlin & Heidelberg (cited on pages 60, 71, 95).

- Mueller J (2000) “Thruster Options for Microspacecraft: A Review and Evaluation of State-of-the-Art and Emerging Technologies” in *Micro Propulsion for Small Spacecraft* edited by Micci M and Ketsdever A Volume 187, Progress in Aeronautics and Astronautics American Institute of Aeronautics and Astronautics chapter 3 (cited on page 90).
- National Aeronautics and Space Administration (2012) *Apollo 11 Launch* URL: <http://dayton.hq.nasa.gov/ABSTRACTS/GPN-2000-000629.html> (visited on [visited on May 15, 2012]) (cited on page 17).
- National Imagery and Mapping Agency (2000) *Department of Defense (DoD) World Geodetic System 1984 (WGS84)* Technical Report, National Imagery and Mapping Agency (cited on pages 65, 70, 181, 182).
- National Space Science Data Center (2008) *NASA - NSSDC - Spacecraft Hayabusa (MUSES-C) - Details* URL: <http://nssdc.gsfc.nasa.gov/nmc/spacecraftDisplay.do?id=2003-019A> (visited on [visited on Aug. 13, 2008]) (cited on page 20).
- Navigation and Ancillary Information Facility (2010) *Time Conversion and Time Formats* Technical Report, NASA (cited on page 58).
- Nawaz A, Lau M, Herdrich G, and Auweter-Kurtz M (2008) “Investigation of the magnetic field in a pulsed plasma thruster” in *AIAA Journal* **46**(11) pp. 2881–2889 DOI: [10.2514/1.37161](https://doi.org/10.2514/1.37161) (cited on pages 3, 55, 90).
- Newton I (1687) *Philosophiae naturalis principia mathematica*, Jussu Societatis Regiae, Londini (cited on pages 51, 62).
- Newton I (1711) *Analysis per quantitatum series, fluxiones, ac differentias*, Ex Officina Pearsoniana, Londini (cited on page 29).
- Newton I (1736) *De metodis fluxionum et serierum infinitarum*, Londini (cited on page 29).
- Oberth H (1923) *Die Rakete zu den Planetenräumen*, R. Oldenbourg, München (cited on page 104).

- Ohlmeyer EJ and Phillips CA (2006) “Generalized vector explicit guidance” in *Journal of Guidance, Control, and Dynamics* **29**(2) pp. 261–268 DOI: 10.2514/1.14956 (cited on page 28).
- Ohndorf A, Dachwald B, and Gill B (2009) “Optimization of low-thrust earth-moon transfers using evolutionary neurocontrol” in *IEEE Congress on Evolutionary Computation*, Trondheim, Norway, pp. 358–364 DOI: 10.1109/CEC.2009.4982969 (cited on page 42).
- Petit G and Luzum B (2010) *IERS Conventions (2010)* Technical Report 36, International Earth Rotation Service, Frankfurt am Main (cited on page 70).
- Petropoulos AE, Kowalkowski TD, Vavrina MA, Parcher DW, Finlayson PA, Whiffen GJ, and Sims JA (2007) “1st ACT global trajectory optimisation competition: Results found at the Jet Propulsion Laboratory” in *Acta Astronautica* **61**(9) pp. 806–815 DOI: 10.1016/j.actaastro.2007.03.013 (cited on pages 7, 41, 42).
- Petukhov VG, Konstantinov MS, and Fedotov GG (2007) “1st ACT Global Trajectory Optimisation Competition: Results found at Moscow Aviation Institute and Khrunichev State Research and Production Space Center” in *Acta Astronautica* **61**(9) pp. 775–785 DOI: 10.1016/j.actaastro.2007.03.006 (cited on page 11).
- Pierson BL and Kluever CA (1994) “Three-stage approach to optimal low-thrust Earth-Moon trajectories” in *Journal of Guidance, Control, and Dynamics* **17**(6) pp. 1275–1282 DOI: 10.2514/3.21344 (cited on pages 36, 37).
- Pollard JE (2000) *Simplified Analysis of Low-Thrust Orbital Maneuvers* Technical Report TR-2000(8565)-10, The Aerospace Corporation, El Segundo, California (cited on page 105).
- Pontryagin LS, Boltjanski W, Gamkreidze RV, and Mishchenko EF (1962) *The Mathematical Theory of Optimal Processes*, Wiley-Intersciences, New York (cited on page 28).

- Racca G, Marini A, Stagnaro L, Van Dooren J, Di Napoli L, Foing B, Lumb R, Volp J, Brinkmann J, Grunagel R, Estublier D, Tremolizzo E, McKay M, Camino O, Schoemaekers J, Hechler M, Khan M, Rathsman P, Andersson G, Anflo K, Berge S, Bodin P, Edfors A, Hussain A, Kugelberg J, Larsson N, Ljung B, Meijer L, Mortsell A, Nordeback T, Persson S, and Sjoberg F (2002) “SMART-1 mission description and development status” in *Planetary and Space Science* **50**(14-15) pp. 1323–1337 DOI: 10.1016/S0032-0633(02)00123-X (cited on pages 20, 51).
- Racca G (2003a) *SMART-1 is changing thrust strategy to avoid long eclipses* SMART-1 Status Report 9, ESTEC, Noordwijk, The Netherlands (cited on pages 104–106).
- Racca G (2003b) *SMART-1 is finding her way through the radiation storms!!* SMART-1 Status Report 5, ESTEC, Noordwijk, The Netherlands (cited on page 97).
- Racca G (2003c) *SMART-1 is working well and continues thrusting* SMART-1 Status Report 8, ESTEC, Noordwijk, The Netherlands (cited on page 97).
- Rayman MD and Lehman DH (1997) “Deep Space One: NASA’s first deep-space technology validation mission” in *Acta Astronautica* **41**(4-10) pp. 289–299 DOI: 10.1016/S0094-5765(98)00073-3 (cited on page 17).
- Rayman MD, Chadbourne PA, Culwell JS, and Williams SN (1999) “Mission design for Deep Space 1: A low-thrust technology validation mission” in *Acta Astronautica* **45**(4-9) pp. 381–388 DOI: 10.1016/S0094-5765(99)00157-5 (cited on page 18).
- Rayman MD, Fraschetti TC, Raymond CA, and Russell CT (2007) “Coupling of system resource margins through the use of electric propulsion: Implications in preparing for the Dawn mission to Ceres and Vesta” in *Acta Astronautica* **60**(10-11) pp. 930–938 DOI: 10.1016/j.actaastro.2006.11.012 (cited on page 22).

- Ren Y, Cui P, and Luan E (2007) “A novel algorithm to optimize complicated low-thrust trajectory” in *Aircraft Engineering and Aerospace Technology* **79**(3) pp. 283–288 DOI: 10.1108/00022660710743895 (cited on page 42).
- Röser HP, Auweter-Kurtz M, Wagner HP, Laufer R, Podhajsky S, Wegmann T, and Hüber F (2006) “Challenges and innovative technologies for a low cost lunar mission” in *Acta Astronautica* **59**(8–11) pp. 1048–1051 DOI: 10.1016/j.actaastro.2005.07.048 (cited on pages 2, 3, 54, 81, 82).
- Sawyer D and Vette J (1976) *AP-8 trapped proton environment for solar maximum and solar minimum* Technical Report 76-06, National Space Science Data Center, Greenbelt, Maryland (cited on page 50).
- Schönmäkers J (2004) *Post-launch optimisation of the SMART-1 low-thrust trajectory to the Moon* Technical Report 548, European Space Agency, Noordwijk, 2200 AG, Netherlands, pp. 505–510 (cited on page 20).
- STK Suite Help Files* (2011), Version 9.2.3, Analytical Graphics, Inc. (cited on page 60).
- Stoer J and Bulirsch R (2002) *Introduction to Numerical Analysis* 3rd Edition, Springer-Verlag, Berlin & Heidelberg (cited on page 30).
- Stryck O van and Bulirsch R (1992) “Direct and Indirect Methods for Trajectory Optimization” in *Annals of Operations Research* **37**(1) pp. 357–373 DOI: 10.1007/BF02071065 (cited on page 44).
- Stuhlinger E (1964) *Ion Propulsion for Spaceflight*, McGraw-Hill, New York, USA (cited on page 35).
- Sweetser TH, Broschart SB, Angelopoulos V, Whiffen GJ, Folta DC, Chung MK, Hatch SJ, and Woodard MA (2011) “ARTEMIS Mission Design” in *Space Science Reviews* **165**(1–4) pp. 27–57 DOI: 10.1007/s11214-012-9869-1 (cited on page 11).

- Tapley BD, Watkins MM, Ries JC, Davis GW, Eanes RJ, Poole SR, Rim HJ, Schutz BE, Shum CK, Nerem RS, Lerch FJ, Marshall JA, Klosko SM, Pavlis NK, and Williamson RG (1996) “The Joint Gravity Model 3” in *Journal of Geophysical Research* **101**(B12) pp. 28029–49 DOI: 10.1029/96JB01645 (cited on page 70).
- Tetlow MR (2003) “Commercial Launch Vehicle Design and Predictive Guidance Development”, PhD thesis, School of Mechanical Engineering, University of Adelaide (cited on page 53).
- Trawny N, Gräßlin M, Laufer R, and Röser HP (2004) “Mission scenarios for a controlled lunar impact of a small satellite” in *55th International Astronautical Congress* Volume 6, International Astronautical Federation, Vancouver, Canada, pp. 3712–3717 (cited on page 4).
- Tsiolkovsky KE (1903) *The Exploration of Cosmic Space by Means of Reaction Devices*, Publishing House of the Defence Industry, Moscow (cited on page 55).
- U.S. Geological Survey (2008) *ESA’s Lunar SMART-1 Mission Extended* URL: <http://astrogeology.usgs.gov/HotTopics/index.php?archives/10-ESAs-Lunar-SMART-1-Mission-Extended.html> (visited on [visited on Aug. 5, 2008]) (cited on page 21).
- U.S. Naval Observatory (2008) *Time Service Dept. Leap Seconds* URL: <http://tycho.usno.navy.mil/leapsec.html> (visited on [visited on Feb. 23, 2009]) (cited on page 57).
- Vasile M and Locatelli M (2009) “A hybrid multiagent approach for global trajectory optimization” in *Journal of Global Optimization* **44**(4) pp. 461–479 DOI: 10.1007/s10898-008-9329-3 (cited on page 44).
- Walker MJH (1986) “A set of modified equinoctial orbit elements (Errata)” in *Celestial Mechanics and Dynamical Astronomy* **38**(4) pp. 391–392 DOI: 10.1007/BF01238929 (cited on pages 64, 65).
- Walker MJH, Ireland B, and Owens J (1985) “A set of modified equinoctial orbit elements” in *Celestial Mechanics and Dynamical Astronomy* **36**(4) pp. 409–419 DOI: 10.1007/BF01227493 (cited on pages 64, 78).

- Wollenhaupt B, Herdrich G, Fasoulas S, and Röser HP (2011) “Overview of Thermal Arcjet Thruster Development” in *28th International Symposium on Space Technology and Science*, B-51, Okinawa, Japan (cited on page 88).
- Yam C, Lorenzo D, and Izzo D (2011) “Low-thrust trajectory design as a constrained global optimization problem” in *Journal of Aerospace Engineering* **225**(11) pp. 1243–1251 DOI: [10.1177/0954410011401686](https://doi.org/10.1177/0954410011401686) (cited on page 44).
- Yang G (2007) “Earth-Moon trajectory optimization using solar electric propulsion” in *Chinese Journal of Aeronautics* **20**(5) pp. 452–463 DOI: [10.1016/S1000-9361\(07\)60067-3](https://doi.org/10.1016/S1000-9361(07)60067-3) (cited on pages 1, 69).
- Zeile O, Lachenmann M, Baumstark E, Mohr A, Bock D, Laufer R, Sneeuw N, and Röser HP (2010) “Analyses of orbital lifetime and observation conditions of small lunar satellites” in *Acta Astronautica* **66**(3–4) pp. 516–527 DOI: [10.1016/j.actaastro.2009.07.008](https://doi.org/10.1016/j.actaastro.2009.07.008) (cited on pages 4, 69, 178).
- Zhang CZ (1994) “A note on the physical parameters of the Moon” in *Earth, Moon, and Planets* **64**(1) pp. 31–38 DOI: [10.1007/BF00608202](https://doi.org/10.1007/BF00608202) (cited on page 65).